UNIVERSIDADE ESTADUAL PAULISTA "JÚLIO DE MESQUITA FILHO"
CAMPUS DE PRESIDENTE PRUDENTE
FACULDADE DE CIÊNCIAS E TECNOLOGIA
Programa de Pós-Graduação em Ciências Cartográficas

NARIANE MARSELHE RIBEIRO BERNARDO

A SEMIANALYTICAL ALGORITHM TO RETRIEVE THE SUSPENDED PARTICULATE MATTER IN A CASCADE RESERVOIR SYSTEM WITH WIDELY DIFFERING OPTICAL PROPERTIES

PRESIDENTE PRUDENTE
2019

NARIANE MARSELHE RIBEIRO BERNARDO

A SEMIANALYTICAL ALGORITHM TO RETRIEVE THE SUSPENDED PARTICULATE MATTER IN A CASCADE RESERVOIR SYSTEM WITH WIDELY DIFFERING OPTICAL PROPERTIES

Thesis presented to the Department of Cartography of the Faculty of Science and Technology of São Paulo State University as part of the requirements for obtaining the PhD degree in Cartographic Sciences.

Advisor: Prof. Dr. Enner Alcântara

PRESIDENTE PRUDENTE
2019

B523s

Bernardo, Nariane Marselhe Ribeiro

A semianalytical algorithm to retrieve the suspended particulate matter in a cascade reservoir system with widely differing optical properties / Nariane Marselhe Ribeiro Bernardo. -- Presidente Prudente, 2019

148 f.

Tese (doutorado) - Universidade Estadual Paulista (Unesp), Faculdade de Ciências e Tecnologia, Presidente Prudente

Orientador: Enner Herênio Alcântara

1. bio-ótica. 2. águas interiores. 3. qualidade da água. 4. sensoriamento remoto. I. Título.

Sistema de geração automática de fichas catalográficas da Unesp. Biblioteca da Faculdade de Ciências e Tecnologia, Presidente Prudente. Dados fornecidos pelo autor(a).

Essa ficha não pode ser modificada.

unesp UNIVERSIDADE ESTADUAL PAULISTA

Câmpus de Presidente Prudente

CERTIFICADO DE APROVAÇÃO

TÍTULO DA TESE: A semianalytical algorithm to retrieve the suspended particulate matter in a cascade reservoir system with widely differing optical properties

AUTORA: NARIANE MARSELHE RIBEIRO BERNARDO
ORIENTADOR: ENNER HERENIO DE ALCÂNTARA

Aprovada como parte das exigências para obtenção do Título de Doutora em CIÊNCIAS CARTOGRÁFICAS, área: Aquisição, Análise e Representação de Informações Espaciais pela Comissão Examinadora:

Prof. Dr. ENNER HERENIO DE ALCÂNTARA
Departamento de Engenharia Ambiental / Instituto de Ciência e Tecnologia de São José dos Campos

Prof. Dr. LUIZ HENRIQUE DA SILVA ROTTA
Pós-Doutorando PNPD / Faculdade de Ciências e Tecnologia de Presidente Prudente

Prof. Dr. NILTON NOBUHIRO IMAI
Departamento de Cartografia / Faculdade de Ciencias e Tecnologia de Presidente Prudente

Prof. Dr. ARCILAN TREVENZOLI ASSIREU
Instituto de Recursos Naturais / Universidade Federal de Itajubá

Profa. Dra. THANAN WALESZA PEQUENO RODRIGUES GUIMARÃES
IFPA / Instituto Federal do Pará

VIDEOCONFERÊNCIA

Presidente Prudente, 03 de setembro de 2019

To God

To my Grandparents, Florinda e Joaquim, Luiz e Maria Hilda

To my parents, Nadir e Mário Bernardo

To my husband, Alisson do Carmo

To our daughter, Cecília Bernardo do Carmo

AGRADECIMENTOS

Dou início aos agradecimentos, primeiramente expressando em palavras minha gratidão à Deus por permitir que pudesse realizar todas as etapas do trabalho de forma segura. Foi graças à Sua proteção que concluímos os trabalhos de campo mesmo em tantas dificuldades. Gratidão por todas as oportunidades, aprendizados e bênçãos recebidas ao longo desta jornada.

Aos meus pais, Nadir Ribeiro Bernardo e Mário Luiz Bernardo, por todo o amor e incentivo. Obrigada por serem exemplos de amor, respeito, dedicação e caráter. Obrigada por me ensinarem a nunca desistir e a aprender com os erros. Obrigada por proporcionarem todas as condições possíveis para que eu finalizasse meus estudos de forma plena e com dedicação total.

Agradeço ao meu esposo, Alisson Fernando Coelho do Carmo, por todo o amor, apoio e otimismo. Obrigada pela ajuda em trabalhos de campo, processamento de dados e por sempre deixar minha vida mais leve, enxergando as belezas das coisas simples e o melhor lado de todas as situações.

Gratidão ao meu orientador Enner Herênio Alcântara, por todos os ensinamentos na vida profissional e pessoal, por toda a disponibilidade, prontidão e eficiência na execução dos trabalhos, pela busca por aportes financeiros para desenvolvimento de tarefas e por acreditar sempre no nosso trabalho.

À Unesp, pela disponibilidade da estrutura física para desenvolvimento deste trabalho, bem como aos professores do PPGCC - em especial aos professores Dr. Nilton Imai e Dra. Maria de Lourdes Galo. Agradeço também ao professor Dr. Arcilan, participante da banca examinadora, sempre contribuindo com sugestões primorosas para o trabalho.

Aos amigos do PPGCC, e em especial àqueles que são uma família para mim durante o doutorado e fazem parte do nosso grupo de pesquisa (SERTIE) - Fernanda Watanabe, Luiz Henrique Rotta, Thanan Rodrigues, Carol Campos, Bruno Fagah, Gabi Takahashi. Ainda agradeço pelos momentos de descontração e desabafos com os amigos feitos durante a pós-graduação Dani Arana, Tayná e Mariana Campos, bem como com as meninas que zelavam da integridade da nossa sala de permanência, Cidinha e Zilda, sempre nos presenteando com um bom dia acolhedor mesmo quando estávamos desanimados

À agência de fomento pela bolsa concedida no período dedicado à realização da tese. O presente trabalho foi realizado com apoio da Coordenação de Aperfeiçoamento de Pessoal de Nível Superior - Brasil (CAPES) - Código de Financiamento 001.

Agradecimentos também à Fundação de Amparo à pesquisa do Estado de São Paulo – FAPESP, pelo financiamento dos projetos **nº 2012/19821-1, 2015/21586-9, 2015/18525-8 and 2019/00259-0**, e ao Conselho Nacional de Tecnologia e Desenvolvimento (CNPq) pelos projetos dos processos n°**472131/2012-5** e n°**482605/2013-8**.

RESUMO

O Material Particulado em Suspensão (MPS) é o principal componente em sistemas aquáticos. Elevadas concentrações de MPS implicam na atenuação da luz, e ocasionam alterações das taxas fotossintéticas. Além disso, a presença de MPS no sistema aquático pode aumentar os níveis de turbidez, absorver poluentes e podem ser considerados como um indicativo de descargas de escoamento superficial. Portanto, monitorar as concentrações de MPS é essencial para a gerar informações técnicas que subsidiem o correto manejo dos recursos aquáticos, prevenindo colapsos hidrológicos. O sensoriamento remoto se mostra como uma eficiente ferramenta para monitorar e mapear MPS quando comparada às técnicas tradicionais de monitoramento, como as medidas in situ. Entretanto, diante de uma grande e complexa variabilidade de componentes óticos, desenvolver modelos de MPS por meio do sinal registrado em sensores remotos é um desafio. Diversos modelos foram desenvolvidos para reservatórios, lagos e lagoas específicos. Atualmente, não há um único modelo capaz de estimar MPS em reservatórios brasileiros em cascata. Com o objetivo de estimar as concentrações de MPS de forma acurada, o objetivo desta tese foi desenvolver um modelo semi-analítico capaz de estimar valores de coeficiente de atenuação, K_d, por meio do uso dos coeficientes de absorção e espalhamento e, consequentemente, utilizar os valores de K_d para estimar as concentrações de MPS. A adoção desta estratégica se baseou na atenuação da luz ao longo da coluna da água, causada pela presença de MPS. Inicialmente, as características óticas dos reservatórios foram investigadas. Foi observado que cada reservatório apresenta um componente oticamente ativo (COA) dominante, como em Barra Bonita, o primeiro reservatório da cascata, dominado pela fração orgânica do MPS, enquanto que Nova Avanhandava, o ultimo reservatório da cascata, a fração inorgânica de MPS é dominante. Além disso, Bariri e Ibitinga, reservatórios localizados próximos à Barra Bonita, apresentaram elevadas contribuições de material orgânico dissolvido colorido (CDOM). Todas estas características implicam em diferentes propriedades bio-ópticas. Sequencialmente, a qualidade da reflectância de sensoriamento remoto (R_{sr}) foi avaliada por meio da comparação de quatro métodos, publicados na literatura, para remoção do efeito especular. Para validação dos resultados, o resultado das simulações obtidas via Hydrolight® foi utilizado como dado de referência. Os resultados demonstraram que o uso de um fator hiperespectral que compense a componente especular foi a melhor abordagem para calcular os dados de R_{sr}, reduzindo aproximadamente 30% dos erros quando comparados às outras abordagens, as quais consideraram apenas a velocidade do vento como causa do efeito especular. Por fim, modelos empíricos e semi-analíticos foram desenvolvidos, sendo que os modelos semi-analíticos apresentaram um resultado mais satisfatório para as estimativas das concentrações de MPS do que os modelos empíricos. O modelo desenvolvido na presente tese, QAA_{TRCS}, resultou em erros médios menores que 30%, enquanto que os modelos empíricos retornaram erros de até 80%. Em vista do grande intervalo de concentrações de COAs e da variabilidade ótica observada no reservatórios em cascata, o QAA_{TRCS} foi capaz de estimar de forma acurada as concentrações de MPS.

Palavras-chave: bio-ótica; águas interiores; qualidade da água; OLI/Landsat-8; sensoriamento remoto.

ABSCTRACT

Suspended particulate matter (SPM) is the main component presented within aquatic system. High levels of SPM concentration attenuate the light affecting the photosynthesis rates. Besides, can increase turbidity levels, absorb pollutions and is an indicative of runoff discharges. Therefore, monitoring SPM concentrations is essential to provide reliable information for a correct water management to prevent hydrological collapse. Remote sensing emerges as an efficient tool to map and monitor SPM when compared to traditional techniques, such as in situ measurements. Nevertheless, considering a widely range of optical components, modeling the remote sensing signal in terms of SPM is a challenge. Several models were developed for specific reservoirs, lakes or ponds. Up to our knowledge, there is not a single model capable to retrieve SPM in Brazilian linked reservoirs in a cascade system. In order to accurately estimate SPM, the aim of the thesis was developed a semianalytical model capable to estimate K_d via absorption and backscattering coefficients, and then, use K_d to derive SPM. This approach was adopted because SPM directly contributes to the light attenuation within the water column. Firstly, optical features were investigated. It was found that each reservoir presented a specific optical active component (OAC) dominance, such as Barra Bonita, the first reservoir in cascade is dominated by organic SPM, while Nova Avanhandava, the last reservoir in cascade is dominated by inorganic SPM. Besides, Bariri and Ibitinga reservoirs located nearest Barra Bonita, demonstrated high levels of CDOM contribution. All these characteristics imply in changes of bio-optical properties. In sequence, the quality of remote sensing reflectance (R_{rs}) was calculated by comparing four methods published in literature, and using as reference for validation, the simulated dataset via Hydrolight®. The results demonstrated that use a hyperspectral factor to compensate the specular component is the best approach to compute suitable R_{rs}, reducing 30% of errors when compared to approaches that use wind speed as the only factor of glint effect. Then, empirical and semianalytical models were developed, and the semianalytical model provided more satisfactory results of SPM estimations than empirical model. Our developed semianalytical model, called $\mathrm{QAA_{TRCS}}$, retrieved errors for SPM estimates lower than 30% on average, while the empirical model reaches errors near 80%. Considering the widely range OACs concentration and the optical properties variability, $\mathrm{QAA_{TRCS}}$ was capable to provide reliable SPM estimates.

Keywords: bio-optics; inland water; water quality; OLI/Landsat-8; proximal remote sensing.

LIST OF FIGURES

LIST OF TABLES

CONTENT

CHAPTER 1: INTRODUCTION

1.1 RESEARCH CONTEXT

Earth's system observation has been used along last decades for aquatic system monitoring in a sustainable manner, providing a synoptic view of Earth's dynamics (Kirk 2011, Muow et al., 2015). The mark of using remote sensing signal starts at 1978, with the launch of first satellite for water applications – Coastal Zone Color Scanner (CZCS, see Table 1.1 and 1.2 for descriptions of symbols and acronyms, respectively) for ocean systems. In inland waters, the investigations initialize later, in the last decade of 1980s (Giardino et al 2018). Currently, the technical improvements in remote sensors have been produced better datasets with upgraded of spatial, temporal, spectral, and radiometric resolutions, aiming to provide reliable information for monitoring different sizes of aquatic systems (Lobo et al., 2015; Giardino et al., 2018).

The accessibility of restrict areas, a broader coverage of study areas, and higher frequency rates of dataset production, are the main strengths when compared to the traditional monitoring techniques, as in situ sampling (Muow et al., 2015, Palmer et al., 2015). Besides, remotely sensed monitoring is mostly safe-cost, considering the quantity of remote sensing datasets that are freely available for download, or even better, can be processed in cloud such as the Google Earth Engine platform (Hansen et al., 2018). More robust and easier access of datasets, improvements of processing capacities, evolution of assessments techniques, along with the expansion of knowledge in hydrological optics theory resulting in a bunch of features to efficiently monitor, predict and technically support the water management decisions for sustainable water uses.

Water quality monitoring using remotely sensed datasets that are capable to register and reproduce, by graphs or images, the interaction of electromagnetic energy and the optical active components (OACs) within the aquatic systems. The main OACs are summarizing by water, phytoplankton (characterized as chlorophyll-a, Chl-*a*), colored dissolved organic matter (CDOM) and suspended particulate matter (SPM). All of them interact with the incident energy by absorbing or scattering the light (Morel and Prieur, 1977).

The absorption and scattering processes can be defined as the coefficients that characterize the inherent optical properties (IOPs) of the water column. Because of these interactions, the

IOPs can be considered as proportional to the concentration and types of OACs within the water column (Kirk, 2011). The aquatic systems also can be described accordingly to the apparent optical properties (AOPs), such as the remote sensing reflectance (R_{rs}) and vertical coefficient of light attenuation (K_d). The AOPs are influenced by the presence of OACs, but also are directly affected to the variation of the incident light field (Preisendorfer 1961, Kirk, 2011).

Among the OACs, the major component of inland water sytems is the SPM, which plays an important role in hydrophysical functioning and internal cycles (Lymburner et al., 2016). Due to its capability to absorb and scatter the light, the SPM is responsible to increase the levels of turbidity, attenuate and reduce the underwater light field, absorb the pollution components, and affect the photosynthesis process that compromises the benthonic life (Billota and Brazier, 2008). Therefore, understanding the SPM dynamics that are responsible to affect the availability of energy inside the aquatic system is essential to guarantee better conditions for the underwater life, besides providing the sustainability of the water resources for now and future uses.

In inland waters, in contrast of ocean systems, presented a higher complexity of OACs due to the widely variation composition and concentrations ranges. Because of the runoff from catchments and anthropogenic activities, inland waters are commonly characterized as highly turbid environments (Zhang et al., 2009). Consequently, a widely OACs variability implies in more complex optical system (Lee et al., 2002) and great efforts are required to establish a bio-optical models capable to produce accurately SPM estimates (Muow et al., 2018; Palmer et al., 2015; Giardino et al., 2018).

Besides the optical complexity challenge, the radiometric signal resulted from aquatic and light interactions cross the atmosphere to reach the sensors. Throughout the atmospheric optical path, the atmospheric components directly attenuate the signal, and almost 90% of registered information is derived from atmospheric influence (Bernardo et al., 2016), also affecting the accuracy of SPM estimates. Beyond aforementioned challenges, other drawbacks that might be considered are the viewing geometry set and the environmental conditions during the field measurements, such as the cloud coverage, time acquisition, wind speed and platform stability, in this case, the boat stability. Viewing geometry is an important factor into the field site measurements due to the glint effects (Mobley 1999), while the field conditions can introduce errors to compute R_{rs}, the most relevant variable to establish an accurate bio-optical modeling (Lee et al., 2010). Therefore, the present thesis aims to deal with these challenges that decrease the performance of SPM retrieval model, and presenting the key solutions found to provide the most accurately SPM estimates over a widely range of OACs within aquatic systems.

Table 1.1 List of acronyms.

Acronym	Description
AOPs	Apparent Optical Properties
IOPs	Inherent Optical Properties
BB	Barra Bonita Hydroelectric Reservoir
BAR	Bariri Hydroelectric Reservoir
IBI	Ibitinga Hydroelectric Reservoir
NAV	Nova Avanhandava Hydroelectric Reservoir
CDOM	Colored dissolved organic matter
CZCS	Coastal Zone Color Scanner
Chl-*a*	Chlorophyll-a
QAA	Quasi analytical algorithm
NAP	Non-algae particles
OAC	Optical active components
PIM	Suspended Particulate Inorganic Matter
POM	Suspended Particulate Organic Matter
SPM	Suspended Particulate Matter
TRCS	Tietê River Cascade System

Table 1.2 List of symbols

Symbol	Parameter	Unit
Γ	Geometrical light factor	-
R_{rs}	Remote sensing reflectance above water surface	sr^{-1}
r_{rs}	Remote sensing reflectance below water surface	sr^{-1}
Y	Spectral power of particle backscattering coefficient	-
S	Spectral slope for non-algae particles (S_{nap}) or CDOM (S_{cdom})	nm^{-1}
SPM	SPM = PIM + POM	$mg.L^{-1}$
$E_d(\lambda)$	Spectral downwelling irradiance below the water surface	$W.m^{-2}. nm^{-1}$
$E_s(\lambda)$	Spectral downwelling irradiance incident onto the water surface	$W.m^{-2}. nm^{-1}$
$L_t(\lambda)$	Spectral total radiance above water surface	$W.m^{-2}.sr^{-1}.nm^{-1}$
$L_{sky}(\lambda)$	Spectral incident sky radiance	$W.m^{-2}.sr^{-1}.nm^{-1}$
$K_d(\lambda)$	Downwelling diffuse attenuation coefficient	m^{-1}
$a(\lambda)$, $a_t(\lambda)$	Spectral total absorption coefficient ($a(\lambda) = a_{cdom}(\lambda)+ a_p(\lambda)+ a_w(\lambda)$)	m^{-1}
$a_{cdom}(\lambda)$	Spectral absorption coefficient of CDOM	m^{-1}

$a_p(\lambda)$	Spectral absorption coefficient of particulate matter ($a_p(\lambda) = a_p(\lambda) + a_{nap}(\lambda)$)	m^{-1}
$a_\varphi(\lambda)$	Spectral absorption coefficient of phytoplankton pigments	m^{-1}
$a_{nap}(\lambda)$	Spectral absorption coefficient of non-algae particles	m^{-1}
$a_w(\lambda)$	Spectral absorption coefficient of water	m^{-1}
$a_{tnw}(\lambda)$,$a_{t\text{-}w}$	Spectral non-water total absorption coefficient	m^{-1}
$b(\lambda)$	Spectral scattering coefficient	m^{-1}
$b_b(\lambda)$	Spectral total backscattering coefficient ($b_b(\lambda)$=$b_{bp}(\lambda)$+ $b_{bw}(\lambda)$)	m^{-1}
$b_{bp}(\lambda)$	Spectral total backscattering coefficient of particulate matter	m^{-1}
$b_{bw}(\lambda)$	Spectral total backscattering coefficient of water	m^{-1}
$u(\lambda)$	Ratio of backscattering coefficient to the sum of absorption and backscattering coefficient ($b_b(\lambda)$/ $b_b(\lambda)$+ $a(\lambda)$)	-
Z	Depth within the water column	m
z_i	Depth for time - i	m
Z_{SD}	Secchi Disk Depth	m
Q	Ratio between	
T	radiance transmittance	
γ	water to air internal reflection coefficient	
λ_0	Reference wavelength	nm

1.2 MOTIVATION

Remote sensing data is capable to estimate the OACs concentrations using bio-optical modeling, it means, mathematically describing the relationships between OACs and an optical property measured by or derived from an optical sensor (Morel 2001). Two main groups characterize the bio-optical modeling – the analytical and empirical (Ogashawara et al., 2016). The empirical algorithms are established using linear regressions or other function fitting between the optical property (R, R_{rs}, a, b_b) and the component of interest (Chl-*a*, SPM, or CDOM, for instance). In this case, the optical property is described as a single parameter or a band ratio combination (Doxaran et al., 2002), and the established model is directly applied to the satellite images. However, the confidence interval of these models is extremely dependent to the interval of the calibration dataset, losing the accuracy when the empirical model is applied to another dataset with different ranges of OACs or optical properties (Matthews, 2011). Additionally, the relation between R_{rs} and OACs can saturate at certain concentration levels, providing a restriction into OACs estimations (Luo et al., 2018).

The other category, the analytical models, is based on principles of radiative transfer equation that mathematically describe the changes in the light field throughout the water column accordingly to the IOPs (Dekker and Hestir, 2012). These algorithms also can be subdivided into two categories – the semi-analytical (SA) and quasi-analytical (QAA). The SA models are capable to model the total absorption (a_t) as a function of the each OACs' absorption (Roesler and Perry, 1995, Maritorena et al., 2002), whereas the QAA model derives the IOPs from R_{rs} (Lee et al., 2002). Relied on such physical principles, the SA and QAA models are more robust than empirical models and are suitable for a broader application range (Novoa et al., 2017). The QAA also presented the advantage of being less complex than SA, retrieving a comparable accuracy (Lee et al., 2002).

On the other hand, these models are originally developed for ocean waters conditions and when they are directly applied to inland water systems, appeared undesirable retrieval errors (Rodrigues et al., 2017). To overcome the challenges, it is possible to re-parameterize steps in QAA processing chain (Yang et al., 2013; Li et al., 2015; Watanabe et al., 2016; Rodrigues et al., 2018). Considering the needed of a model tuning, the re-parameterization of QAA is required for QAA applications to optical complex systems, as the inland waters.

Several studies have been conducted in order to provide improvements in QAA for inland waters. Some studies were conducted in widely turbid environments considering different geographic locations (Li et al., 2013; Joshi and D'sa et al., 2018), or there are other cases where the inland water systems presented frequently occurrence of blooms in hypertrophic environments (Mishra et al., 2014; Watanabe et al., 2016). Other relevant investigations were conducted in reservoirs that shown opposite optical conditions in different seasons (Rodrigues et al., 2017), or even considered an aquatic system with expressive CDOM effects (Ogashawara et al., 2016, Campos et al., 2017).

Up to our knowledge, studies of analytical bio-optical modeling considering a cascade of reservoirs system that presented a widely range of SPM were not developed. Cascade reservoirs systems are inland water environments, with high complexity driving from the watershed runoffs and the influence of the reservoirs in cascade, it means, the sequence of dams located at one river that cause a filtration process that change the inland water dynamics. In this context, the following question raises: Is it possible to establish a single model to derive SPM concentrations in a widely range of OACs such as in cascade reservoirs systems?

1.3 HYPOTHESIS

In inland water cascade systems, as the Tietê River Cascate System (TRCS), there is a widely range of OACs due to the cascade reservoir continuum concept (CRCC) effects. Such variability also affects the optical properties in aquatic systems. Currently studies based on the absorption properties in cascade reservoirs shown that there is no general dominance of OAC through the entire cascade, it means, each reservoir presented an optical component that dominates the optical properties (Bernardo et al., 2019; Alcântara et al., 2016).

In this respect, studies have been conducted for modeling the optical properties (Gomes et al., 2019; Rodrigues et al., 2017b; Alcântara et al., 2016) or OACs concentrations (Watanabe et al., 2016) considering specific Brazilian reservoirs. One of the most relevant study conducted over a widely range of SPM in cascading reservoirs concluded that is still a challenge to derive SPM concentrations using a single empirical model due to the presence of optical and OACs variability (Rodrigues et al., 2017).

Considering the effects of light attenuation in water column caused by SPM and the stability of derive K_d using IOPs, instead of using radiometry measurements that are very sensitive to the incident light field variations, it is appropriated to use K_d as a single explanatory variable to accurately derive SPM concentrations over a widely range of OACs concentration such as found in TRCS.

1.4 OBJECTIVES

The aim of this thesis is to provide a new semianalytical model capable to estimate reliable SPM concentrations over a complex aquatic system that presented high variability of OACs, such as the Tietê River Cascade System (TRCS). More specifically, the objectives aim to: (i) expand the knowledge of optical properties in linked and complex aquatic systems; (ii) assess and define a method capable to estimate the remote sensing reflectance with high accuracy; (iii) evaluate the strengths and weakness of empirical algorithms to retrieve SPM concentrations in a widely differing optical waters and; (iv) develop a semianalytical model to retrieve SPM concentration sensible to high variability in the optical properties.

1.5 CONTENT OF THESIS

The present thesis is composed by seven chapters. Chapter 1 introduces the context of remote sensing monitoring in aquatic systems, describes the state of art and the knowledge gaps that encourage our hypothesis, as well as, the objectives of the present thesis. The following chapters will present a brief introduction related to the content of respective chapter, methods and datasets used for investigations. In each chapter also is presented the results, discussion and conclusions, where are highlighted the main findings and pointed out the future steps regarding to the chapter content. As a final point, the Chapter 6 sums up the main findings from our research and itemize the future recommendations based on our results. A quickly description of each Chapter is provided in the sequence.

1.5.1 Chapter 2 – Study site

Chapter 2 aims to describe the characteristics of Tietê Cascade System River (TRCS) highlighting the aspect of cascade river continuum concept (CRCC) and the features related to this aspect, which makes the TRCS an interesting area for our deeper investigations. Features from TRCS's catchment are provided and more specific information about the hydroelectric reservoirs are related. Additionally, a brief description of acquisition methods and data processing is also presented.

1.5.2 Chapter 3 – Light absorption budget in a reservoir cascade system with widely differing optical properties

Chapter 3 focus on the absorption variability and the optical characterization in TRCS, by assessing the trends from up-to-downstream reservoirs located at TRCS. Aquatic systems are complex systems, due to environmental pressures that lead to water quality parameter changes and, consequently, variations in OAC. In cascading reservoir systems, such as the Tietê Cascade Reservoir System (TRCS), which has a length of 1100 km, the horizontal gradients are expressive due to the filtration process caused by the sequence of dams, affecting the light absorption throughout the cascade. Our new observations showed that CDOM are the main OAC in two reservoirs, non-algae particles (NAP) dominated another one and phytoplankton dominated the remainder one. The variability of light absorption along the cascade indicates the influence of watershed dynamics in the reservoirs as much as the flow driven by previous reservoirs. Despite the effect of the variability of light absorption, light absorption by phytoplankton strongly affects the total absorption in the four reservoirs in TRCS. The results obtained in this work may help to better understand how the gradient pattern changes primary production and also indicate a challenge in retrieving SPM concentrations using a singular bio-optical model for the entire cascade composed of different optical environments.

1.5.3 Chapter 4 – Glint Removal Assessment to Estimate the Remote Sensing Reflectance in Inland Waters with Widely Differing Optical Properties

Chapter 4 represented an investigation regarded to the in situ data quality measurements. The quality control of remote sensing reflectance (R_{rs}) is a challenging task in remote sensing applications, mainly in the retrieval of accurate in situ measurements carried out in optically complex aquatic systems. One of the main challenges is related to glint effect into the in situ measurements. Our study evaluates four different methods to reduce the glint effect from the R_{rs} spectra collected in cascade reservoirs with widely differing optical properties. The first (i) method adopts a constant coefficient for skylight correction (ρ) for any geometry viewing of in situ measurements and wind speed lower than 5 $m \cdot s^{-1}$; (ii) the second uses a look-up-table with variable ρ values accordingly to viewing geometry acquisition and wind speed; (iii) the third method is based on hyperspectral optimization to produce a spectral glint correction, and (iv) computes ρ as a function of wind speed. The glint effect corrected R_{rs} spectra were assessed using HydroLight simulations. The results showed that using the glint correction with spectral ρ achieved the lowest errors, however, in a Colored Dissolved Organic Matter (CDOM) dominated environment with no remarkable chlorophyll-*a* concentrations, the best method was the second. Besides, the results with spectral glint correction reduced almost 30% of errors.

1.5.4 Chapter 5 – Empirical investigations to SPM model

Chapter 5 aims to define an empirical bio-optical model to retrieve the SPM concentrations along the TRCS. Investigations were conducted to assess the effects of using the entire dataset of TRCS or specific datasets (from each field campaign) to provide SPM retrieval models. Robust datasets are capable to provide more reliable estimates? Do the empirical datasets achieve high levels of accuracy? Considering that the SPM composition in TRCS is highly variable, what are the impacts of such variation into remote sensing modeling using an empirical relationship? These issues and other features are investigated and shown in this chapter. The results demonstrated that band combination provided better results than single band models, and further investigations throughout analytical models can provide more accurate SPM estimates than empirical modeling.

1.5.5 Chapter 6 – Analytical approaches to retrieve SPM estimates in TRCS

Chapter 6 provide a new analytical model to estimate SPM concentrations in TRCS. Suspended matter particles directly affect the underwater light field, as consequence, change the water clarity conditions and the primary production can reduce. Efficient monitoring of SPM dynamics in inland waters system depending on the use of time-save tools and robust methods, such as remote sensing data and bio-optical modeling. Our aim was develop a robust bio-optical modeling capable to retrieve reliable SPM estimates for a widely range of SPM concentration based on the widely variability encountered at the Tietê River Cascade System (TRCS), with SPM ranging from 0 to 44 $mg.L^{-1}$. Additional challenging imposed by high levels of Chl-*a* (up to 700 $mg.m^{-3}$), turbidity up to 80 NTU and high CDOM absorption describe the faced optical complexity. Considering that K_d is the best single explanatory variable to derive SPM, without the saturation problem as R_{rs}, we estimate SPM concentrations via K_d. K_d was analytically derived from IOPs retrieved in the Quasi-Analytical modeling (QAA). Required accuracy for inland waters was obtained by re-parametrizing the original frame of QAA. Our model improved the estimates of IOPs in almost 30% when compared to other QAA versions. Furthermore, $K_d(655)$ was capable to describe 74% of SPM variations in TRCS, with average error lower than 30%.

1.5.6 Chapter 7 – Conclusions and Recommendations

Finally, Chapter 7 provides the key conclusions from the entire investigation are highlighted as the strengths of our work. We also pointed out the main recommendations for future investigations, based on the opportunities found during the development of this thesis.

CHAPTER 2: STUDY SITE AND SURVEYS

2.1 TIETÊ RIVER CASCADE SYSTEM

The Tietê River runs from east-to-west for 1100 km in São Paulo State, passing through the capital, and flows into the Paraná River, a tributary of the Plata River. From up-to-downstream, the Tietê River placed six hydroelectrical reservoirs in cascade, which are Barra Bonita (BB, 22°31'S, 48°32'W), Bariri (BAR, 22° 9'S,48°44'W), Ibitinga (IBI, 21°45'S, 48°59'), Promissão(21°48' S, 49°23'W), Nova Avanhandava (NAV, 21°71'S, 50°12'W), and Três Irmãos (21°38'S, 51°32'W). Together, BB, BAR, IBI and NAV producing an associated hydroelectric power of 1.8 MW, more than 90% of the total hydroelectric productivity generated by all reservoirs in Tietê River (including the smaller rivers) (ANEEL, 2017).

According to the land use and land cover, illustrated in Figure 2.1, we verified that the upstream LULC is dominated by industrial and artificial areas, responsible for high levels of sewage discharges (Watanabe et al., 2016). In the downstream regions, agriculture and pasture are the main economic activities, which also act as pollution sources due to the irrigation and the runoff from herbicides and other poisons resulted from bare soil and shrub lands.

Excepting NAV, which is a run-of-river reservoir, BB, BAR and IBI are storage systems. For BB, BAR, IBI and NAV, field campaigns were gathered out as described in Table 2.1 (see the sampling spots in Figure 2.1). BB reservoir is the first system of cascade, located near the São Paulo State capital, which can be considered as a meaningful pollution source due to waste discharges in the Tietê River's tributaries. Several studies have been demonstrated that the high levels of SPM concentrations and other pollutants in the Piracicaba River decreases from the upper to the downstream reservoirs (Rodgher et al., 2005; Bernardo et al., 2016; Rodrigues et al., 2016).

Figure 2.1. Brazil and São Paulo State (a); Map of the TRCS and respective land cover classes of Tietê basin (water body, forest, shrubland, bare soil, umid areas and urban areas by CPLA, 2010) (b); TRMM rainfall averages over TRCS(c); sampling locations were detailed for each reservoir Barra Bonita(d); Nova Avanhandava(d); Bariri(e); Ibitinga(f).

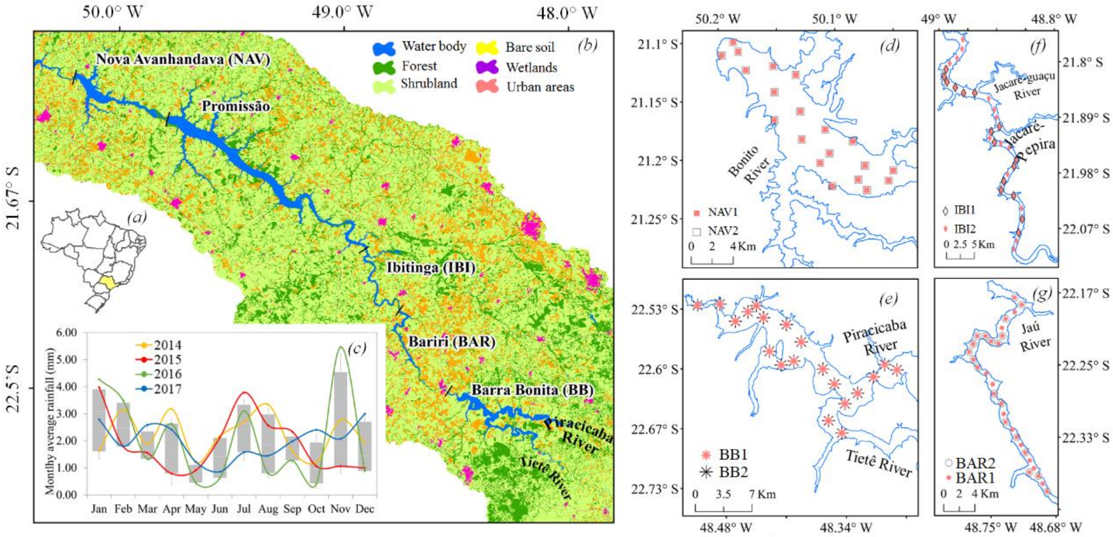

BB (22°31'S and 48°32'W) and BAR (22° 9'S and 48°44'W) are located in the middle course of the Tietê River watershed, with 310 km^2 and 63 km^2 of flooded area, respectively. The time residence of BB varies between 30 (summer) to 180 days (winter), whereas in the BAR it ranges between 7–24 days (Cairo et al., 2017). Both reservoirs are considered eutrophic systems, with recurrent microalgae blooms due to nutrient and pollutant discharges within the Tietê River driven by nearby urban areas (Barbosa et al., 1999; Prado et al., 2015; Tonietto, et al., 2015).

IBI (21°45'S and 48°59') and NAV (21°71'S and 50°12'W) are located in the middle and lower course of Tietê River, with flooded areas comprising 114 km^2 and 210 km^2, respectively. The time residence of water ranged from 25–41 days in IBI, and 46 days on average in NAV (Barbosa et al., 1999). IBI is considered a meso-to-eutrophic environment (Cairo et al., 2017), and NAV is considered an oligo-to-mesotrophic waters (Rodrigues et al., 2017).

Two field campaigns were conducted in each reservoir (see details in Table 2.1), and the sample geographic locations were selected following the design plan steps described by Rodrigues et al. (2016). Measurements of radiometric quantities and water sample collection were taken at each sampling spot. The following water quality parameters were also collected: Secchi Disk Depth (Z_{SD}, m), suspended particulate matter (SPM, $mg.L^{-1}$) and its respective organic and inorganic fractions (POM and PIM, $mg.L^{-1}$), chlorophyll-a (Chl-*a*, $mg.m^{-3}$), wind speed ($m.s^{-1}$) and depth (m).

Table 2.1. Sampling descriptions from each fieldwork in BB, BAR, IBI and NAV reservoirs from TRCS, and respective water quality parameters and radiometric measurements. L_t is the total radiance, L_{sky} is the incident sky radiance (both in $W{\cdot}m^{-2}{\cdot}sr^{-1}{\cdot}nm^{-1}$), E_s is the downwelling irradiance incident onto the water surface and E_d is the downwelling irradiance (both in $W{\cdot}m^{-2}{\cdot}nm^{-1}$). HR means hydroelectrical reservoir and *n* number of samples.

Field Campaign	ID	*n*	Time Acquisition	Radiometric Measurements	Water Quality and Physical Parameters
Barra Bonita HR	BB1	20	May 2014	L_t, L_{sky} E_s, E_d(z) a_{cdom}, a_{phy}, a_{nap}	Turbidity, Z_{SD}, SPM, PIM, POM, Chl-*a*, Wind Speed and Depth.
	BB2	20	October 2014		
Bariri HR	BAR1	30	August 2016		
	BAR2	18	June 2017		
Ibitinga HR	IBI1	30	July 2016		
	IBI2	16	June 2017		
Nova Avanhandava HR	NAV1	20	May 2014		
	NAV2	20	September 2014		

2.2 IN SITU DATASET

2.2.1 Water Quality Parameters

Turbidity (NTU), wind speed ($m.s^{-1}$), Z_{SD} (m), and bottom depths (Z, m) were taken in triplicate to reduce systematic errors. Turbidity and wind speed were measured with portable gadgets, a Turbidity Meter (Hanna Instruments- HI 93414, Hanna Instruments, Woonsocket, USA) that was calibrated at each day of field using standard solutions (1, 10, 75, 100 and 750 NTU), and an anemometer, respectively. The Z_{SD} measurements were collected using a 30-cm Secchi Disk Depth and the same technical observer was maintained in all fieldworks in order to minimize visual interpretation mistakes.

Water samples, in duplicate, were collected in each spot, and were filtrated at low vacuum by using Whatman GF/F filters (47 mm of diameter and 0.7 μm pore size), to establish the SPM, PIM, POM, and Chl-*a* concentrations. The SPM concentrations, and their organic and inorganic fractions, were obtained following the APHA protocol (1998). The Chl-*a* concentrations were obtained by the acetone extraction method and spectrophotometer analysis (Londe et al., 2016). Replicates were obtained in order to avoid systematic errors.

2.2.2 Spectral dataset

Measurements of irradiance and radiance quantities were obtained in situ using a set of TriOS Hyperspectral radiometers (RAMSES TriOS; TriOS, Germany), with measurements taken from 400 to 900 nm, at 3.3 of resolution. In order to standardize the entire dataset, linear interpolation at 1 nm were conducted (more details of TriOS processing can be found at Imai et al., 2014). The viewing geometry of sensors was adopted accordingly to Mobley (1999) in order to avoid boat shadows, high influence of specular radiance (glint) and noise effects. Details of radiometry processing are found in Chapter 4.

Furthermore, a(λ) were measured in laboratory analysis (Tasssan and Ferrari, 1995, 1997), and b(λ) coefficients were measured in situ using the equipments specified in Table 2.2.

Table 2.2 Absorption and scattering equipments employed in each field campaign.

ID	Time Acquisition	Absorption equipment	Scattering equipment
BB1	May 2014	SHIMADZU spectrophotometer	Hydro-Scat 6P
BB2	October 2014		ECO-BB9
BAR1	August 2016		ECO-BB9
BAR2	June 2017		ECO-BB9
IBI1	July 2016		ECO-BB9
IBI2	June 2017		ECO-BB9
NAV1	May 2014		Hydro-Scat 6P
NAV2	September 2014		ECO-BB9

Total absorption coefficients, $a_t(\lambda)$ (m^{-1}), were derived from the sum of CDOM, phytoplankton, NAP and water absorption. The water absorption were adopted from Pope and Fry (1997), while NAP and phytoplankton absorption coefficients were established accordingly to Tassan and Ferrari methodology (1995), and CDOM followed the method proposed in Bricaud et al.(1981). The measurements of absorbance were conducted in a spectrophotometer (SHIMADZU UV-VIS 2600 – Shimadzu, Japan) within the spectral range from 280 to 800 nm, at 1 nm of resolution. Acquisition methods and equations used to obtain absorption coefficients are better described in the Chapter 3.

Hydro-Scat 6P (HOBI Labs Inc., Tucson, AZ, USA) is capable to measure the Volume Scattering Function at six specific wavelengths that can be setting accordingly to the user's requirements, in our case, the choose wavelengths were positioned at 420, 442, 470, 510, 590, 700 nm and 715 nm (Alcântara et al., 2017). As an active sensor, it emits an incident light and a sensor is strategically positioned at the opposite part in order to register the backscattered light at an angle of 140° (Maffione and Dana, 1997; HOBI Labs, 2010). ECO-BB9 (WETLabs) were conducted using different wavelengths (412, 440, 488, 510, 532, 595, 660, 676 e 715 nm) and the angle used to measure the backscattered light is about 117° (industrial set configuration).

The process of corrections of backscattering measurements in terms of absorption corrections are described in Imai et al. (2015). Absorption corrections were conducted using and additional measurement of absorption from AC-S measurements (WETLabs) in BB and NAV fields (Watanabe et al., 2019). In the fields where AC-S measurements were not available, laboratory absorptions were used to proceed the corrections. Although AC-S taken measurements along the water profile, the laboratory absorption coefficients were used to correct only the backscattering measurements at 0.3 meters of depth, it means, we got a unique value to represent a sample instead of had a profile dataset as provided by AC-S.

Considering the differences in wavelengths from all the sensors used in the field, we exponentially fit a function along the values of backscattering coefficients to standardize the measurements. In this manner, we were capable to compare the reference dataset (in situ measurements) with the outputs modeling, such as the IOPs from QAA.

2.3 ORBITAL IMAGES

The date from each fieldwork was established with regard to the Landsat-8 overpass, to have in situ measurements that were coincident with satellite data for future applications. Furthermore, all field measurements were carried out during dried periods, which did not allow us to make seasonal interpretations. Principal Component Analysis was performed using the Standard deviation image, retrieved from the temporal series of Operational Land Imager onboard Landsat-8 (OLI/Landsat-8). The first component of the SD image was then used to determine the sampling locations within each reservoir (more details are given in Rodrigues et al. 2016). Details of OLI images used in this work are described in Chapter 5 and 6.

CHAPTER 3: LIGHT ABSORPTION BUDGET IN A RESERVOIR CASCADE SYSTEM WITH WIDELY DIFFERING OPTICAL PROPERTIES

This chapter was published in the **Water Journal.** doi: 10.3390/w11020229

3.1 SCOPE

Water quality monitoring has been efficiently performed via remotely sensed data, using empirical and analytical models, and when applied to time-series images, it provides synoptic scale observations (Lee et al., 2002; Odermatt et al., 2012; Rodrigues et al., 2016, Watanabe et al., 2016). The success of remote sensing applications to aquatic systems depends on the understanding of underwater light interactions with the Optically Active Compounds (OACs) (Kirk, 1994). These interactions are expressed by Inherent Optical Properties (IOPs), absorption and scattering of light, and the OACs are represented by Chlorophyll-*a* (Chl-*a*), Suspended Particulate Matter (SPM) and Colored Dissolved Organic Matter (CDOM) (Kirk, 1994).

Much attention has been devoted for characterizing aquatic systems and determining the spatial variability of IOPs in the ocean (Bricaud et al., 1981; Bricaud et al., 1995, Bricaud et al., 1998; Babin et al., 2003), in coastal environments (Gokul et al., 2014, Shaju et al., 2017; Vishnu et al., 2018), and bays (Ferreira et al., 2014, Das et al., 2017). For inland waters, efforts have been made to evaluate the Australian (Campbell et al., 2011), African (Matthews and Bernardo, 2013), and Brazilian Reservoirs (Alcântara et al., 2016; Rodrigues et al., 2016) to identify the optical differences between open oceans and freshwater systems. The newest studies have also been developed to classify the inland water systems (Moore et al., 2014, Shen et al., 2015; Spyrakos et al., 2014) and overcome the challenge of bio-optical modeling in such environments (Pahlevan et al., 2014).

Bio-optical modeling is used to create a remotely sensed-based algorithm, which can be applied to satellite images and can be used for monitoring water quality variability over time. In inland waters with specially linked water systems, such as cascading reservoirs, high variability in optical properties prevents the use of only one model to estimate the water quality parameters. For example, Rodrigues et al. (2017a) studied two reservoirs with widely differing optical properties and tried to estimate the SPM concentration using only one adjusted model. However, this was not possible; each reservoir needed a local model (Rodrigues et al., 2017). An understanding of how light is absorbed and how a connected system influences not only the absorption but also the water quality parameters is mandatory for operational monitoring from space. Until now, most studies investigate and propose development of new bio-optical models, however, few studies aim to understand light absorption variability and how it has been conducted on cascading systems.

In contrast to open oceans, inland waters are optically complex environments, due to the different influences of OACs (Moore et al., 2014). Moreover, inland waters are influenced by internal processes and environmental pressures, such as nutrient enrichment, wastewater discharges and other non-natural disturbances (Muow et al., 2015; Palmer et al., 2015; Shi et al., 2018). In cascade reservoir systems, the existence of sequential dams modifies the water retention time of continuous rivers and impacts the filtration process, which changes the OACs concentrations and compositions from up-to-downstream, as predicted by the Cascade Reservoir Continuum Concept (CRCC) (Barbosa et al., 1999). Relying on the OACs variability in TRCS, a relevant scientific question is raised: what is the behavior of the IOPS throughout cascading reservoirs, since the IOPs are related to the composition and morphology of OACs? We hypothesize that a strong relationship would exist between OACs concentration and absorption properties in aquatic continuum systems and both would be affected similarly by autochthonous and allochthonous strengths, throughout the course of the Tietê River.

Considering its 1100 km of extension, the Tietê Cascade System Reservoir (TRCS) environment is a challenging and relevant region to investigate, since its water attends to fishery activities, navigation, hydroelectric productivity, and supplies industrial, agriculture and domestic demands (Barbosa et al., 1999; Smith et al., 2014). The TRCS's waters are deeply affected by different non-natural contamination sources, such as discharges from pasture waste, wastewater from urban centers and other agricultural activities developed in nearby areas, including sugarcane and citrus crops (Frascareli et al., 2018). As consequence, Barra Bonita (BB) and Bariri (BAR) reservoirs are considered eutrophic environments (Dellamano-Oliveira et al., 2008), Ibitinga (IBI) is considered a meso-to-eutrophic (Londe et al., 2016;Cairo et al., 2017), and Nova-Avanhandava (NAV) is considered as oligo-to-mesotrophic environment (Rodrigues et al., 2016).

Understanding the optical features throughout long rivers is crucial for a better understanding of the riverine transfers and the potential role in global biogeochemical cycles. Therefore, the present data are suitable to contribute to the understanding of the dynamics of this type of aquatic system, aiming to gain insights into the optical information of South American aquatic continuum systems by sampling the absorption coefficients from non-algal-particle (NAP), Chl-*a* and CDOM in TRCS. The specific goals of this work were to analyze the optical properties in an aquatic continuum river, to identify whether there was a downstream gradient in spectral absorption and to verify the controls on light absorption budget. Considering the optical characteristics as well known, remote sensing products can be better used for continuous monitoring and to establish effective control strategies to improve water quality, mainly for larger rivers, such as Tietê.

3.2 DATA AND METHODS

3.2.1 In situ measurements

Eight field campaigns were made in TRCS - two field studies per reservoir (see details of sampled locations in Chapter 2), therefore each dataset was labeled with regard to the respective locations and time order, BB1, BB2, NAV1, NAV2, BAR1, BAR2, IBI1 and IBI2. The field studies were carried out on 05-09 May 2014 in BB1; 13-16 October 2014 in BB2; 15-18 August 2016 in BAR1; 23-24 June 2017 in BAR2; 19-23 July 2016 in IBI1; 21-22 June 2017 in IBI2; 28 April – 02 May 2014 in NAV1; and 24-26 September 2014 in NAV2.

Physical parameters, such as temperature (°C), turbidity (NTU), and depth (m), were measured in triplicate in all sampling locations. The Secchi disk depth (Z_{SD}, m^{-1}) was achieved with a black and white disk with 30 cm of diameter. Furthermore, water samples were collected near the surface (depth = 0.3 m) in 5 L black plastic bottles that were rinsed three times with the water from each sampling spot. To preserve the original features of samples, the bottles were stored in the dark at low temperatures until laboratory analysis, where absorption spectra measurements were made. The SPM and Chl-*a* concentrations were established following the APHA (1998) and Golterman et al. (1978) protocols (APHA, 1998; Golterman et al., 1975), respectively.

3.2.2 Laboratory analysis

The IOPs are represented by $a(\lambda)$, scattering coefficients ($b(\lambda)$), and the volume scattering function (VSF). To analyze the optical composition of the cascade system in terms of IOPs, only the absorption spectra measured in situ were assessed in this work. The total absorption spectra $a_t(\lambda)$ resulted from the contribution of each OAC spectrum (Equation 3.1) can be mathematically described as follow:

$$a_t(\lambda) = a_{cdom}(\lambda) + a_{\phi}(\lambda) + a_{nap}(\lambda) + a_w(\lambda), \tag{3.1}$$

where $a_t(\lambda)$ is the total absorption spectrum, $a_{cdom}(\lambda)$ is the absorption spectrum of CDOM (Equation 3.2), $a_{\varphi}(\lambda)$ is the absorption spectrum of phytoplankton (Equation 3.3), $a_{nap}(\lambda)$ is the absorption spectrum of Non-Algal Particles (NAP, Eq. 4), and $a_w(\lambda)$ is the absorption spectrum of pure water from Smith and Baker (1981).

All absorption coefficients were derived using absorbance readings (ABS) on a SHIMADZU UV-2600 UV–VIS spectrophotometer (SHIMADZU, Japan) with a 1 nm spectral resolution, ranging from 280 to 800 nm. The $a_{cdom}(\lambda)$ was established after water samples were filtered through a nylon membrane with a 47 mm diameter and 0.22 µm pore size. The filtrate was placed in quartz cuvettes, with an optical path of 10 cm (L = 0.1 m). Then, the spectral ABS readings were taken to derive $a_{cdom}(\lambda)$ after filtration and acclimation to room temperature (Equation 3.2):

$$a_{cdom}(\lambda) = \frac{2.303 \times ABS(\lambda)}{L}, \tag{3.2}$$

where L is the optical path length of the cuvette, and ABS is the spectral absorbance reading within 280-800 nm of interval. Baseline data were obtained by using Milli-Q water placed in a 10 cm quartz cuvette. The conversion factor (2.303) between the base 10 logarithm and natural logarithm was used and was applied to the baseline correction by subtracting the residual absorbance, i.e., the average value between 700 and 750 nm. The a_{cdom} spectra were established by methodology proposed by Bricaud et al. (1981) and the fit of the exponential function was also computed to achieve the S_{cdom} results (Babin et al., 2003).

To compute a_{nap} and a_{φ}, water samples were filtered through fiberglass filters (Whatman GF/F with 0.7 pore size and 47 mm diameter) and were placed inside the integrated sphere module, using a blank filter as reference, and were then wetted with drops of Milli-Q water during the laboratory analysis (Matthews and Bernard, 2013). The transmittance and reflectances were read to calculate the particulate absorption (a_p), following the T-R method (Tassan and Ferrari, 1995, 1998).

The bleaching of the organic fraction of SPM was performed using hypochlorite solution (NaClO) at 10%. The bleached filters were washed with Milli-Q water to prevent the eventual contamination of the remaining NaClO and new transmittances and reflectances readings were made to compute a_{nap}. The a_{φ} was achieved by subtracting a_{nap} from a_p (Equation 3.3 and 3.4).

$$a_{\phi}(\lambda) = a_p(\lambda) - a_{nap}(\lambda) \tag{3.3}$$

$$a_{nap}(\lambda) = a_{nap}(\lambda_0) \times e^{-S_{nap}(\lambda-\lambda_0)} \tag{3.4}$$

where S_{nap} is the slope of the exponential decreasing function considering a spectral range (the present study uses 400 to 700 nm), which mathematically describes the relative steepness of the curve (Twardowsky et al., 2004); λ_0 is the reference wavelength, usually adopted near 443 nm for a_{cdom} and a_{nap}. To avoid systematic errors due to different methodologies, all absorption values were established following specific protocols for each OAC.

3.3 RESULTS

3.3.1 Water Quality Scenery

The descriptive statistics of water quality parameters measured in situ are summarized in Table 3.1. In BB (both campaigns), particulate inorganic matter (PIM) presented the highest variation, with coefficient of variation (CV) = 78.8% and 37.3%, in BB1 and BB2. BAR1 showed the highest variation in Chl-*a* (CV = 80.5%), BAR2 presented the highest variation for PIM (CV = 42.9%). In IBI (both campaigns), the larger variability resulted from Chl-*a* (CV = 86.0% and 67.8%), and NAV (both campaigns), the larger variability was obtained in PIM (CV = 76.8% and 65.8%, respectively). The lowest variability resulted from temperature for all field studies, with CV comprising between 1.90 and 15.4%.

Table 3.1 Descriptive Statistics of water quality parameters in BB, BAR, IBI, NAV from two field campaigns. See the acronyms in Table 1.1 (Chapter 1).

	Z_{sd} (m)	**Turbidity (NTU)**	**pH**	**Chl-*a* ($mg.m^{-3}$)**	**SPM ($mg.L^{-1}$)**	**PIM ($mg.L^{-1}$)**	**POM ($mg.L^{-1}$)**	**Temp. (°C)**
				Barra Bonita 1 (n = 20) - BB1				
Min	0.80	1.66	7.18	17.75	3.60	0.20	2.80	24.5
Max	2.30	12.50	9.25	279.86	16.30	4.40	14.7	26.9
Mean	1.49	5.17	8.36	120.44	7.21	1.10	6.10	25.6
CV	28.9	47.0	8.32	58.4	45.21	78.8	52.0	2.8
				Barra Bonita 2 (n = 20) - BB2				
Min	0.37	11.60	7.12	263.20	10.80	0.60	10.2	24.5
Max	0.78	33.20	10.1	797.80	44.00	3.80	30.4	32.1
Mean	0.57	18.64	9.28	428.72	21.97	2.60	18.2	28.1
CV	17.18	28.26	9.44	36.03	32.05	37.30	26.2	7.8
				Bariri (n = 30) – BAR1				
Min	0.50	7.80	6.10	25.67	3.60	0.90	1.4	21.1
Max	1.60	80.90	9.90	709.89	40.33	4.00	-	-
Mean	1.16	16.60	7.90	119.76	8.28	2.30	5.9	24.3
CV	20.03	45.82	10.5	80.52	54.76	21.4	75.1	15.4
				Bariri (n = 18) – BAR2				
Min	1.60	3.50	6.83	3.80	0.20	0.20	0.40	22.0
Max	3.20	8.80	7.28	19.0	2.60	1.30	1.60	23.9
Mean	2.20	5.7	6.97	8.00	1.60	0.60	1.10	22.8
CV	10.9	21.9	1.90	40.9	27.90	42.4	28.8	1.90
				Ibitinga (n = 30) – IBI1				
Min	1.60	2.82	5.50	1.37	1.00	0.30	0.50	21.2
Max	3.20	8.87	7.00	119.04	8.10	2.60	6.00	30.1
Mean	2.23	4.29	6.10	21.75	2.61	0.80	1.80	23.7
CV	10.91	17.90	6.80	85.97	39.20	35.3	49.6	9.50
				Ibitinga (n = 16) – IBI2				
Min	1.90	1.85	6.50	2.50	0.20	0.20	0.30	21.40
Max	3.80	3.60	6.96	13.7	2.20	1.00	1.90	24.00
Mean	2.90	2.47	6.78	6.64	1.06	0.40	0.93	22.82
CV	19.5	21.1	1.77	67.2	53.5	61.8	49.8	3.80
				Nova Avanhandava 1 (n = 20) - NAV1				
Min	2.29	1.01	8.50	2.46	0.10	0.10	0.20	25.1
Max	4.80	2.47	8.90	12.56	2.60	2.20	0.90	26.3
Mean	3.15	1.66	8.60	6.21	1.01	0.70	0.93	26.0
CV	19.95	25.40	1.39	40.0	61.7	76.7	40.8	1.12
				Nova Avanhandava 2 (n = 20) - NAV2				
Min	2.45	1.01	7.60	4.51	0.50	0.14	0.30	23.8

Max	4.65	2.56	8.30	20.5	2.80	2.00	1.10	25.6
Mean	3.41	1.73	8.10	9.01	1.00	0.50	0.50	24.6
CV	14.1	18.98	2.20	34.9	37.6	65.8	26.5	1.90
All dataset (n =174*)								
Min	0.37	1.01	5.50	1.37	0.10	0.08	0.20	21.1
Max	4.80	80.9	10.1	797.80	44.00	4.40	43.00	39.4
Mean	1.15	13.31	8.36	197.50	11.34	1.94	9.40	25.8
CV	88.7	67.0	13.9	80.0	69.7	53.1	81.0	10.8

*Some samples and its respective water quality parameters were not evaluated.

The TRCS showed pH values ranging between 5.50 (IBI2) and 10.1 (BB2), and temperature ranged from 21.1°C to 32.1°C considering the entire dataset. The highest SPM and Chl-*a* concentrations varied three orders of magnitude in TRCS, whereas PIM varied two orders of magnitude. BB2 reached the maximum concentrations (SPM = 44.0 $mg.L^{-1}$ and Chl-*a* = 797.8 $mg.m^{-3}$), whilst NAV1 reached the lowest SPM concentration (SPM = 0.1 $mg.L^{-1}$). The lowest Chl-*a* concentration was found in IBI1 (Chl-*a* = 1.4 $mg.m^{-3}$). The full TRCS dataset demonstrated high correlations between Chl-*a* and SPM concentrations, with $r = 0.95$ (p-value < 0.05). It is important to note that the Chl-*a* and particulate organic matter (POM) fractions showed $r = 0.94$ (p-value < 0.05, plot is not depicted here), whilst SPM and POM fraction showed $r = 0.99$ (p-value < 0.05). The SPM and PIM concentrations also showed significant statistical relations ($r = 0.67$, p-value < 0.05).

The PIM and POM concentrations showed an organic-to-inorganic standard from up-to-downstream reservoirs. Although the average proportions are similar between all reservoirs (Figure S.3.3.1), we observed expressive POM concentrations in BB and BAR compared to PIM concentrations as well as the expressive PIM concentrations in NAV (Table 3.2) compared to POM concentrations. Details about the inorganic-to-organic relation along the cascade reservoirs are presented in Supplementary Material (Figure S.3.1).

Inverse relationships were observed between water transparency (represented by Z_{SD}) against Chl-*a*, as well as the Z_{SD} against PIM, Z_{SD} against SPM and Z_{SD} against POM. Through the cascade, the Z_{SD} was slightly more influenced by SPM with $r = 0.70$ (p-value < 0.05) than Chl-*a*, PIM and POM (r = 0.66, 0.66 and 0.69, respectively). The minimum value of Z_{SD} was obtained in BB2 (= 0.37 m), and the maximum was found in NAV1 (= 4.80 m). Overall, the downstream reservoirs (NAV and IBI) presented higher Z_{SD}, and upstream reservoirs (BB and BAR) showed lower Z_{SD} values.

The boxplots (Figure 3.1) illustrated the water quality parameter gradients throughout the cascade system. High SPM concentrations were accomplished by the high Chl-*a* concentrations in upstream reservoirs (BB and BAR reservoirs in Figure 3.1 – a and b). The turbidity (Figure 3.1 – c) decays from the up-to-downstream (from BB to NAV), following the SPM and Chl-*a* concentration behaviors. The Z_{SD} is lower in reservoirs with high turbidity and it is higher in reservoirs with low turbidity, as expected (Figure 3.1 – d). Although the reservoirs demonstrated the interconnection process, the temperature and pH did not present any detectable pattern (boxplots are not shown).

Figure 3.1 Boxplot of water quality parameters obtained in each field campaigns: (a) SPM concentration (mg.L^{-1}); (b) Chl-*a* concentrations (mg.m^{-3}); (c) Turbidity (NTU); (d) Secchi Disk Depth (Z_{SD}, meters).

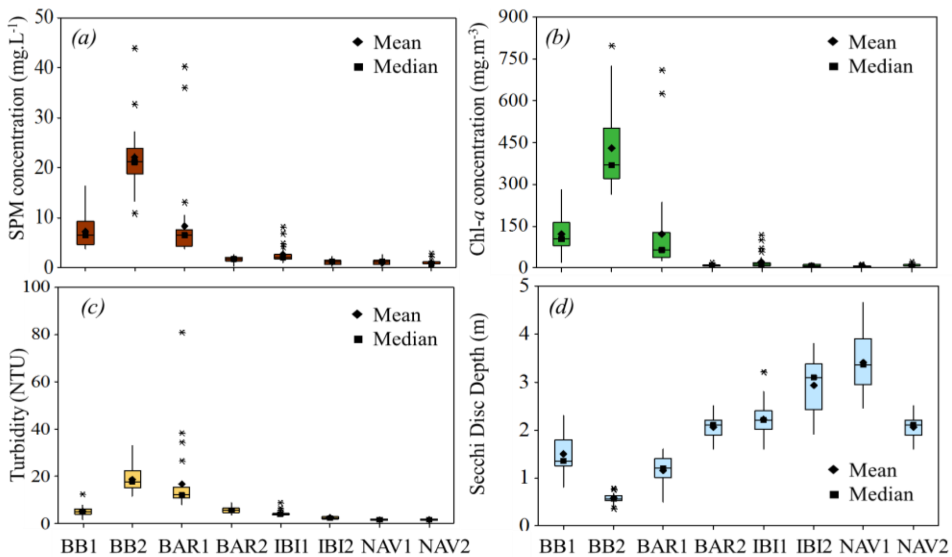

3.3.2 Trends of Absorption Coefficients

3.3.2.1 a_{cdom} throughout the TRCS

The CDOM absorption spectral curves for the TRCS dataset ($a_{cdom}(\lambda)$), with 175 sampling spots are depicted in Figure 3.2 (a), which followed the exponential fit as expected.

Regarding the TRCS values, the $a_{cdom}(443)$ ranged from 0.21 m^{-1}(NAV1) to 3.17 m^{-1} (BAR2), as shown in Table 3.2. The assessment of the CV depicted BAR2 with highest $a_{cdom}(443)$ variability (CV = 33.2%), and NAV1 with the lowest variability (CV = 8.5%). To quantify the distinct decay between the fieldwork, the slopes of CDOM (S_{cdom}) were calculated by fitting an exponential function and nonlinear least squares method. S_{cdom} comprised between 0.004 (in BB2) and 0.020 nm^{-1} (in NAV2) (Table 3.2). Although the S_{cdom} range for BB1, NAV1 and NAV2 are similar (0.016 - 0.018; 0.014 – 0.017; and 0.016 - 0.020 nm^{-1}), a paired t-test showed that S_{cdom} are different at 5% of significance. The same conclusion was obtained from comparisons between BB2 versus BB1, NAV1, NAV2, and between BAR1 versus IBI1.

Figure 3.2 In situ absorption spectra from all sampling locations for (a)a_{cdom}; (b)a_{p}; (c)a_{nap}; (d) a_{φ}.

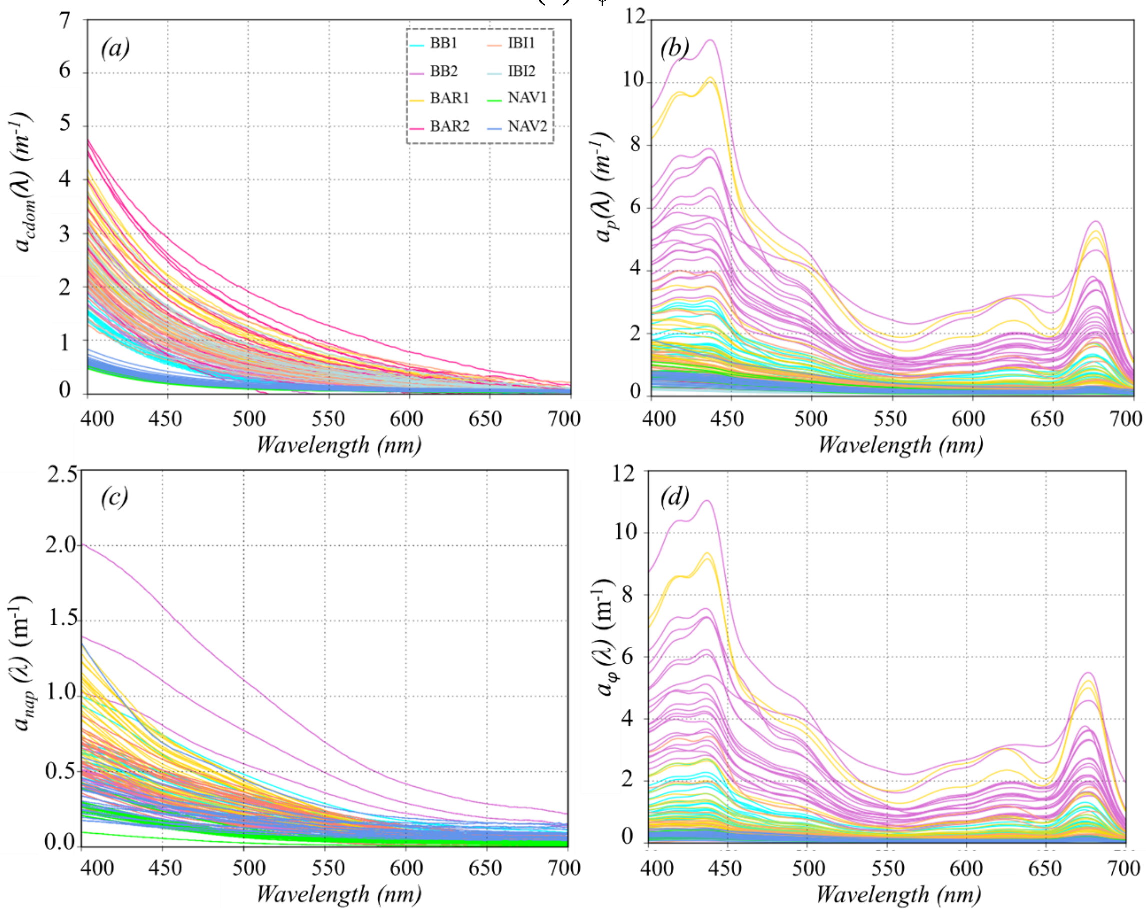

Table 3.2 Descriptive Statistics of $a_p(443)$ in m^{-1}, $a_\varphi(443)$, $a_{nap}(443)$, $a_{cdom}(443)$, NAP Slope (S_{nap}), and CDOM Slope (S_{cdom}). The exponential slope was obtained from CDOM within 400-700 nm of range.

		BB1	BB2	BAR1	BAR2	IBI1	IBI2	NAV1	NAV2
a_p (443)	Min	0.69	03.12	0.70	0.16	0.23	0.12	0.10	0.24
	Max	2.94	11.2	9.98	0.42	3.94	0.34	0.54	1.20
	Mean	1.67	5.15	1.99	0.30	0.80	0.21	0.22	0.52
	CV	38.90	27.10	64.70	25.90	54.10	38.40	60.40	25.60
a_φ (443)	Min	0.29	2.77	0.34	0.04	0.06	0.05	0.02	0.06
	Max	2.62	10.9	9.19	0.20	3.41	0.14	0.18	0.44
	Mean	1.21	4.67	1.41	0.12	0.42	0.09	0.06	0.25
	CV	52.30	31.90	64.70	28.20	89.50	33.30	72.80	31.80
a_{nap} (443)	Min	0.32	0.23	0.34	0.09	0.15	0.06	0.03	0.14
	Max	0.80	1.70	0.84	0.26	0.63	0.20	0.38	0.78
	Mean	0.47	0.49	0.58	0.18	0.39	0.12	0.12	0.27
	CV	25.30	76.50	22.70	25.90	27.40	48.30	71.20	34.00
a_{cdom} (443)	Min	0.45	0.77	1.12	0.32	0.72	0.77	0.26	0.24
	Max	0.97	1.35	2.46	3.17	2.23	2.29	0.54	0.47
	Mean	0.83	1.05	1.71	1.84	1.29	1.35	0.26	0.32
	CV	13.2	16.6	20.2	33.1	17.3	38.1	8.5	12.6
S_{cdom}	Min	0.016	0.004	0.010	0.009	0.006	0.011-	0.014	0.016
	Max	0.018	0.016	0.015	0.019	0.013	0.015	0.017	0.020
	Mean	0.017	0.012	0.012	0.013	0.009	0.013	0.015	0.018
	CV	3.2	19.6	10.2	10.9	23.8	8.8	4.5	5.7
S_{nap}	Min	0.008	0.006	0.010	0.009	0.008	0.005	0.008	0.003
	Max	0.011	0.009	0.012	0.011	0.014	0.022	0.011	0.007
	Mean	0.009	0.008	0.011	0.010	0.010	0.013	0.009	0.005
	CV	7.90	9.40	3.90	4.10	11.60	38.60	6.70	16.70

Regarding the frequency for all S_{cdom} values, the highest frequency was founded in the 0.010-0.014 nm^{-1} range (Figure S.3.2 – a). Moreover, investigations about relationships between S_{cdom} and $a_{cdom}(443)$ demonstrated statistically significant relationships in BB (both field studies) and IBI2 (Figure S.3.2 – b, c and d), with r values of -0.64, -0.87, -0.48, respectively. Other fieldwork showed weaker relationships, such as IBI1 (r = 0.45), and NAV1 (r = -0.37). BAR (both field studies) and NAV2 did not indicate a statistical relationship between $a_{cdom}(443)$ and S_{cdom}.

The relations between $a_{cdom}(443)$ versus Chl-*a* concentrations, and $a_{cdom}(443)$ versus SPM concentrations were also investigated. Considering the entire TRCS dataset, Chl-*a* and $a_{\mathrm{cdom}}(443)$ presented coefficients of correlation (R) = 0.15 (p-value < 0.05). However, taking into account each dataset separately, the relationships changes with BB1, BAR2, IBI2 and NAV2 (Figure S.3.3), showing significant relationships at 5% significance (r = 0.77, 0.66, 0.51, 0.61, respectively). Other field studies did not show relationships with statistical significance (BB2, BAR1, IBI1, and NAV1).

Considering SPM and $a_{cdom}(443)$ relationships, the entire TRCS dataset showed r = 0.20 (p-value <0.05). This scenery changes when field campaigns were individually considered. BB1, IBI1, and NAV1 showed r = 0.54, 0.49, and -0.06 (p-value < 0.05), respectively (graphs are not shown here). The other fields (BB2, BAR1 and BAR2, IBI2 and NAV2) did not show significant relationships between SPM and $a_{\mathrm{cdom}}(443)$.

3.3.2.2 a_p throughout the TRCS

All sampled particulate absorption spectra, $a_p(\lambda)$ are plotted in Figure 3.2 (b), and demonstrated time-fold variation, with highest magnitudes in BB2, BAR1 and BB1. The lowest magnitudes were found in BAR2 and IBI2. Considering inorganic and organic particle composition, it is worth highlighting that the phytoplankton absorption contributions to the $a_{\mathrm{p}}(\lambda)$ curves were mainly in BB (both field studies), due to absorption features at 443 nm and 675 nm; whereas, the inorganic absorption contribution can be highlighted in NAV (both field studies), due to the exponential shape of the absorption curves.

The values of $a_{\mathrm{p}}(443)$ for the TRCS dataset ranged from 0.10 m^{-1} to 11.2 m^{-1} (Table 3.2 for details). The highest variability was found in BAR1 (CV = 65%), and the lowest variability was encountered in NAV2 (CV=26%). In addition to the a_{p} curves, inorganic and organic particulate contributions were also evaluated by plotting the NAP ($a_{nap}(\lambda)$) and phytoplankton ($a_{\varphi}(\lambda)$) absorption spectra (Figure 3.2 – c and d, respectively).

The absorption of blue light ($a_{\varphi}(443)$) decreased markedly from the upstream site BB2 (10.9 m^{-1}) to the downstream site NAV1 (0.02 m^{-1}) (Table 3.2). The $a_{nap}(\lambda)$ curves did not present the same standard from up-to-downstream, with $a_{nap}(443)$ ranging between 0.03 m^{-1} (NAV1) and 1.7 m^{-1} (BB2) (Table 3.2).

Two highlighted absorption features are observed in Figure 3.2(d): one at 443 nm and another at 675 nm, which are due to Chl-*a* absorption. The highest magnitude of phytoplankton absorption was found in BB2, with $a_{\varphi}(443)$ = 10.9 m^{-1}, and $a_{\varphi}(675)$ = 5.44 m^{-1} (Table 3.2). The lowest magnitudes were found in NAV1 ($a_{\varphi}(443)$ = 0.02 m^{-1}) and BAR2 ($a_{\varphi}(675)$ = 0.004 m^{-1}). IBI1 depicted the highest variability among all field sites, with CV_{443nm} = 90% and CV_{675nm} = 95%.

Some fieldwork (IBI2, NAV1 and NAV2) did not show statistically significant relationships between Chl-*a* concentration and $a_{\varphi}(443)$ or $a_{\varphi}(675)$. BB1, BAR1 and IBI1 presented high relationships and did not vary the relation with wavelength (r = 0.90, r = 0.99, and r = 0.89, respectively at 443 nm and 675 nm). In BB2 and BAR2 fieldwork, relationships showed slight differences at each wavelength: at 443 nm, BB2 presented r = 0.64 and BAR2 presented r = 0.43; whereas at 675 nm, BB2 presented r = 0.54 and BAR2, presented r = 0.65 (BB2 and BAR2 plots can be found in Supplementary Information – Figure S.3.4).

Regarding $a_{nap}(\lambda)$ curves (Figure 3.2 - c), the exponential shape is a result of the isolation of residual pigment absorptions (Babin et al., 2003). This means that there were neither phytoplankton nor accessory pigments features in a_{nap} spectra. Among all field campaigns, only BAR1 and BAR2 depicted a remarkable change in magnitude for the entire spectrum dataset, demonstrating a considerable division between the two datasets (2-3 times magnitude of difference). IBI1 and IBI2 presented a slight overlap of some curves (lowest curves for IBI1 overlaps the highest curves for IBI2). Overall BB1 and BB2, and NAV1 and NAV2 presented high similarity among the curves, except for some samples that presented the highest magnitudes.

In terms of magnitude, BB2 showed the highest values for the entire spectra and NAV1 the lowest magnitude (Figure 3.2 – c). Among all field sites, the largest variability of $a_{nap}(443)$ was encountered in BB2, with CV = 77%, and the smallest variability was in BAR1, with CV = 23% (Table 3.2).

The entire cascade presented slope of nap spectrum (S_{nap}) values ranging between 0.003 m^{-1} and 0.023 m^{-1}. Statistical analysis for S_{nap} (Table 2) demonstrated that IBI2 presented the highest variability (0.005 $nm^{-1} < S_{nap} <$ 0.022 nm^{-1}, and CV = 39%), and the lowest variability was found in BAR (both fieldworks with CV = 4%). The frequency for the entire dataset of S_{nap} values was analyzed and showed a normal distribution, with the highest frequency in the 0.008 – 0.010 m^{-1} range. Relationships between $a_{nap}(443)$ and PIM concentrations were evaluated and a statistical relationship was found only in BAR1, with r = 0.50 (p-value < 0.05).

3.3.3 Relative contribution of OACs absorptions in TRCS

The a_t curves represent the sum of all individual OACs absorption spectra with the pure water absorption curve (a_w (λ), Smith and Baker, 1981), as described Equation 1. To identify each OAC absorption contribution to the total absorption without water (a_{t-w}), the average curves are plotted in Figure 3.3.

Figure 3.3 Average absorption coefficients by a_{cdom}, (high dashed line), phytoplankton (a_{φ}, dotted line), a_{nap},(low dashed line), and total non-water absorption (a_{t-w}, continuous line) for the (a)BB1; (b)BB2; (c)BAR1; (d)BAR2; (e)IBI1; (f)IBI2; (g)NAV1; (h)NAV2. Note the differences in Y-axis between the surveys.

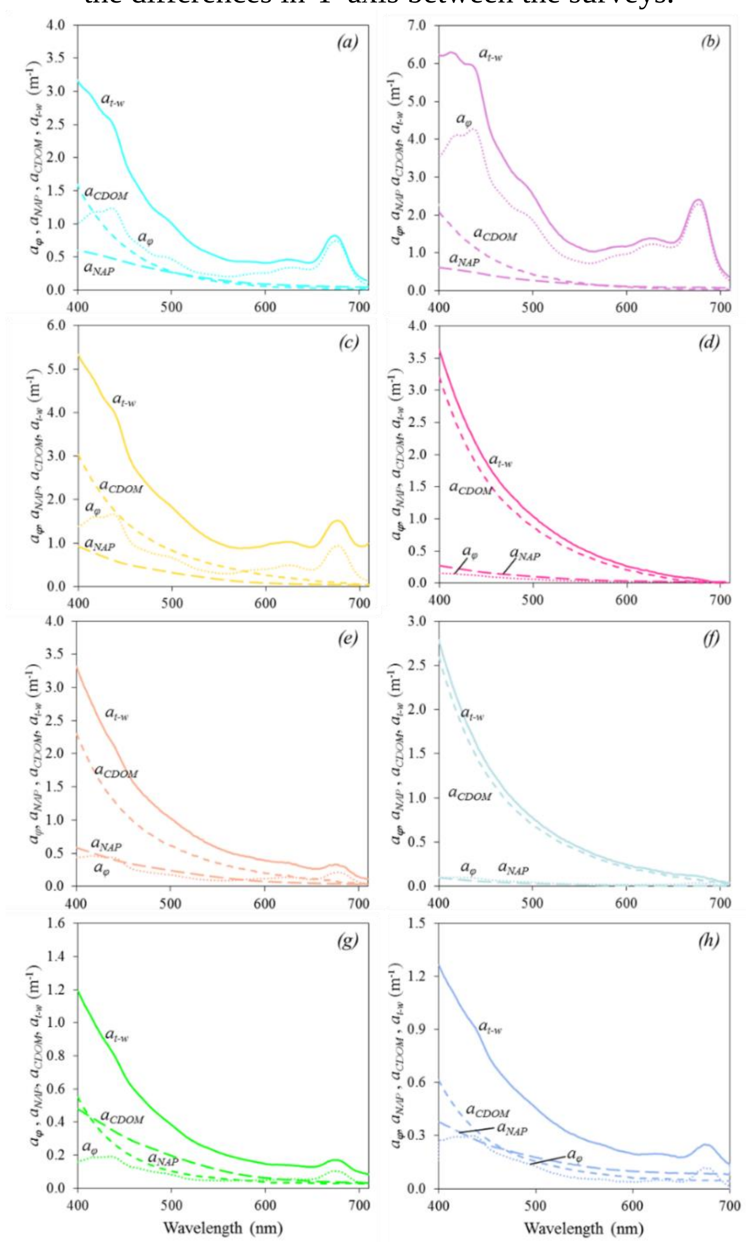

Regarding $a_{t\text{-}w}$, the BB (both study sites – Figure 3.3, a and b) dataset is markedly influenced by a_{φ}. BAR1 and BAR2 are distinctly different: BAR1 showed absorption features near 443 nm, 620 nm and 675 nm, resulting from a_{φ} contributions, while BAR2 presented a continuous exponential decrease along the spectra (Figure 3.3 – c and d). IBI1 presented smoothed features near 443 nm and 620 nm, derived from a_{φ} contributions (Figure 3.3 – e), whilst IBI2 presented an exponential decrease (Figure 3.3 – f). NAV1 and NAV2 (Figure 3.3 – g and h) depicted an exponential decrease with a_{nap} and a_{cdom} contributions up to 670 nm, where a_{φ} became expressive. NAV1 showed the a_{nap} predominance, and NAV2 presented a main contribution from a_{cdom}, mainly up to 450 nm.

To compare the spectral behavior throughout the cascade, Figure 3.3 was reorganized in comparative graphs, shown in Figure 3.4. The magnitude of $a_{\varphi}(\lambda)$ (Figure 3.4 – a) coincides with the order of reservoirs, since the magnitudes followed in the sequence of BB2, BAR1, BB1, IBI1, NAV2, and the remainder fields. The $a_{nap}(\lambda)$ presented varied magnitudes (Figure 3.4 – b), with BAR1 higher than BB2, BB1, IBI1, NAV1, NAV2, BAR2, and IBI2. The $a_{cdom}(\lambda)$ also did not show the up-to-downstream decay, with magnitudes varying in descending order from BAR1, BAR2, IBI1, IBI2, BB2, BB1, NAV2, NAV1 (Figure 3.4 – c).

Figure 3.4 Average absorption spectra of (a)a_{φ}; (b)a_{nap}; (c)a_{cdom} from all field surveys and respective OACs.

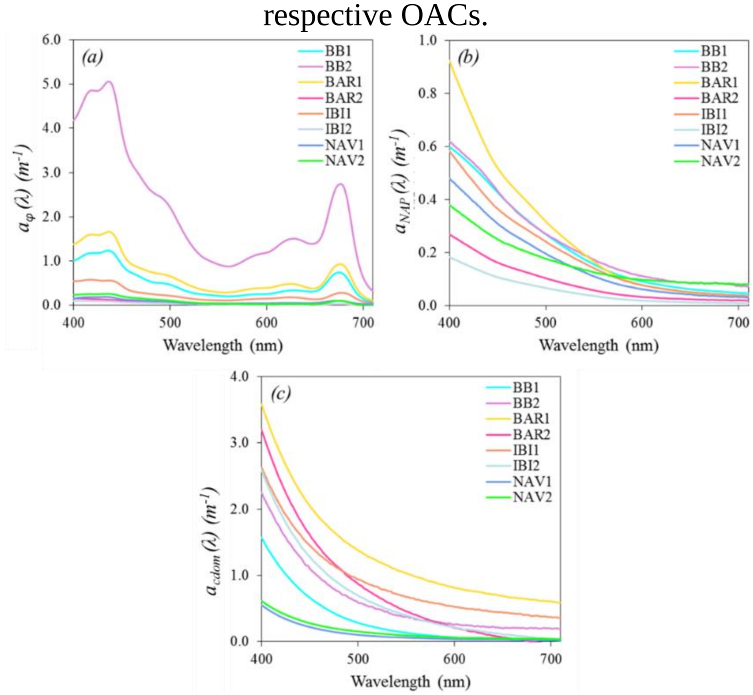

3.3.4 Absorption Budgets

The ternary diagram represented the OACs absorption contributions to the absorption itself ($a_{t-w}(\lambda)$) without water. Then, the diagrams were plotted in Figure 3.5 for the specific wavelengths of the Operational Land Imager sensor, onboard ongoing Landsat 8 (OLI/Landsat-8) - 443, 482, 560, and 655 nm. The OLI sensor was used because its images are suitable for inland water applications due to spatial resolution and revisit time (Pahlevan et al., 2014).

Figure 3.5 Ternary diagrams showing the contribution (%) of absorption coefficients to a_{t-w} at (a) 443; (b) 482 nm; (c) 560 nm; (d) 655 nm from all field surveys (BB1, BB2, BAR1, BAR2, IBI1, IBI2, NAV1, and NAV2).

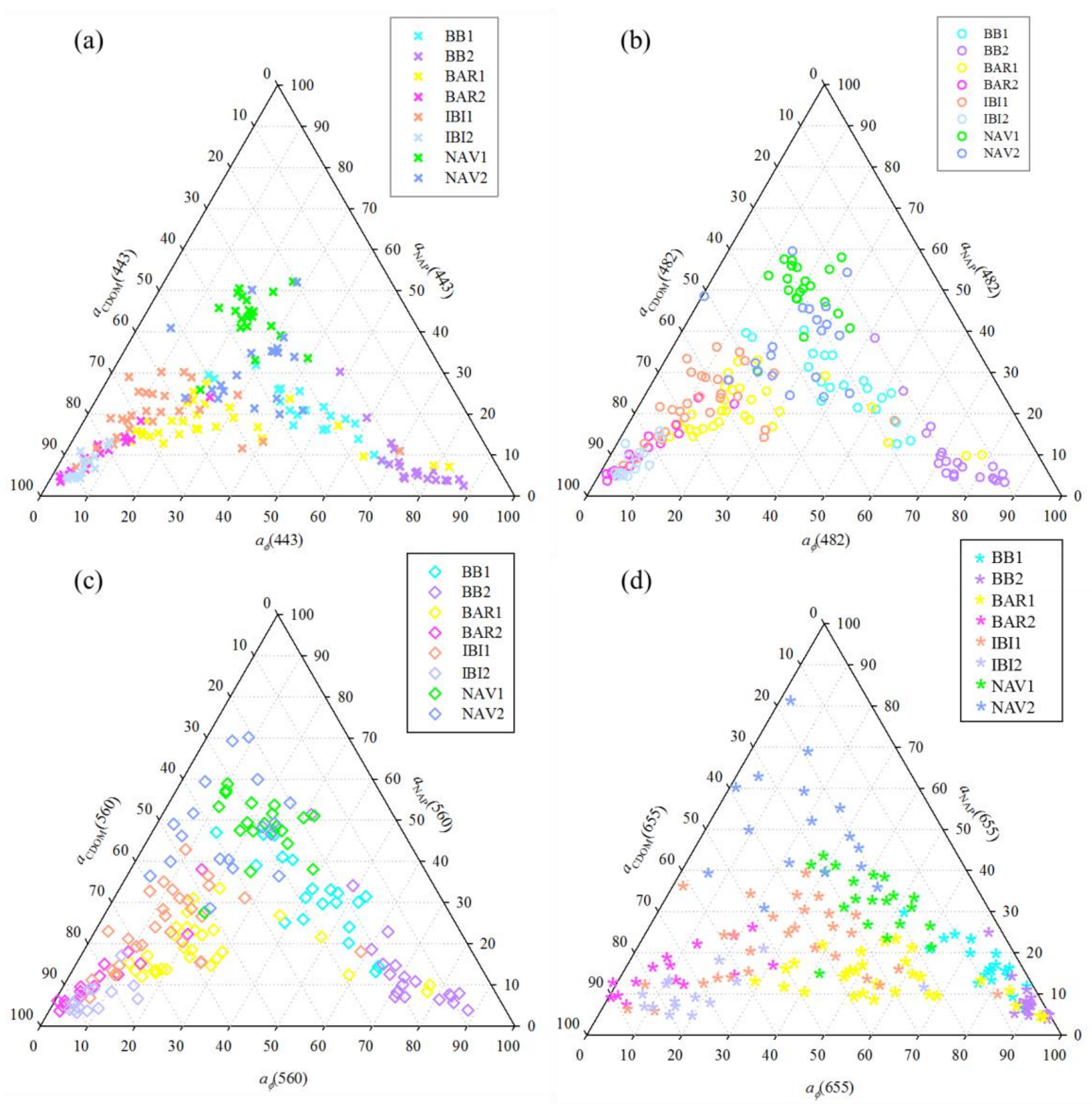

The $a_{t-w}(443)$ (Figure 3.5 – a) showed different OAC contributions in each reservoir. Overall, in BAR (both field studies) and IBI (both field studies) the major contributor was CDOM (averages of 53.3%, 82.74%, 64.9% and 87.30% for BAR1, BAR2, IBI1 and IBI2). In BB (both field studies), we identified a marked contribution from phytoplankton absorption (BB1: 20.7%-67.8%; BB2: 48.1%-87.9%). NAV1 presented a major influence of NAP (43.2%), whereas NAV2 presented high contributions from CDOM and NAP (39.4% and 31.7%, respectively). Considering the region of photossintetically active radiation (PAR – 400 to 700 nm range) and including the contribution of water to the total absorption, we maintain our findings for almost all field works, excepting NAV2 where water presented dominance of 41% against 30% from NAP (Table 3.3).

Table 3.3 Mean contribution of a_{cdom}, a_{φ}, a_{nap} and a_w to a_t within 400-700 nm of range.

	BB1	BB2	BAR1	BAR2	IBI1	IBI2	NAV1	NAV2
a_{cdom}	26.1%	19.0%	**40.5%**	**72.6%**	**49.0%**	**72.1%**	22.8%	18.6%
a_{φ}	**43.0%**	**68.9%**	37.4%	5.2%	21.3%	4.7%	16.7%	10.9%
a_{nap}	18.3%	7.4%	14.1%	8.1%	16.8%	6.3%	**31.2%**	29.8%
a_w	12.6%	4.7%	8.0%	14.1%	12.9%	16.9%	29.3%	**40.7%**

The $a_{t-w}(482)$ (Figure 3.5 – b), showed a high contribution of a_{φ} to BB (BB1: 40.07% and BB2: 73.06% of averages). The a_{cdom} contribution was predominant in BAR1, BAR2, IBI1 and IBI2 (averages of 54.6%, 82.5%, 63.5%, and 86.2%, respectively). NAP was dominant in NAV1 (30.4% - 58.0%), whereas NAV2 presented a slightly higher a_{φ} contribution (37.8%), when compared to a_{nap} (31.7%).

The $a_{t-w}(560)$ (Figure 3.5 – c), BB1 increased the dominance of a_{φ} (42% on average) and a_{nap} (32% on average) contributions. BB2 presented higher a_{φ} contributions (31.5% - 95.7%) and some samples showed a slight increase of NAP contributions. BAR1 presented a high CDOM contribution (30.1% - 77.6%) with two samples that showed remarkable $a_{\varphi}(\lambda)$ contributions (they also presented the highest Chl-*a* concentrations in the BAR dataset). BAR2 maintained a high contribution from CDOM (47.0% - 94.1%). IBI1 showed a strong influence by CDOM (41.4% - 90.5%), as well as IBI2 (74.3% - 91.8%); BAR and IBI datasets were clustered towards the CDOM apex (Figure 3.5). NAV1 is a_{nap}-dominant (contributions ranging between 28% and 70%) with one CDOM-dominated sample (a_{cdom} = 51.6%).

Overall, NAV2 conserved the high influence of a_{nap} (28.6% - 70.2%), with one CDOM-dominated sample (a_{cdom} = 58%).

The $a_{t\text{-}w}$(655) (Figure 3.5 – d) depicted a high influence by a_{φ} in BB1 (52.8% - 90.1%) and BB2 (73.2% - 96.1%). BAR1 was phytoplankton dominant (30.0% - 95.2%), with three samples that presented meaningful a_{cdom} contribution (a_{cdom}(655) > 50%), whilst BAR2 showed the predominance of CDOM (52.8% - 91.3%). IBI1 and IBI2 were CDOM dominant (with averages of 48.5% and 71.4%, respectively), one phytoplankton-dominated sample in IBI1 (a_{φ}(655)= 58.7%), and another sample displaced to the phytoplankton apex in IBI2 (a_{φ}(655) = 82.6%). NAV1 presented a homogeneous distribution among all OACs, with a remarkable a_{nap} contribution (30.5% on average) and a slight highlight of the a_{φ} contribution in some samples, which reached 60%. NAV2 was mostly dominated by NAP (34.0% - 79.4%).

3.3.5 Light Variability from up-to-downstream Reservoirs

To better represent the longitudinal variability of light absorption from upstream to downstream, the average values of a_{φ}, a_{nap}, a_{cdom} and $a_{t\text{-}w}$ at 443 nm are displayed in boxplot graphs (Figure 3.6). We considered 443 nm as a reference wavelength, due to its relation to dissolved organic matter concentration (Alcântara et al., 2016) and the marked Chl-*a* pigment absorption feature (Cetinic, 2018); furthermore, it is the central wavelength of the first OLI spectral band.

Figure 3.6 Boxplot of absorption coefficients at 443 nm obtained in all field campaigns: (a) $a_{\varphi}(443)(m^{-1})$; (b) $a_{nap}(443)(m^{-1})$; (c) $a_{cdom}(443)(m^{-1})$; (d) $a_{t\text{-}w}(443)(m^{-1})$.

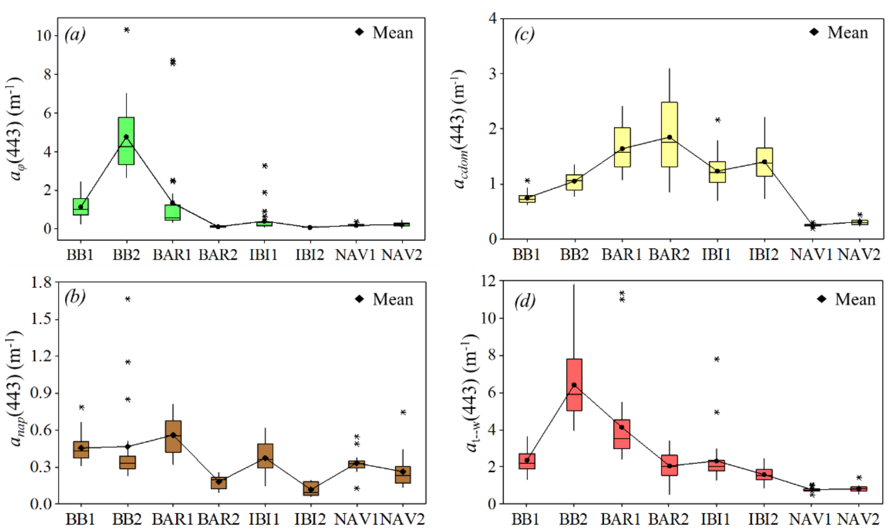

The light absorption decreases from up-to-downstream, following a similar pattern observed for OACs (see Figure 3.6). However, the absorption is very sensitive to OACs concentration at the time of water sampling. There is an increase in light absorption with higher concentrations and a decrease with lower concentrations. The $a_{cdom}(443)$ data showed that the BAR reservoir has more CDOM in the water than the BB reservoir, although both reservoirs had similar Chl-*a* concentrations. The $a_{nap}(443)$ showed the smallest longitudinal gradient of light absorption coefficients along the cascade. The $a_{t\text{-}w}(443)$ decreased from up-to-downstream and showed that phytoplankton was the main contributor to $a_{t\text{-}w}(443)$.

3.4 DISCUSSION

Evaluating optical properties throughout inland water systems that showed extreme upstream gradients is not an easy task (Massicote et al., 2017). There many variables that affect the hydrodynamic of hydroelectrical reservoirs, such as the hydraulic residence time of water (and fluctuation of water level), land use and cover use of drainage basin, wind, rainfall rates, runoff, and internal properties, including temperature, incident solar radiation into the water surface, and nutrients, for instance (Barbosa et al., 1999; Straškraba, et al., 1999). It is already known that absorption properties are proportional to the amount and diversity of optically active constituents within the water (Kirk 1994; Bukata, et al., 1995), however, the relations along cascading reservoirs with substantially different characteristics were not fully investigated in the literature.

All fieldwork was carried out in dry seasons (except IBI1) and at similar wind speeds. According to Tundisi and Matsumura-Tundisi (1990), water management leads to relatively high residence times during the dry seasons, and dry seasons normally present higher concentrations of Chl-*a* and suspended matter, due to high nutrient loads and light availability (Alcântara et al., 2016). The rainfall rates in BB did not vary too much when compared to the other fieldwork (Figure S.3.5- a) and presented high levels of Chl-*a*. The main cause can be attributed to the incident solar radiation onto the surface (Figure S.3.5 – b) in BB2, which is not as predominant in IBI2 and BAR2 (field studies that were carried out in June 2017).

The water residence times in each reservoir were: 30-180 days in BB; 7-24 days in BAR; 25-41 days in IBI; and 46 days (on average) in NAV. Similar Chl-*a* concentrations for

BAR1/IBI1 and BAR2/IBI2 are related to the low residence time similar length (BAR is almost 70 km long and IBI is 48 km) and comparable meanders along their course. Therefore, this suggests that both reservoirs are affected by the same environmental effects, since they show similar physical characteristics. They are geographically near (they are in sequence within the cascade), and they are located in drainage basins with similar developed activities (Periotto et al., 2018). The higher Chl-*a* concentrations in the BAR and IBI reservoirs, are a consequence of local discharges from respective tributaries. It is also reasonable to suggest that the high retention time and the proximity to urban areas, responsible for high discharges of nutrients and optimal conditions for phytoplankton growth, are the main causes of the high Chl-*a* concentrations found in BB (Watanabe et al., 2016). The low nutrient concentrations in NAV are responsible for the lack of phytoplankton development as much as bottom vegetation, due to river bottom nutrients, and the deeper euphotic zone (Smith et al., 2014; Rodrigues et al., 2017).

The most variable qualitative parameters were PIM (in BB1, BB2, BAR2, NAV1, and NAV2 field studies) and Chl-*a* concentration (in BAR1 and IBI1 field studies), with outliers of Chl-*a* concentration in BAR1 and IBI1 (Figure 3.2 - b). Outliers in BAR1 were the samples located in front of the Ribeirão Grande River - the tributary that receives wastewater discharges from Bauru city (Cairo et al., 2017), which did not have domestic sewage treatment at the time of the fieldwork (Figure 2.1 – f). The outliers in IBI1 are located in the convergence zone between the Jacaré-Guaçu River and the Claro River (Figure 2.1 – g), which are the main tributaries of the IBI reservoir. These results suggest the existence of regional nutrient inputs from tributaries, which modify the regional characteristics within the BAR and IBI reservoirs. Temperature and pH did not present gradients along the TRCS (Table 3.1), however, higher pH values were accomplished by higher Chl-*a* concentrations, which can be caused by intense phytoplankton activity that removes CO2 from aquatic systems and changes the pH, to values normally higher than 7.0.

Regarding the water quality parameters in TRCS, the Chl-*a* concentrations are highly related to POM ($r = 0.94$), and POM is highly related to SPM ($r = 0.99$). The inorganic fraction (PIM) demonstrated a weak relationship with SPM ($r = 0.67$); such a decrease can be the consequence of the NAV reservoir - an inorganic-dominated environment (Rodrigues et al., 2016). The variations of organic-to-inorganic particulate matter from up-to-downstream reservoirs are depicted in Figure S.3.1 (b) and demonstrated changes in water quality parameter composition. In this respect, it is also possible to note a qualitative change with high concentrations of SPM and Chl-*a* in the BB and BAR reservoirs and low concentrations in NAV and IBI (Figure S.3.1 – a and b).

Based on the organic to inorganic changes throughout the cascade, the results suggested higher $a_{\varphi}(\lambda)$ magnitudes in the upstream reservoirs, and lower $a_{\varphi}(\lambda)$ magnitudes in the downstream reservoirs. Such a trend was observed when absorption spectrum curves were evaluated (Figure 3.4 – a). As opposed to the phytoplankton and NAP absorption curves, the a_{cdom} spectra were investigated due to CDOM absorption effects on the available light for primary production (Kirk 1994).

The sources of colored DOM can be either autochthonous resulting from phytoplankton degradation that increases CDOM concentrations, or allochthonous resulting from carbon matter carried by the surrounding terrestrial basin drainage (Massicote et al., 2011; Lambert et al., 2016; Martins et al., 2018). Considering the amount of energy sampled during the field studies (Figure S.3.5 - b), we can note a trend in the relationships between high incident solar radiation and low levels of CDOM (represented by a_{cdom}(443 nm)) in NAV and BB (both field studies). The inverse is also validated – low levels of incident solar radiation and high levels of a_{cdom}(443 nm) were observed in BAR (both field studies) and IBI2. This trend is the result of the photochemical degradation of carbon organic matter due to light exposure, resulting in CDOM decreases (Vähätalo et al., 2004; Massicote et al., 2017). The exception, IBI1, presented high levels of CDOM accompanied by high levels of incident solar radiation, which indicates that the main source of carbon organic matter was high rainfall in July 2016 (Figure 3.1 - c). These high levels of CDOM could be the main factor that replaces photodegraded CDOM with terrestrial organic matter from the drainage basin and tributaries (Lambert et al., 2016).

The a_{cdom}(443) from the entire cascade ranged from 0.21 – 3.17 m^{-1} (Table 3.2), which is similar to other published studies for aquatic systems (Vishnu et al., 2018; Cairo et al., 2017; Riddick et al., 2015; Matthews and Bernard, 2013; Zhang et al., 2010; Carder et al., 1989). The highest a_{cdom} magnitudes were found in BAR1 and IBI1 (sampled curve in Figure 3.4 – c). The highest a_{cdom} curve in IBI1 was obtained at the same sampling location that presented the highest Chl-*a* concentration in the IBI1 dataset. Additionally, this sample is located near the Environmental Protection Area of Ibitinga, an area with high forest coverage and bog lake formations, resulting from wetlands of tributaries (Jacaré-Guaçu and Jacaré-Pepira Rivers – Figure 2.1 - g). More detailed information can be found in Figure S.3.6.

The exponential shape of a_{cdom} described in terms of S_{cdom} showed a narrow range between 0.006 nm^{-1} < S_{cdom} < 0.020 nm^{-1} in the TRCS. The S_{cdom} showed an inverse proportional relation to its molecular weight, represented by $a_{cdom}(443)$ (Kirk, 1994). The low values of S_{cdom} implies a high molecular weight of CDOM, whilst high values of S_{cdom} imply a low molecular weight (Carder et al., 1989; Twardowski et al., 2004). Such an inverse relationship between S_{cdom} and $a_{cdom}(443)$ can be related to CDOM photochemical degradations from phytoplankton (Helms et al., 2008; Matsuoka et al., 2013).

With the aim of investigating the sources of CDOM, we plotted $a_{cdom}(443)$ against Chl-*a* concentrations (Figure S.3.3). The plots can indicate if CDOM derived from autochthonous material (phytoplankton photobleaching) or from allochthonous material (riparian vegetation loads and runoff discharges) (Tilstone et al., 2013). The results showed that at least one field campaign from each reservoir presented a significant statistical relationship between Chl-*a* and $a_{cdom}(443)$ (BB1, BAR2, IBI2, and NAV2). Nevertheless, the relationships changed between the field studies, which suggested that CDOM origin varying. Moreover, the BB2 and BAR1 fieldworks did not show statistical relationships, even with high Chl-*a* concentrations, demonstrating that CDOM production is not dependent on the trophic status encountered within the aquatic system - BB and BAR are considered eutrophic environments.

The Chl-*a* concentrations, accessory pigments, and the different physiology states of phytoplankton assemblages are the main factors that modify the intensity and spectral position of features in $a_{\varphi}(\lambda)$ (Sathyendranath et al., 1987; Mobley et al., 1994). Due to the existence of absorption peaks and their spectral positions, it is possible to infer the types of phytoplankton and pigments encountered in a sample (Mobley et al., 1994).

The $a_{\varphi}(\lambda)$ peaks near 620 nm are related to phycocyanin, which is a pigment commonly present in cyanobacteria (Richardson 1996; Mishra et al., 2014). BB and BAR exhibited such feature in almost all $a_{\varphi}(\lambda)$ curves. Previous studies have related the dominance of cyanobacteria to phytoplankton assemblages in such reservoirs (Barbosa et al., 1999; Smith et al., 1999). At approximately 443 nm, the accessory pigments (Chl-*b,c*) and Chl-*a* are the major contributors to $a_{\varphi}(\lambda)$, whereas peaks at 675 nm result from Chl-*a* plus phaeophytin pigments (Sathyendranath et al., 1987). The features near 443 nm and 675 nm are remarkably observed in $a_{\varphi}(\lambda)$ curves obtained in BB (both field studies), BAR1, and IBI1; these features are less remarkable in NAV (both field studies) and disappear in BAR2 and IBI2 (Figure 3.4). A shoulder near 490 nm, encountered in some spectral curves in BB (both field studies), BAR1 and IBI1 indicates the presence of carotenoids in phytoplankton pigments (Perkins et al., 2014). The reduction in Chl-*a* concentrations directly affects the peaks near 440 nm and 675 nm in the a_{φ} curves (Figure 3.4), mainly in BAR1 and compared to those in BAR2 and IBI2. The total absorption is also influenced by such decay and, which demonstrates the relationship between phytoplankton production and the spectral absorption of available energy. The feature near 440 nm represents pigments accessories of phytoplankton (alfa and Beta carotene), while 675 nm feature represents Chl-*a*, *b* or *c* pigments. The variability of features observed in samples from different reservoirs indicate species richness of phytoplankton community along the cascade. Due to the different absorption peaks in $a_{\varphi}(\lambda)$ from up-to-downstream caused by high variability in Chl- *a* concentrations and package effects (Watanabe et al., 2017), it is not possible to categorize the reservoirs accordingly to the dominance of certain types of phytoplankton assemblages per reservoir. Conversely, it is possible to identify a longitudinal gradient of $a_{\varphi}(\lambda)$ magnitudes in TRCS (Figure 3.6 – a), as observed for Chl-*a* concentrations (Figure 3.2).

The $a_{nap}(\lambda)$ curves showed the iron oxides features between 450-550 nm (Estapa et al., 2012) in BAR, IBI and NAV fieldwork (Figure 3.4), which is consistent with the sandy soil formation in the drainage basin in the BAR and IBI reservoirs (Souza et al., 2000; Tundisi et al., 2008), and demonstrated the influence of sand extraction activities observed in the NAV reservoir during the field studies. The highest and lowest $a_{nap}(\lambda)$ average curves (Figure 3.4-b) are related to the average PIM concentrations (Table 1), as observed in BAR1 (2.30 $mg.L^{-1}$) and IBI2 (0.40 $mg.L^{-1}$), respectively. The $a_{nap}(\lambda)$ magnitudes depend on concentration and type of particles (Wòzniak et al., 2011; Meler et al., 2017). Despite the significant differences in S_{nap} in the fieldwork, these values are too small to hypothesize a water classification as a function of S_{nap}, such as the classification made in African Reservoirs (Matthews and Bernard, 2013).

The evaluation of the absorption contribution of each OACs to $a_{t\text{-}w}$ made by ternary diagram allowed for an understanding of the optical features in each reservoir. The ternary diagram is considered as a tool for water classification, due to sampling distributions along the three-axes (Case 1 or Case 2 type, Prieur and Sathyendranath, 1981). It is not our intention to classify the waters of the TRCS, but to properly understand what happens in absorption coefficients along the cascade. Overall, the results indicated that BAR and IBI reservoirs are CDOM-dominated environments, except for samples with high Chl- *a* concentrations (higher than 700 $mg.m^{-3}$). The CDOM-dominance was conserved through the spectra (at 443, 482, 560 and 655 nm) for the BAR and IBI fieldwork. BB (both field studies) is a phytoplankton-dominated environment, whilst NAV (both field studies) was identified as a NAP-dominated environment. Based on the average of contributions from each field, the reservoirs showed specific OAC dominances that were not wavelength dependent.

Considering 443 nm as a reference wavelength for plotting the absorption coefficient variation along the cascade (Figure 3.6), we observed a slight decrease in absorption from up-to-downstream, mainly in a_{t-w}(443). Furthermore, phytoplankton absorption acted as the major contributor of $a_{\mathrm{t-w}}$(443) and showed the same decreasing trend encountered for OAC concentrations (Figure 3.2). The increasing dominance of CDOM in the BAR and IBI (Figure 3.4 - c) showed a relevant enrichment of CDOM within these reservoirs. Considering that CDOM is the colored fraction of dissolved organic matter (DOM), and DOM is an important fraction of dissolved organic carbon (DOC) in inland waters, CDOM can be used as a useful indicator of DOM and DOC (Cole et al., 2007; Zhu et al., 2014). Therefore, the CDOM-dominance in BAR and IBI indicated high DOM and DOC concentrations, caused by internal production, in BAR2 and IBI2 (Figure S.3.3), and terrestrial sources as in IBI1, due to the runoff discharges driven by watershed contributions.

3.5 CONCLUSIONS

Understanding and interpreting bio-optical properties, such as IOPs, further the understanding of the underwater light field is essential to bio-optical modeling developments and accurate water quality monitoring applications. The present results allowed an analysis of the dynamics of a cascading reservoir system, showing the continuous longitudinal gradient of optical absorptions and OACs in TRCS. Variations of the magnitude of OACs affect the light absorption coefficients, mainly a_{φ} and a_{t-w}. From up-to-downstream, the

TRCS presented a slight decrease for NAP and CDOM absorption coefficients, and they showed more susceptibility to allochthonous effects.

a_{cdom} was the highly variable parameter within the cascade, mainly in the BAR and IBI reservoirs. The a_{cdom} spectra did not show a decaying trend along TRCS, instead it presented low magnitudes in BB and NAV and major magnitudes in IBI and BAR. The different magnitudes of the a_{cdom} curves among samples collected within the same reservoir indicate additional sources of CDOM throughout the aquatic systems; in other words, the tributaries and activities in nearby areas affect the optical properties within reservoirs as much as the water flow from previous reservoirs. NAP absorption presented a less remarkable decaying trend from up-to-downstream, with high variations in the BAR and IBI fieldwork that can result from the contribution of runoff sediments.

The longitudinal gradient of a_{φ} is proportional to the Chl-*a* concentration throughout the cascade and directly influences $a_{t\text{-}w}$, despite the individual optical dominance for each reservoir - BB is a phytoplankton-dominated environment; BAR and IBI are CDOM-dominant environments; and NAV is a NAP-dominant environment. Some exceptions to the dominance of OAC were found in specific sampling locations that showed distinct Chl-*a*, SPM or a_{cdom} values compared to the entire dataset. In these cases, the highest absorption contribution within the reservoir changed accordingly to the most expressive OAC.

The insights from this work demonstrated a longitudinal gradient of absorption coefficients that were directly affected by OAC variations throughout the TRCS. Moreover, CDOM and NAP are essential to watershed contributions as much as the internal characteristics (such as residence time, incident solar radiation, and so forth). Furthermore, the land use and land cover in watersheds provide nutrient enrichments and pollution discharges within the reservoirs and are reflected by OACs in specific locations, which affect the absorption coefficients. These local variations highlight the needs of local management to identify the main sources of higher OAC concentrations. The absorption variability found in TRCS confirms the challenges in retrieving OAC concentrations using a unique bio-optical model for the entire cascade. By contrast, our results highlighted the presence of a total absorption gradient and the strong influence of phytoplankton absorption on the total absorption along the aquatic continuum. Further analysis in a longer time series might provide temporal absorption coefficient datasets in TRCS and support strategies for bio-optical modeling in different optical conditions.

3.6 SUPPLEMENTARY INFORMATION

Fig. S.3.1	(a) Composition of SPM in fractions of PIM and POM for the entire dataset and respective samples in BB for Barra Bonita, B for Bariri, I for Ibitinga, and N for Nova Avanhandava reservoirs; (b) the average contributions of PIM/POM.
Fig. S.3.2	(a) Frequency distribution of the exponential slopes (Scdom) for all surveys; Scatterplot of $a_{cdom}(443)$ as a function of Scdom for (b)BB1, (c)BB2, and (d)IBI2 (fields that presented significant statistical relations).
Fig. S.3.3	Relationships between a_{cdom} (443) and Chl-*a* concentrations (mg.m-3) encountered in BB1 (a), BAR2 (b), IBI2 (c) and NAV2 (d).
Fig. S.3.4	Scatterplots of $a_{\varphi}(443)$ as a function of Chl-*a* concentrations in BB2 at (a)443 nm and (b)675 nm; and BAR2 at (c)443 nm and (d)675 nm.
Fig. S.3.5	(a)Plot of Monthly average rainfall (mm) from TRMM in 2014, 2016 and 2017 and respective fieldworks; (b) Average incident spectral solar radiation (Ed in $W.m^{-2}.nm^{-1}$) for each fieldwork
Fig. S.3.6	Absorption coefficients at OLI center wavelengths for (a) phytoplankton and Chl-*a* concentrations; (b) non-algae particles and NAP concentrations; and (c) colored dissolved organic matter in all fieldworks, where BB is Barra Bonita, BAR is Bariri, IBI is Ibitinga, and NAV is Nova Avanhandava reservoirs.

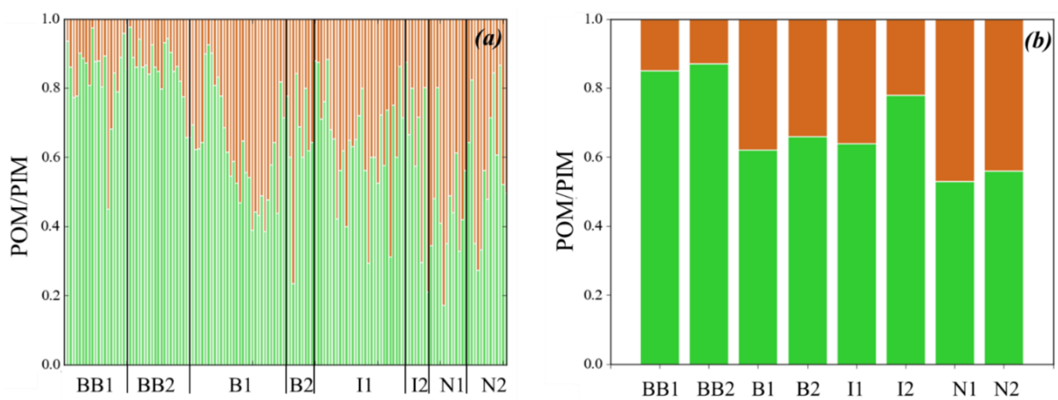

Figure S.3.1. (a) Composition of SPM in fractions of PIM and POM for the entire dataset and respective samples in BB for Barra Bonita, B for Bariri, I for Ibitinga, and N for Nova Avanhandava reservoirs; (b) the average contributions of PIM/POM.

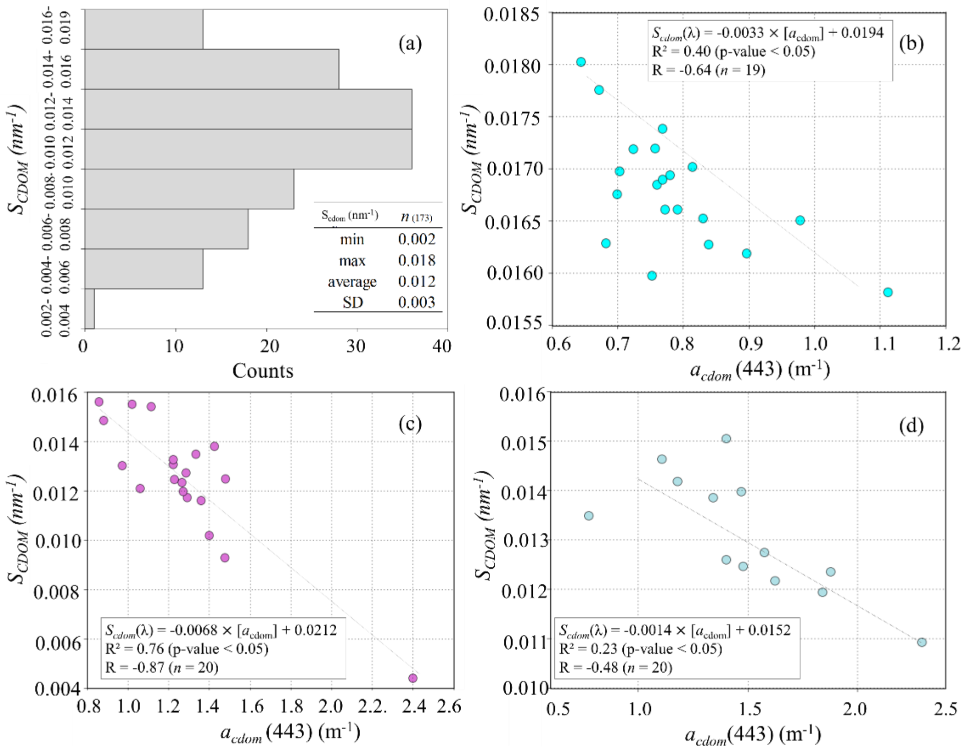

Figure S.3.2. (*a*) Frequency distribution of the exponential slopes (S_{cdom}) for all surveys; Scatterplot of $a_{cdom}(443)$ as a function of S_{cdom} for (*b*)BB1, (*c*)BB2, and (*d*)IBI2 (fields that presented significant statistical relations).

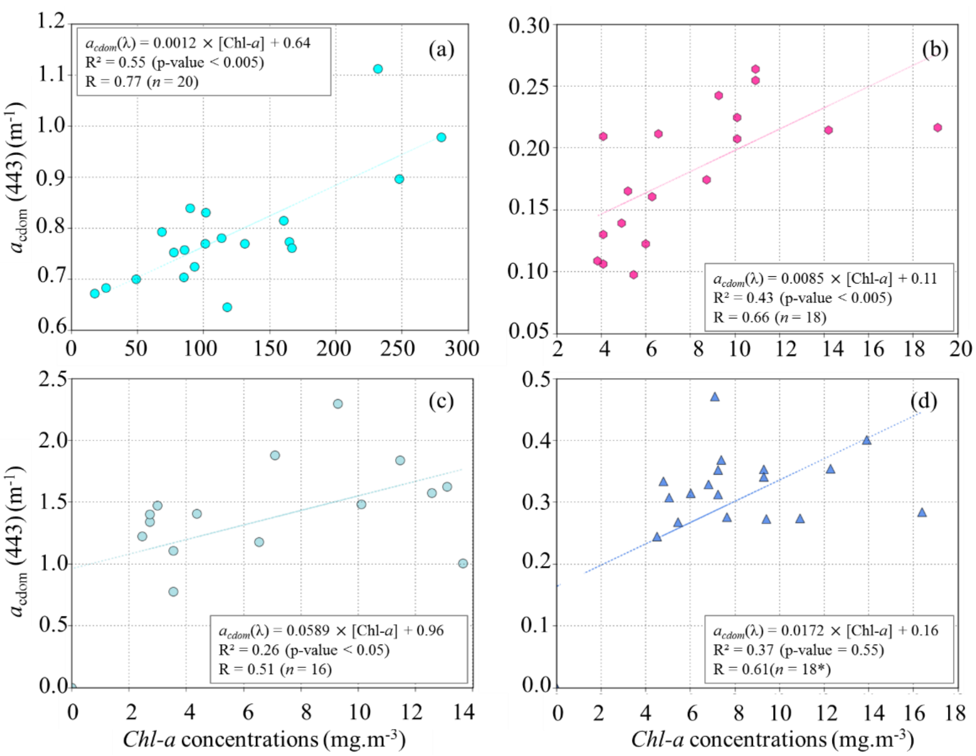

Figure S.3.3. Relationships between $a_{cdom}(443)$ and Chl-*a* concentrations (mg.m^{-3}) encountered in BB1 (*a*), BAR2 (*b*), IBI2 (*c*) and NAV2 (*d*).

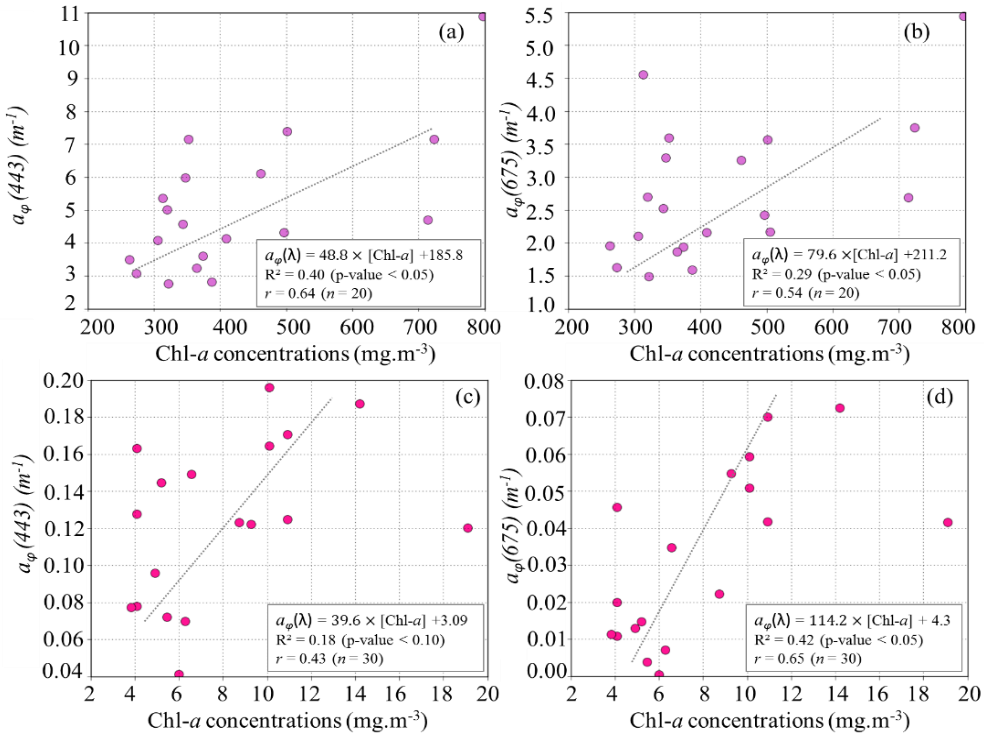

Figure S.3.4. Scatterplots of $a_{\varphi}(443)$ as a function of Chl-*a* concentrations in BB2 at (a)443 nm and (*b*)675 nm; and BAR2 at (*c*)443 nm and (*d*)675 nm.

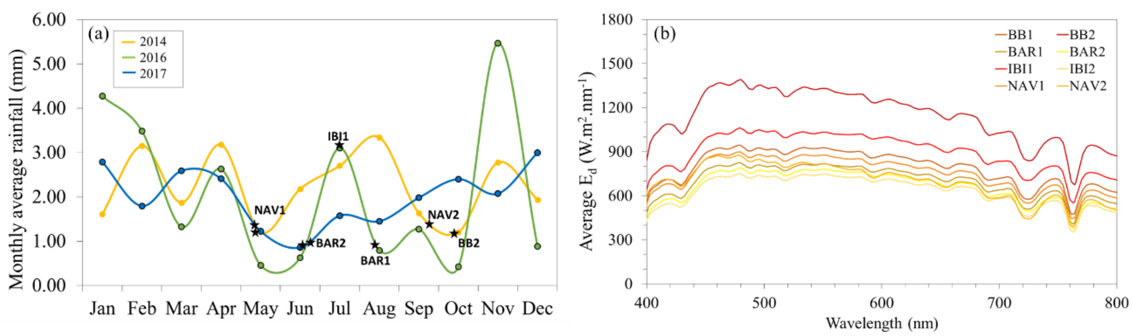

Figure S.3.5. (a)Plot of Monthly average rainfall (mm) from TRMM in 2014, 2016 and 2017 and respective fieldworks (the star near NAV1 is BB1; whilst the star near BAR2 is IBI2); (b) Average incident spectral solar radiation (E_d in $W.m^{-2}.nm^{-1}$) for each fieldwork.

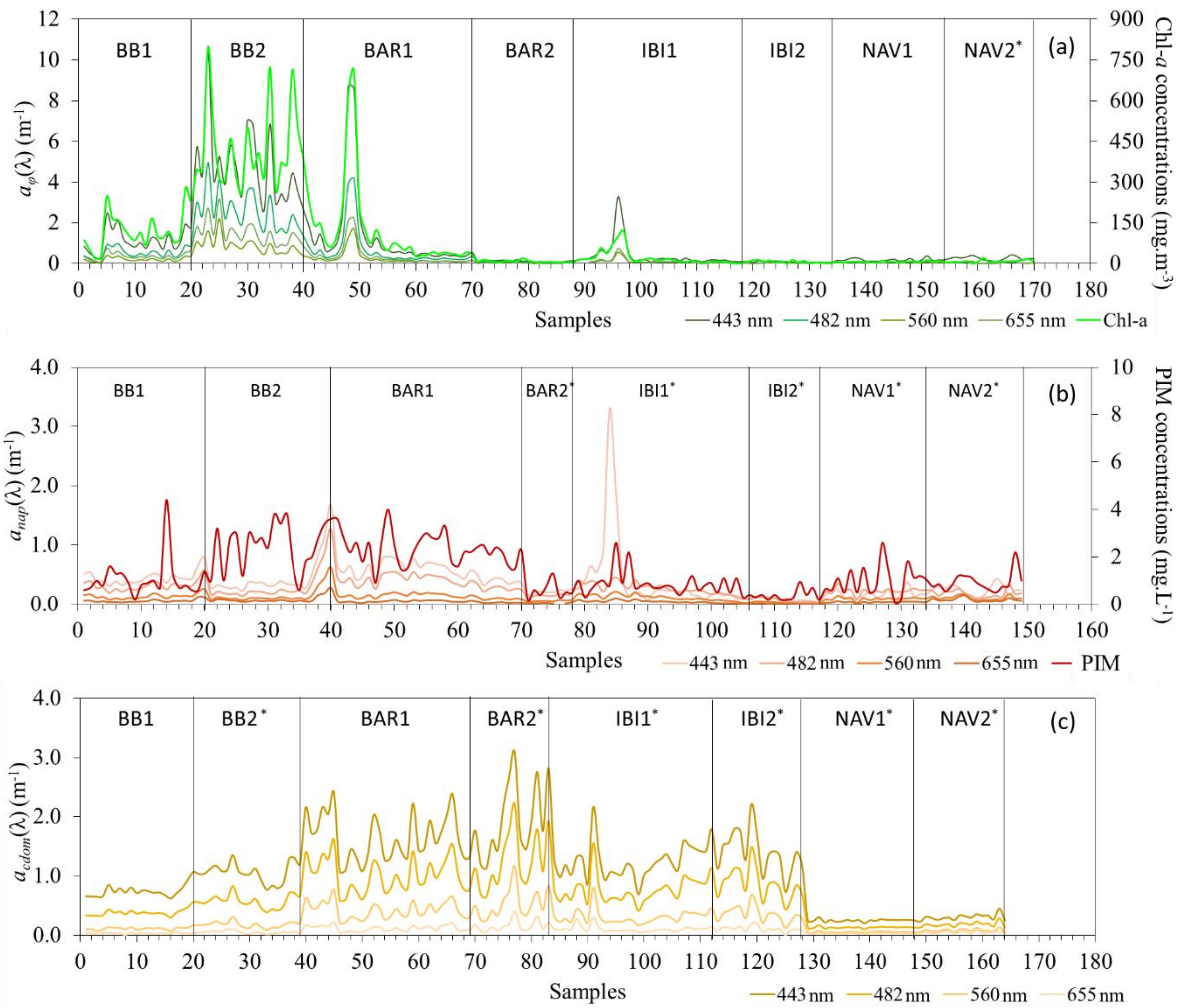

Figure S.3.6. Absorption coefficients at OLI center wavelengths for (a) phytoplankton and Chl-*a* concentrations; (b) non-algae particles and NAP concentrations; and (c) colored dissolved organic matter in all fieldworks, where BB is Barra Bonita, BAR is Bariri, IBI is Ibitinga, and NAV is Nova Avanhandava reservoirs.

CHAPTER 4: REMOTE SENSING REFLECTANCE DATA QUALITY

This chapter was published in the **Remote Sensing** Journal. doi: 10.3390/rs10101655

4.1 SCOPE

The quality assessment of remote sensing reflectances (R_{rs}) is an essential task due to the crucial role of R_{rs} products for water quality monitoring (Zibordi et al., 2012, Garaba et al., 2015, Zhang et al., 2017). In aquatic systems, targets that drive less than 10% of the radiometric quantities are registered by remote sensors (IOCCG, 2010). Radiometric quantities to compute R_{rs} should be carefully measured and post processing must be used to retrieve the most reliable optical information (Lee et al., 2010). The R_{rs} is defined as the ratio of water leaving radiance (L_w, $W.m^{-2}.sr^{-1}.nm^{-1}$) and the downwelling irradiance (E_d, $W.m^{-2}.nm^{-1}$) that reaches the water surface ($z = 0^+$) for a specific viewing geometry (θ, ϕ that represents zenithal and azimuthal angles, respectively). Likewise, the R_{rs} can be defined as the ratio of backscattering (b_b) to the b_b plus absorption (a), which are inherent optical properties (IOPs) (Gordon et al., 1975). Then, R_{rs} is mathematically described as Equation (4.1) (Mobley 1999).

$$R_{rs}(\theta, \varphi, \lambda) = \frac{L_W(\theta,\varphi,\lambda)}{E_d(\lambda)} \propto \frac{b_b(\lambda)}{b_b(\lambda)+a(\lambda)} \tag{4.1}$$

It is already known that L_w cannot be directly measured (Garaba et al., 2015; Lee et al., 2010; Mobley et al., 2015) without specific structures to block the surface glint. Therefore, L_w is calculated from measurable radiometric quantities. This means the total leaving radiance, $L_t(\theta,\varphi,\lambda)$, in $W.m^{-2}.sr^{-1}.nm^{-1}$, that reaches the sensor when it is pointed to the water surface, and the sky radiance, $L_{sky}(\theta,\varphi,\lambda)$, in $W.m^{-2}.sr^{-1}.nm^{-1}$, are measured when the sensor is pointed in the same plan as L_t but viewing the sky.

Relationships between all radiometric quantities are given by $L_t(\theta,\varphi,\lambda) = L_r(\theta,\varphi,\lambda) + L_w(\theta,\varphi,\lambda)$. Considering L_r as the radiance reflected by the water surface straight into the FOV (field-of-view) of the sensor and it is largely derived from L_{sky} into the water (Mobley

1999), L_r can be expressed as $L_{\mathrm{r}}(\theta,\varphi,\lambda) = \rho \times L_{\mathrm{sky}}(\theta,\varphi,\lambda)$. Therefore, we can re-write R_{rs} as follow:

$$R_{rs}(\theta,\varphi,\lambda) = \frac{L_t(\theta,\varphi,\lambda) - \rho \times L_{sky}(\theta,\varphi,\lambda)}{E_d(\lambda)} \quad (4.2)$$

where ρ (Equation 4.2) (defined as the ratio of the surface-reflected radiance at the specular direction corresponding to the downwelling sky radiance from one direction) is the water-surface reflected factor used to correct the surface radiance reflection or glint effect—one of the main constraints of above-water measurements (Ruddick et al., 2006). The ρ values depend on the viewing geometry of the sensor, environmental conditions (incident irradiance, solar zenith angle—SZA, wind speed, fetch effect), and atmospheric composition (aerosol, molecules, cloud coverage) (Fougnie et al., 1999; Mobley 1999; Gilerson et al., 2018). Besides, the more accurate estimate of ρ, the more accurate are the R_{rs} datasets for atmospheric correction validations, vicarious calibration of sensors, and bio-optical models (Gordon et al. 1975, Dev and Shanmugam, 2014).

The glint component did not provide information from an underwater light field, then, it might be removed from R_{rs} to the retrieve optical information about the optical components within a water column (Ruddick et al., 2006, Kay et al., 2009, Kutser et al., 2013). There are some strategies to minimize the surface reflected light, such as: (i) to take measurements below the water surface (upwelling radiance, L_u) and then extrapolate it to above water (Hooker et al., 2013, Wei et al., 2016); and (ii) to plug a black cone into the sensor's head to protect the readings from the surface reflection (Skylight-blocked approach—SBA in (Lee et al., 2013). Both strategies lead to particular constraints regard to calculus approximations and the self-shadowing of the cone, respectively.

Regarding the above-water measurements, methods to estimate the ρ values are capable of removing the influence of L_{sky} in the R_{rs} measurements. Simulations of a radiative transfer numerical model with several geometrical views, meteorological conditions, and IOPs showed that for wind speeds lower than 5 m.s^{-1}, clear sky conditions and specific viewing geometry (θ_v, φ_v = 40°, 90°), it is possible to assume a constant value of ρ = 0.028 (Mobley, 1999). However, such an assumption is dependent on the input parameters of the simulation and it did not take into account the spectral influence (Mobley 1999) or other cloudy conditions. Improved simulations considered the polarization ray effects and the water surface roughness (Mobley, 2015), however, the spectral dependence was not included in those runs.

In respect to the simulations and field measurements, other glint removal methods includes the wind speed variations and part cloud cover, resulting in ρ = 0.0256 for overcast skies, and for clear to partly cloudy skies the values of ρ and wind speed relations can cause more than two orders of variations (Ruddick et al., 2006). Then, the computations of ρ can be made using a proper equation where ρ values are described as a function of wind speed. However, this does not take into account spectral dependence and also suggests an offset correction for residual glint (ε) that can produce negative spectra for overcast sky conditions.

Facing the challenge of the spectral dependence of ρ, Lee et al. (2010) proposed a method that relied on spectral optimization (Lee et al., 2010). The method was established considering two reflectances: the total remote sensing reflectance ($T_{rs} = L_t/E_d$), and sky remote sensing reflectance ($S_{rs} = L_{sky}/E_d$). The initial guess of R_{rs} was done by using constant values of ρ, T_{rs}, S_{rs}, and a delta value (Δ, average of R_{rs} spectra from 750 to 800 nm) corresponding to a glint correction offset. Then, the initial guess of R_{rs} is optimized by using the hyperspectral optimization method (HOPE, (Lee et al. 2007; Lee et al. 2009). HOPE uses the IOPs (a and b_b coefficients) to derive a modeled R_{rs}. The HOPE outputs are used to compute the radiance reflectance just below the surface (r_{rs}), and it is extrapolated to the above-water surface reflectance (modeled R_{rs}). The difference between R_{rs} measured (using T_{rs} and S_{rs}) and R_{rs} modeled (using HOPE outputs) is considered as a bias that is adjusted until reaches the minimal value for producing the final value of Δ, its means, the best correction of glint, and most accurate R_{rs}.

The glint removal methods aim to remove, or at least minimize, the surface-reflected reflectance from R_{rs}. However, all aforementioned methods based their corrections into the simulations of radiative transfer models or specific spectral features of R_{rs}. Simulations of radiative transfer models require IOPs as inputs (Mobley, 2009 and 2015, Ruddick et al, 2006). In the case of spectral corrections of glint in Lee et al. (2010), absorption and scattering values are required to optimize the R_{rs} spectra and establish ρ and Δ (Lee et al., 2010). This method also uses L_t, which is the registered radiance from the aquatic system after the incident irradiance penetrates into the water column, interacts with optical active components (OAC) and water itself, and then re-emerges, passing through the surface until it reaches the sensor's view (sensors are pointed to the water surface to measure L_t). The IOPs are intrinsically related to the concentration and composition of OACs (Bukata et al., 1995), and L_t is the total radiance that reaches the sensor (partially due to surface reflectance and partially from the energy of water column after interacts with OACs and water itself) (Mobley 1999). The optically complex waters may affect the glint correction results, and consequently the R_{rs} accuracy, because the main steps of glint removal methods are dependent of L_t and IOPs that are directly related to concentrations of OACs within the water column.

The present work aims, therefore, to assess the methods to remove the glint effect in inland water systems with widely differing optical properties. While we sought to trace the glint effect, comparisons between in situ R_{rs} and R_{rs} orbital data that resulted from the Landsat surface reflectance code (LaRSC) of the Operational Land Imager sensor (OLI/Landsat-8) are also outlined, aiming to investigate the reliability of the glint removal method to provide valuable information for quality control of image data.

4.2 DATA AND METHODS

4.2.1 Radiometric Dataset

Optical measurements were made in situ, to gather radiance and irradiance measurements to compute R_{rs} and apply glint correction methods. In the laboratory the water samples collected at each sampling location established the absorption coefficients from the phytoplankton, non-algae particles, and colored dissolved organic matter, in addition to the total absorption coefficient.

The in situ measurements were made between 400 and 900 nm using TriOS Hyperspectral radiometers (RAMSES TriOS®; TriOS, Germany). L_t and L_{sky}, both in $W.m^{-}2.sr^{-1}.nm^{-1}$, were measured with ARC sensors that contained a 7° field of view, and 3.3 nm of the sampling interval. The downwelling irradiance incident onto the water surface (E_s, in $W{\cdot}m^{-}2.nm^{-1}$) and the downwelling irradiance below the water surface (E_d, in $W.m^{-2}.nm^{-1}$) were measured by an ACC sensor equipped with a cosine collector for registering the light within the hemisphere. Errors due to slight wavelength differences were avoided by linearly interpolating all the measurements at 1 nm spectral resolution before computing R_{rs}.

All field campaigns assumed the same geometric view and were set up to minimize the sun glint effect. Measurements of L_{sky} and L_t were made using the zenith solar angle (θ_v), which equaled 40° from zenith and the sensors were pointed towards nadir. An azimuthal angle (φ_v) of 90° (solar plan was considered the origin) was also adopted to avoid boat shadows and to minimize the specular radiance effects (Mobley 1999, Mueller 2000).

4.2.2 Inherent Optical Properties

Laboratory measurements were made to obtain the OAC's absorption features. Detailed description of the method used to retrieve absorption coefficients are described in Chapter 3, Section 3.2.2 – Laboratory analysis.

4.2.3 Remote Sensing Reflectance

The water color radiometry can be defined in terms of R_{rs}, which is strongly affected by the surface-reflected component since L_r is affected by the meteorological conditions, cloud coverage, and wind speed. Each facet of a wave is capable of reflecting the light into the sensor view (Lee et al., 2010). In order to correct the glint, the ρ factor acts as the probability factor to estimate the proportion of energy from the sky that will reach the water surface and reflect into the sensor.

Four approaches of glint removal of R_{rs} were evaluated to understand the impacts of "ρ factor" in different optical compositions. The first approach, hereafter M1, adopted $\rho = 0.028$ for all sampling spots (Mobley 1999); the second approach (M2) considered a ρ factor that changes according to the viewing geometry, acquisition time, and illumination geometry (Mobely 2015). The third approach (M3) used a ρ factor that is spectrally dependent (Lee et al., 2010); and the fourth approach (M4) used the ρ factor as a function of wind speed (Ruddick et al., 2006)

The M1 approach adopted $\rho = 0.028$ because it represents the maximum value of L_{sky} that will be reflected into the sensor. When the wind speed in the field was not higher than 5 $m \cdot s^{-1}$, the geometry view was $(\theta_v,\varphi_v) = 40°$, and 90° was maintained, the measurements were made under clear sky conditions. In addition, it is recommended that measurements be taken during the solar hour between 10 a.m.–2 p.m. (Mobley 1999).

The M2 approach was calculated based on the LUT (Look-Up-Table) of ρ values, which requires as inputs the wind speed (WS, in $m \cdot s^{-1}$), sun zenithal angle (SZA), and viewing geometry adopted from the sensors represented by φ_v and θ_v (Mobley 2015). The LUT of ρ results from several HydroLight simulations with several wind speeds, and geometries; although it was not analyzed, the values of the simulations are expressed in terms of quads that are greater than the areas comprised by the sensor's FOV. The differences between M1 (Mobley 1999) and M2 (Mobley 2015) are the methods used to simulate the water surface wave (Cox-Munk or Fourier transformation) and consider the polarization of light. Moreover, M2 takes into account the wave shadowing effect. The inputs for LUT were wind speed measured in situ by using a portable anemometer, the viewing geometry adopted as θ_v, φ_v = 40°, 90°, and the SZA calculated by Equation (4.3):

$$\mathrm{SZA} = \cos^{-1}(\sin\delta \times \sin\gamma + \cos\delta \times \cos\gamma \times \cos \mathrm{H}) \tag{4.3}$$

where δ is latitude from each sampling spot collected by Garmin GPS, γ is the solar declination calculated via the NOAA website (http://www.esrl.noaa.gov/gmd/grad/solcalc/), H is the sidereal hour retrieved by the difference between the sidereal hour at 0 h in the UTC system and the right ascension (α). H and α values were available from the Astronomic Annularly of the Brazilian National Observatory (2014, 2016, and 2017) and the values were interpolated considering the time zone for Brazil in each sampling spot. The values in LUT were used to compute R_{rs} using Equation (4.2).

The M3 approach considers a spectral ρ variation (Lee et al., 2010). As a premise, there is an initial guess of the reflectance value calculated by Equation (4.4):

$$\mathrm{R_{guess}} = \mathrm{R_{Fresnel}} - \Delta \tag{4.4}$$

where $R_{Fresnel}$ is the radiance reflectance computed with $\rho = 0.022$ and Δ is the $R_{mean(750–800\mathrm{nm})}$, i.e., an offset calculated as the mean of $R_{Fresnel}$ between 750 and 800 nm, that supposed to be set as zero for Case-1 waters and extended to longer wavelength intervals if the measurements longer than 800 nm were made for Case-2 waters. The step forward consists of using the hyperspectral optimization algorithm (HOPE) (Lee et al., 2002; Lee et al., 2013) for solving the inversion problem and modeling the total scattering (b), total absorption coefficients (a_t), and specific coefficients (a_w, a_{dg}, a_{phy}). These values of b, a_t, a_w, a_{dg}, a_{phy}, are used as inputs to compute the subsurface reflectance (r_{rs}) that is converted into remote sensing reflectance R_{rs} using Equation 4.5.

$$R_{rs} = \frac{0.52 \times r_{rs}}{1 - 1.7 \times r_{rs}} \tag{4.5}$$

The r_{rs} values are modeled on the HOPE solution. Considering the R_{rs} and R_{guess}, the called bias (Lee et al., 2010) represents the surface correction value, and can be computed as an objective function (Equation 4.6).

$$Error = \frac{\bigcup_{400}^{675}\left(R_{guess} - R_{rs}\right)^2 - \bigcup_{750}^{800}\left(R_{guess} - R_{rs}\right)^2}{\bigcup_{400}^{675} R_{guess} + \bigcup_{750}^{800} R_{Fresnel}} \tag{4.6}$$

With R_{guess} calculated from (4.4) and R_{rs} is calculated from (4.5), $\bigcup_{400}^{675}\left(R_{guess} - R_{rs}\right)^2$ is the square of mean reflectance from 400 to 675 nm, and $\bigcup_{750}^{800}\left(R_{guess} - R_{rs}\right)^2$ is the square of mean reflectance from 750 to 800nm. The Error (4.6) is computed for each adjustment until reaches the minimal value for producing the final value of Δ, initially assumed as $\Delta = R_{mean}$(750–800 nm).

It is important to highlight that if we used the assumptions of HOPE, which uses a_0 and a_1 coefficients to model the phytoplankton absorption coefficient, the interactions did not achieve the minimum value of Error, leading to high values of delta and the shape of spectra was negative. Then, we adjusted the method to use specific absorption coefficients (a^*_{phy}) instead of the modeled coefficient, then the values are closer to the real measurements and the interactions are converted into a minimum Error, resulting in corrected R_{rs} spectra, also named optimize reflectance values (R_{opt} -Equation 4.7).

$$R_{opt} = R_{Fresnel} - \Delta = \frac{L_t(\theta,\varphi,\lambda) - \rho(\lambda) \times L_{sky(\theta,\varphi,\lambda)}}{E_d(\lambda)} - \Delta \tag{4.7}$$

where the terms in Equation (7) are the total and sky radiances (L_t and L_{sky}), downwelling irradiance (E_d) and proportional coefficient of the sky reflected light (ρ). Δ is related to a residual glint correction, which means sun glint, whitecaps, and foam reflected light (Lee et al., 2010).

The M4 approach relies on sun sky conditions as well as features at 750 nm, where $L_{sky}(750)/E_d(750)$ were lower than 0.05 (from clear to partially cloud covered sky), the value of ρ is calculated as a function of wind speed (W, m.s^{-1}), as described in Equation (4.8), if the ratio is higher than 0.05, then ρ = 0.0256 and represented by an overcast sky. The main assumption is that reflectance is dominated by pure water absorption in near infrared (700–900 nm), therefore, a registered signal in this range results from glint (assuming no other sources of errors) (Ruddick et al., 2006):

$$\rho_{sky} = 0.0256 + 0.00039 \times W + 0.000034 \times W^2 \tag{4.8}$$

where W is the wind speed (m·s^{-1}) in each sampling location, and the coefficients in Equation (4.8) were obtained according to radiative transfer model simulations (Mobley 1999). Then, the values retrieved from Equation (4.8) were used to compute R_{rs} (Equation 4.2). The benefits and disadvantages from each glint removal method used in this work are accessed in Table 4.1.

Table 4.1 Features of tested glint removal methods (GRM).

GRM	Benefits	Disadvantages
M1 (Mobley 1999)	• Minimizes the skylight effects using Cox-Munk simulations for waves and unpolarized ray	• Spectral dependence of skylight and wind speed variations are not considered. • Simulations were developed for sea optical compositions.
M2 (Mobley 2015)	• Minimizes the skylight effects using wave spectral variance and considered the ray-polarization.	• Spectral dependence of skylight is not considered. • Desires additional information collected in fieldwork, such as wind speed and SZA computations.
M3 (Lee et al., 2010)	• Minimizes the sky and sunlight effects by using HOPE—semi-analytical scheme for retrieving IOPs.	• Needs additional information collected in fieldwork, such as the absorption and scattering coefficients.
M4 (Ruddick et al., 2006)	• Minimizes the skylight effect accordingly to the wind speed and was developed for turbid environments.	• Requires additional information about wind speed quantities. • Turbidity environments presented SPM concentrations ranged from 0.3–200 mg·L^{-1}

To compare which model performs better the HydroLight (version 5.2; Sequoia Scientific, Inc., Bellevue, WA, USA; Mobley, 2013) was used.

4.2.4 Hydrolight Simulations

HydroLight (version 5.2; Sequoia Scientific, Inc., Bellevue, WA, USA) is a radiative transfer numerical model capable of computing the radiance distribution, which relies on the inputs (IOPs and the OACs concentrations) and contour, such as the nature of the wind-blown water surface and the sky conditions. HydroLight produces an in-water light field, with outputs split into radiance components that allows us to compute the reference dataset of R_{rs} from 400–800 nm via Equation (4.1), removing the unwanted contributions, it means surface reflected light.

The most representative R_{rs} curves from each fieldwork were selected by applying the k-means, and then clustering results were compared to the sample curves by using a Spectral Angle Mapper (SAM, Kruse et al., 1993). Overall, a total of 24 of 175 R_{rs} curves (at least 2 curves from each field) were selected and 24 sampling spots with different optical features were used in HydroLight simulations.

HydroLight experiments were performed using a Case-2 model, where it is required to define concentrations and specific absorptions from four OACs (pure water, chlorophyll-bearing particles, CDOM, and mineral particle). We used the default IOPs of water that were relied on by Pope and Fry (1997) for absorption, and Smith and Baker (1981) for scattering. Specific coefficients of Chl-*a* and mineral particles were user-supplied (files with specific absorptions between 350–800 nm were set into the HydroLight), as well as the concentrations (in $mg \cdot m^{-3}$ and $g \cdot m^{-3}$) that were considered as constant with depth (we did not collect measurements along the water column). The CDOM component required the value of Slope (S_{cdom}) and the absorption at λ_0, considered at 440 nm.

The scattering model and phase function were kept as the default setup that represents the GAM model parameters and Petzold’s average-particle phase function (Gordon et al., 1975), respectively. Some sampling stations were simulated, including chlorophyll fluorescence. The inelastic scattering was not included in the runs. Besides, the geographical location used to compute the sun zenith angles, wind speed, water temperature, and acquisition dates was informed as an input of each sampling spot. For all simulations, we assumed a clear sky in RADTRANX, by using cloud cover equal to 0, and no atmospheric parameters were modified because we did not take measurements from the atmospheric composition. Infinite depth (no bottom contributions) and a spectral range of 400–800 nm ($\Delta\lambda$ = 1 nm) were defined. All inputs are summarized in Table 4.2.

Table 4.2 Inputs of Hydrolight of simulations using case-2 model.

OAC	Description	Notation	Unit	TRCS's Database	Test Data
Water	Number of R_{rs} spectra	N	-	175	24
	Wavelengths	λ	nm	400:1:900	400:1:800
	Absorption and scattering coefficients of pure water	a_w,b_w	m^{-1}	Pope and Fry (1997) and Smith and Baker (1981)	
	Water temperature	T	°C	21.1–39.4	21.8–29.2
Chlorophyll-bearing particles	Chlorophyll-a concentration	Chl-*a*	$mg.m^{-3}$	1.37–797.8	2.46–710.00
	Specific absorption coefficient	a^*_{phy}	m^2mg^{-1}	Laboratory data	
	Scattering coefficient Chl-*a*	b_{phy}	m^{-1}	Standard power law	
	Scattering phase function	β_{phy}	sr^{-1}	Average particle (Petzold's phase Function)	
Colored Dissolved Organic Matter (CDOM)	absorption coefficient of CDOM at 440 nm	$a_{cdom}(443)$	m^{-1}	0.20–2.29	0.20–2.20
	Slope of CDOM absorption	S_{cdom}	nm^{-1}	0.004–0.018	0.004–0.0172
Non-algae particles (NAP)	NAP concentration	NAP	$g.m^{-3}$	0.10–4.4	0.10–3.00
	Specific absorption coefficient at 440	a^*_{NAP}	m^2mg^{-1}	Laboratory data	
	Scattering coefficient by NAP	b_{NAP}	m^{-1}	Standard power law (Loiser and Morel near surface)	
	Scattering phase function	β_{NAP}	sr^{-1}	0.015–0.03	

The printout returned information about all of the parameters and inputs used during the runs. The outputs, written into ASCII files, were formatted to be read by spreadsheets in Excel (macros). Considering this option, we extracted the R_{rs} dataset from the outputs of HydroLight. Then, reference HydroLight R_{rs} (reference dataset) was compared to the in situ R_{rs} corrected by the four methods aforementioned.

4.2.5 Accuracy Assessment of R_{RS}

Considering several approaches to evaluate accuracy on R_{rs}, a better understanding is provided when we evaluated the optical closure between in situ measurements to the simulated data (Garaba et al., 2013); therefore, comparisons between R_{rs} calculated by M1, M2, M3, and M4 to the simulated R_{rs} assessed which method retrieved the most reliable optical information. The matching was evaluated using statistical errors–Root Mean Squared Difference, RMSD in sr^{-1}, normalized Root Mean Squared Difference, nRMSD in %, and Mean Absolute Percentage Error (MAPE, in %) (Equations (4.9 to 4.11).

$$RMSD = \sqrt{\frac{1}{n}\sum_{i=1}^{n}(x_{e,i} - x_{r,i})^2} \tag{4.9}$$

$$nRMSD = \frac{RMSD}{\left(\max(x_{m,i}) - \min\left(x_{r,i}\right)\right)} \times 100 \tag{4.10}$$

$$MAPE = \frac{|x_{e,i} - x_{r,i}|}{x_{r,i}} \times 100 \tag{4.11}$$

where $x_{e,i}$ and $x_{r,i}$ are the values estimated and measured R_{rs} from M1, M2, or M3 and simulated R_{rs} (reference data); max and min are maximum and minimum values. RMSD can be used for establishing random errors, such as environmental issues (Toole et al., 2000), whilst MAPE is used as a scatter factor of measurement, indicating systematic errors such as radiometric or platform errors.

4.2.6 OLI Assessment

OLI applications for inland water systems were recently investigated and demonstrated great results (Vanhellemont and Ruddick, 2015; Alcântara et al., 2016; Bernardo et al., 2017; Lehmann et al., 2018) due to their spatial resolutions that are able to represent significant details in hydrologic process in such environments. Besides, the Landsat dataset has demonstrated high suitability for inland and coastal studies (Pahlevan et al., 2013; Muow et al., 2015). Assessment of matching between the best glint removal of R_{rs} and the reflectance product of the Operational Land Imager (LaSRC) onboard Landsat-8 was performed. R_{rs}-glint removal based methods were spectrally convoluted (Equation 4.12) with the spectral response function (SFR) of each band of OLI centered at 593 nm, 482 nm, 561 nm, and 665 nm. The last band of OLI was not considered in our analysis due to the limitation of HydroLight simulations in the 400–800 nm range.

$$\mathrm{R}_{\mathrm{rs}}^{\mathrm{s}}(\lambda) = \frac{\int_{\lambda_{\min}}^{\lambda_{\max}} R_{rs}(\lambda)\mathrm{SFR}(\lambda)}{\int_{\lambda_{\min}}^{\lambda_{\max}} \mathrm{SFR}(\lambda)} \tag{4.12}$$

where R_{rs}^{s} is the convoluted in situ R_{rs} for OLI bands (centered at 443 nm; 482 nm; 561 nm and 655 nm), SFR is the spectral function response for each band (Barsi et al., 2014), and λ_{max} and λ_{min} are the longer and shorter wavelength in each OLI band. Then, the convoluted values of R_{rs} were compared to the R_{rs} from OLI images to assess if our glint removal dataset matches the OLI dataset. Considering that LaSRC retrieved the irradiance reflectance, the images were converted into R_{rs} by dividing them to π, and applying the scale factor of 10,000 (Bernardo et al., 2017). The images were also visually assessed in order to identify the presence of glint. None of them presented visual glint effects in the water surface.

The matching between in situ samples and image samples was made considering only in situ measurements that were taken at the same day that OLI overpass, corresponding to 34 sampling locations. A summarized flowchart of methodology is shown in Figure 4.1.

Figure 4.1 Methodological flowchart.

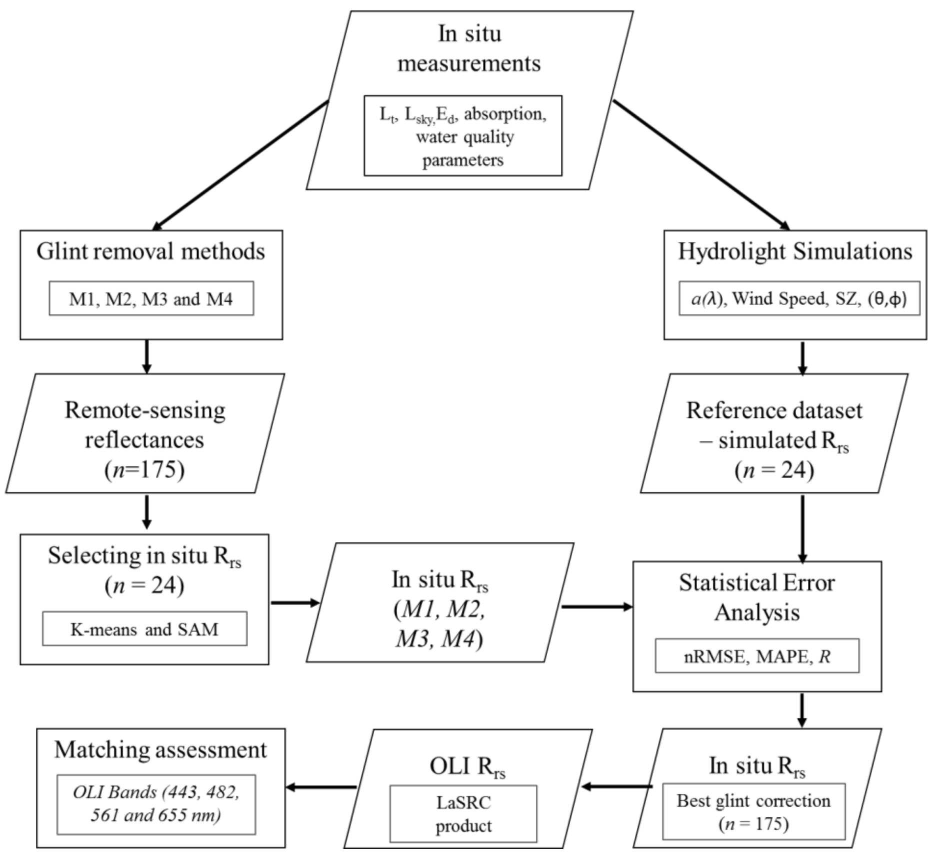

4.3 RESULTS

4.3.1 Water Quality Data and Optical Characterization

A wide variability of water quality parameters was observed in TRCS's dataset. The Chl-*a* concentration ranged from 1.37 mg.m^{-3} to 797.8 mg.m^{-3}, SPM ranged from 0.10 mg.L^{-1} to 44 mg.L^{-1} (Table 4.3), and most of the samples presented a high composition of particulate organic matter (POM), excluding the NAV's samples. Furthermore, Z_{SD} comprised between 0.37 and 4.80 m, whilst turbidity comprised between 1.01 and 80.9 NTUs (Table 4.3), leading to the most variable water quality parameter (CV = 88.7%). Except BB, the other fieldworks reached wind speeds higher than 5 m·s^{-1}.

Table 4.3 Descriptive statistics from all field campaigns carried out in TRCS. The notations are SPM - Suspended Particle Matter, PIM - Particle Inorganic Matter, POM - Particle Organic Matter, Aver -average, SD-Standard Deviation, Min-Max -minimum-maximum, CV- Coefficient of Variation.

		BB1 (n = 20)	**BAR1 (n = 30)**	**IBI1 (n = 30)**	**NAV1 (n = 20)**
SPM (mg·L^{-1})	Min-Max	3.6–16.3	3.6–40.3	1.0–8.1	0.1–2.6
	Aver ± SD	7.2 ± 3.3	8.3 ± 4.5	2.6 ± 1.0	1.0 ± 0.6
	CV (%)	45.2	54.8	39.2	61.7
PIM (mg·L^{-1})	Min-Max	0.2–4.4	0.9–4.0	0.3–2.6	0.1–2.2
	Aver ± SD	1.1 ± 0.9	2.3 ± 0.5	0.8 ± 0.3	0.7 ± 0.5
	CV (%)	78.8	21.4	35.3	76.7
POM (mg·L^{-1})	Min-Max	2.8–14.7	1.4–36.3	0.5–6.0	0.2–0.9
	Aver ± SD	6.1 ± 3.2	5.9 ± 4.5	1.8 ± 0.9	0.5 ± 0.2
	CV (%)	52.0	75.1	49.6	40.8
Chl-*a* (mg·m^{-3})	Min-Max	17.7–279.9	25.7–709.9	1.4–119.0	2.5–12.6
	Aver ± SD	120.4 ± 70.3	119.8 ± 96.4	21.8 ± 18.7	6.2 ± 2.5
	CV (%)	58.4	80.5	86.0	40.0
Turbidity (NTU)	Min-Max	1.7–12.5	7.8–80.9	2.8–8.9	1.0–2.5
	Aver ± SD	5.2 ± 2.4	16.6 ±7.6	4.3 ± 0.8	1.7 ±0.4
	CV (%)	47.0	45.8	17.9	25.4
Z_{SD} (m)	Min-Max	0.8–2.3	0.5–1.6	1.6–3.2	2.3–4.8
	Aver ± SD	1.5 ± 0.4	1.2 ± 0.2	2.2 ± 0.2	3.2 ± 0.6
	CV (%)	28.9	20.0	10.9	20.0
Wind Speed (m·s^{-1})	Min-Max	0.6–4.9	0.5–8.0	0.0–6.0	2.0–6.4
	Aver ± SD	1.8 ± 1.1	2.5 ± 2.3	2.2 ± 1.2	3.6 ± 1.3
	CV (%)	57.8	90.3	54.5	36.8
		BB2 (n = 20)	**BAR2 (n = 18)**	**IBI2 (n = 16)**	**NAV2 (n = 20)**
SPM (mg·L^{-1})	Min-Max	10.8–44.0	0.20–2.6	0.20–2.20	0.50–2.80
	Aver ± SD	21.9 ± 7.04	1.6 ± 0.44	1.06 ± 0.57	1.00 ± 0.38
	CV (%)	32.0%	42.4	53.5	37.6
PIM (mg·L^{-1})	Min-Max	0.6–3.8	0.20–1.30	0.20–1.00	0.30–1.10
	Aver ± SD	2.60 ± 0.96	0.60 ±0.24	0.40 ± 0.24	0.50 ± 0.14
	CV (%)	37.3	42.4	61.8	26.5
POM (mg·L^{-1})	Min-Max	10.2–30.4	0.40–1.60	0.30–1.90	0.14–2.00
	Aver ± SD	18.2 ± 4.8	1.10 ± 0.32	0.93 ± 0.46	0.50 ± 0.34

	CV (%)	26.2	28.8	49.8	65.8
Chl-*a* ($mg \cdot m^{-3}$)	Min-Max	263.2–797.8	3.8–19.0	2.50–13.7	4.51–20.5
	Aver ± SD	428.7± 154.5	8.0 ± 3.27	6.64 ± 4.46	9.01 ± 3.15
	CV (%)	80.5	40.9	67.2	34.9
Turbidity (NTU)	Min-Max	11.6–33.2	3.50–8.80	1.85–3.60	1.01–2.56
	Aver ± SD	18.6 ± 7.6	5.70 ± 1.25	2.47 ± 0.52	1.73 ± 0.33
	CV (%)	45.8	10.9	21.1	18.9
Z_{SD} (m)	Min-Max	0.37–0.78	1.60–3.20	1.90–3.80	0.37–4.80
	Aver ± SD	0.57 ± 0.10	2.20 ± 0.19	2.90 ± 0.57	1.15 ± 1.12
	CV (%)	17.2	10.9	19.5	88.7
Wind Speed ($m \cdot s^{-1}$)	Min-Max	0.0–5.0	0.0–6.5	0.0–6.5	0.0–5.6
	Aver ± SD	1.5 ± 1.4	3.0 ± 1.7	4.0 ± 1.9	2.9 ± 1.6
	CV (%)	99.2	56.3	47.1	55.7

The optical contributions from each OAC to the total absorption disregarding water itself ($a_{t\text{-}w}$ (λ)) were plotted in ternary diagrams (Figure 4.2) using the central wavelength of OLI bands. Each reservoir demonstrated specific OACs dominance. Furthermore, the light absorption budgets for each reservoir did not change along the wavelengths, it means, the OACs dominance were not spectrally dependent.

Based on average contributions from all wavelengths, BB1 and BB2 presented dominance of a_{phy} (51.1 ± 12.2% and 72.2 ± 10.6%), followed by a_{cdom} (25.3 ± 6.1 and 19 ± 6.9), and a_{nap} (23.6 ± 7.5 and 8.8 ± 7.6). BAR1 and BAR2 were CDOM-dominated (a_{cdom} of 65.9 ± 15.4% and 80.2 ± 11.9%), whilst a_{phy} (22.4 ± 16.1% and 8.2 ± 6.2%) and a_{nap} (11.8 ± 3.9% and 11.6 ± 6.4%) were not too expressive in the budget absorption. IBI1 and IBI2 also presented the highest contribution of a_{cdom} (67.3 ± 14.5% and 82.6 ± 7.6%), followed by a_{phy} (17.7 ± 11.7% and 9.5 ± 5.1%), and a_{nap} (15.1 ± 7.1% and 7.9 ± 3.8%). NAV1 and NAV2 showed a remarkable NAP contribution (43.1 ± 7.1% and 40.1 ± 10.8%), followed by a_{cdom} (29.4 ± 6.8% and 32.9 ± 10.5%) and a_{phy} (27.6 ± 7.3 and 25.7 ± 10.3%).

Figure 4.2 Ternary diagrams of absorption coefficients at 443 (a), 482 nm (b), 560 nm (c) and 655 nm (d) from all field surveys (BB1, BB2, BAR1, BAR2, IBI1, IBI2, NAV1, and NAV2). Where a_{φ} is related to phytoplankton absorption, a_{NAP} to non-algae particle absorption and a_{cdom} is related to the absorption from colored dissolved organic matter.

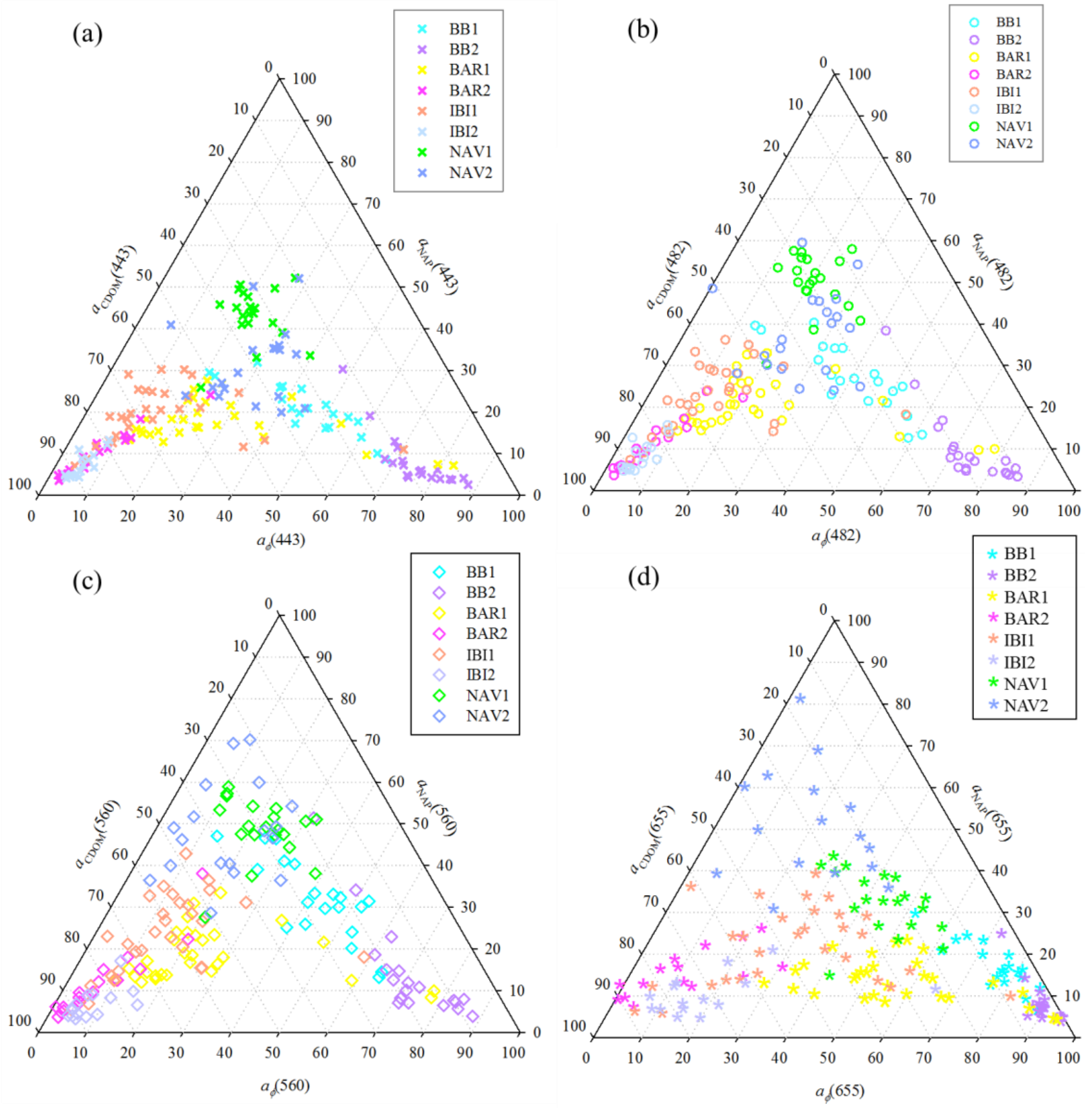

4.3.2 R_{RS} from M1, M2, M3 And M4 Approaches

Overall, the most variability was found in the NIR range (700–800 nm), where we observed that M3 showed the lowest magnitudes of CV (not valid for BB reservoir), it means that in the NIR range the R_{rs_M3} provided the lowest variation among sampled curves, or rather, the most clustered curves in the NIR interval. Furthermore, NAV showed a marked reduction in all spectra magnitudes by M2 and M3 approaches (Figure 4.3 g,h). The same occurred in BAR curves when we used the M3 glint removal method (Figure 4.3 – e).

It is possible to observe that R_{rs} curves presented several features along the spectra that changed for each fieldwork. Regardless of approach, the spectral features are conserved along 400–800 nm, varying only in magnitude. In order to quantify such variations along the spectra, we computed the CV for each 20 nm of range and Figure 4.3 represent them in graphs.

Similar results were obtained from M1 and M2 approaches in terms of CV and standard deviations (SD) for almost all fieldworks (Figure 4.3). The highest variations of R_{rs} were found in BB fieldworks for M3 in NIR ranges (700–800 nm), and NAV2 (Figure 4.3 a,b,h), which are the opposite results compared to the other reservoirs (BAR1, BAR2, IBI1, IBI2, NAV1) that presented M3 as the approach with minimums CVs.

The assessment of glint methods was made comparing the achieved results to the HydroLight simulations. However, to simulate the entire dataset composed by 175 spectral curves would imply a lot of time consumption and computational processing. Aiming to optimize the simulations, a group of representative samples was selected by using k-means to organize the entire dataset in clusters. Then, the most similar in situ spectra selected with the clustered data by using SAM. A total of 24 spectra were selected for HydroLight simulations/comparisons. We take care to select at least three samplings from each field—one sample near to the highest concentration of SPM, the other one near to the lowest concentration, and another one near to the average.

Figure 4.3 Coefficient of variation (CV) of R_{rs} derived from glint removal methods M1 (Mobley 1999), M2 (Mobley 2015), M3 (Lee et al., 2010), and M4 (Ruddick et al., 2006) in (a) BB1, (b) BB2, (c) BAR1, (d) BAR2, (e) IBI1, (f) IBI2, (g) NAV1, and (h) NAV2. The error bars indicate the standard deviation (SD, sr^{-1}) from each fieldwork rescaled by a factor of 100 (SD × 100).

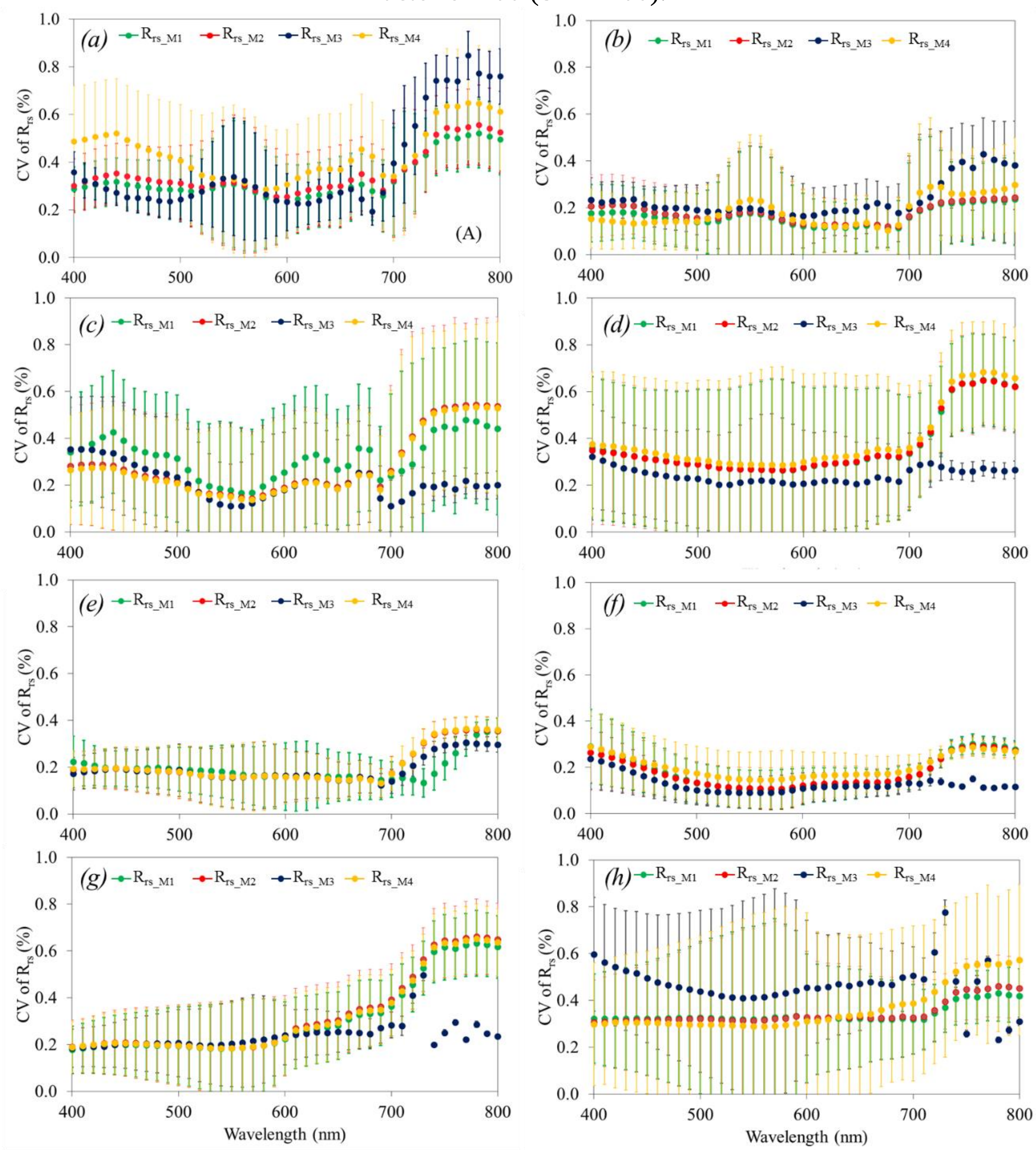

The plots from specific central wavelengths of OLI are shown in Figure 4.4, as well as the error assessments of glint removed-R_{rs} are shown in Table 4.4. The OLI images were chosen because they were suitable for inland water studies due to their spatial and temporal resolutions (Palmer et al., 2015).

Figure 4.4 Plots of HydroLight simulations (R_{rs_Hydro}) against (a) M1; (b) M2; (c) M3; and (d) M4 glint corrected R_{rs}. Highlight: R_{rs} datasets (in situ and simulated, n = 24) were spectral resampled for OLI bands for comparisons.

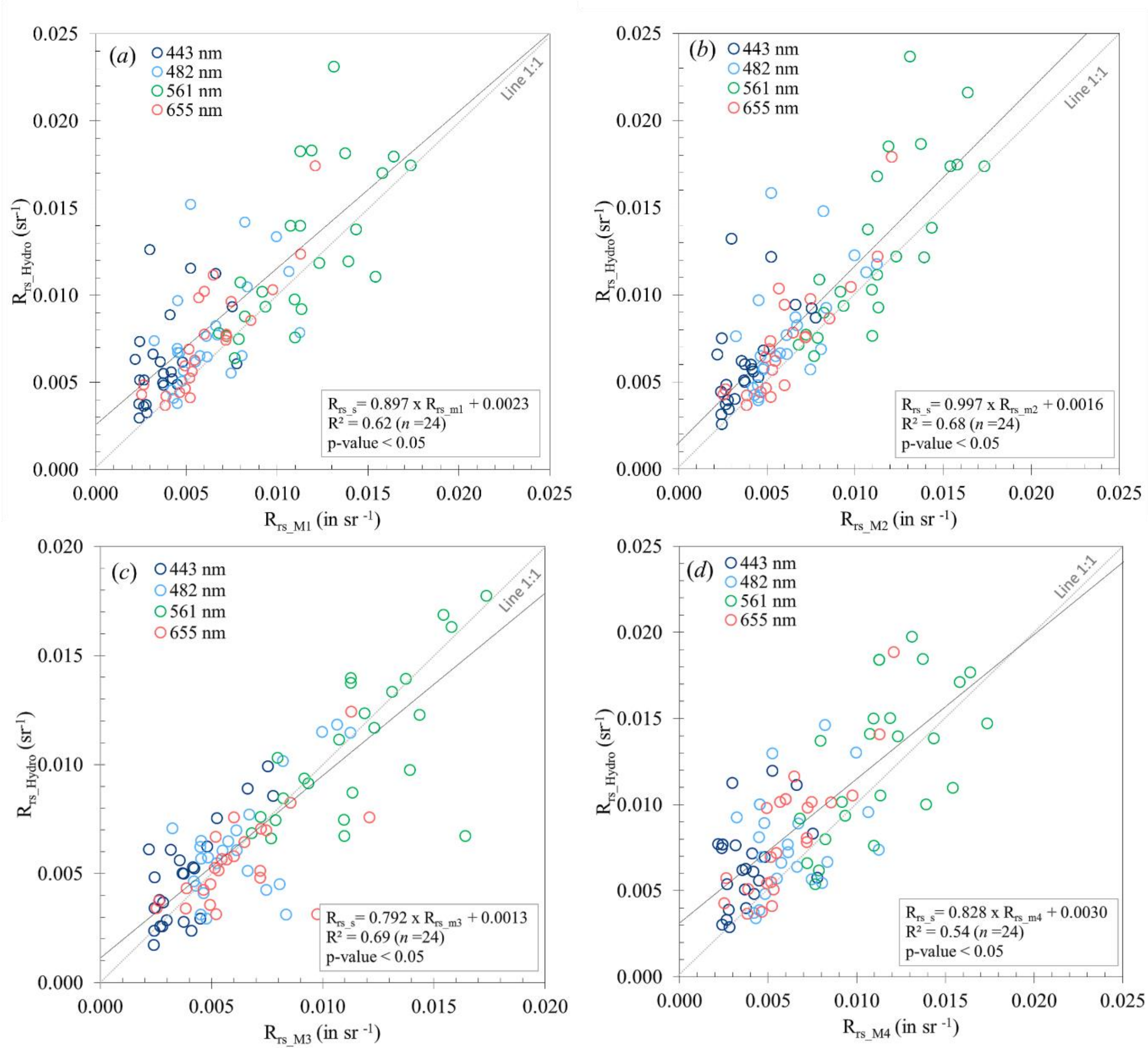

Overall, the nRMSD ranged from 7.6% to 54.1% over the entire TRCS's dataset. Excepting BB1 and IBI1, the M3 approach retrieved the lowest errors (Table 4.4). It is important to highlight that IBI2 showed a meaningful variation of errors comparing all corrections, ranging from 16.6% to 40.2%. Meaningful differences between glint removal methods were also found in BB2—the errors comprising between 18.8% and 54.1%, reducing the error by about 35%. Regarding all glint removal methods tested in this work, the most suitable R_{rs} dataset was provided by M3, it means, the spectral ρ correction (Lee et al., 2010).

Table 4.4 nRMSDs (%) for in situ R_{rs} retrieved from M1, M2, M3 and M4 methods using HydroLight R_{rs} as reference data.

Fieldworks	M1 (Mobley 1999)	M2 (Mobley 2015)	M3 (Lee et al., 2010)	M4 (Ruddick et al., 2006)
BB1	12.4	12.8	18.4	24.5
BB2	41.1	34.6	18.9	54.1
BAR1	34.9	37.0	24.8	28.5
BAR2	20.4	22.0	19.5	32.1
IBI1	8.0	7.6	16.5	15.4
IBI2	26.8	16.6	20.8	40.2
NAV1	28.1	31.7	10.5	30.7
NAV2	31.5	17.1	11.7	32.7

Besides the analysis for each fieldwork, we evaluated the errors based on OLI central wavebands (Table 4.5). Therefore, glint-removed R_{rs} and Hydrolight R_{rs} were spectrally convoluted (Equation 4.12) and comparisons were made by wavelength. Relying on the results, the lowest errors retrieved from M3 approach again (20.34–29.8% of nRMSD and 13.9–39.3% of MAPE), whereas the highest errors retrieved from M4 approach (30.1–64.2% of nRMSD and 26.2–86.6% of MAPE). Regarding the wavelengths, the highest errors were found in 443 nm, whereas the lowest errors were found in 665 nm.

Table 4.5 Error assessment (nRMSD) from comparisons between in situ R_{rs} (retrieved from glint removal corrections—M1, M2, M3, M4) and simulated R_{rs}. Error analysis from simulated R_{rs} and M1, M2, M3, and M4 comparisons for the entire spectrum.

OLI Bands	M1	M2	M3	M4	M1	M2	M3	M4
	nRMSD (%)				MAPE (%)			
443 nm	59.76	57.42	**29.81**	64.24	74.05	68.02	**39.26**	86.56
482 nm	39.02	38.43	**24.50**	42.56	38.63	35.08	**25.53**	48.19
561 nm	32.48	32.43	**25.79**	34.14	20.87	19.30	**13.91**	26.15
655 nm	22.18	20.79	**20.34**	30.09	25.60	24.71	**18.46**	38.91

4.3.3 OLI R_{rs} *versus* Glint removal R_{rs_M3}

Plots of matching pairs between the LaRSC product of OLI bands and the in situ R_{rs} retrieved from the M3 glint removal method are shown in Figure 4.5. For such an analysis, we used solely the sampling spots (n = 34) that matched with the Landsat-8 overpass in order to minimize the temporal effects over the results. It is important to highlight that if the image for NAV1 presented an overcast sky, then, this fieldwork was not considered in our analysis due to the sample spots in the same day of data acquisition are under cloud coverage.

Figure 4.5 Comparison between OLI derived and in situ R_{rs} at 34 sampling spots.

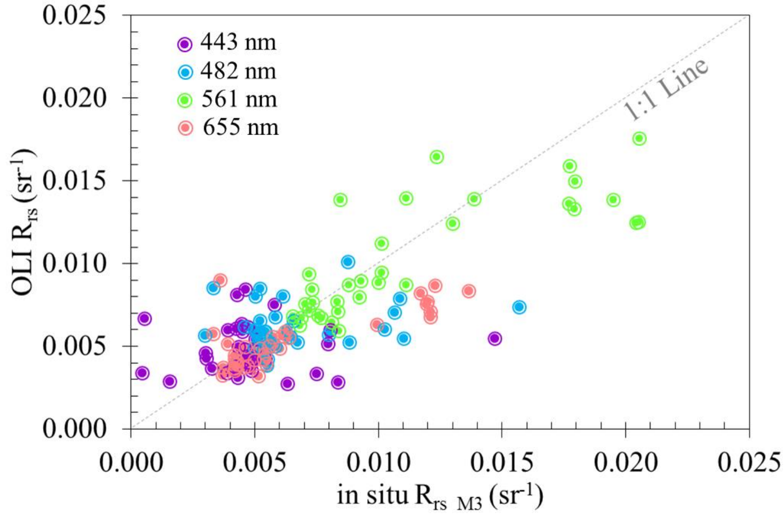

The OLI3 (561 nm) and OLI4 (655 nm) plotted in Figure 4.5 are well distributed along the 1:1 line and showed r = 0.60 (p-value < 0.05). OLI1 and OLI2 did not show relevant correlation coefficients (r = 0.002 and 0.05, respectively), which implied higher MAPE in OLI1 and OLI2, 43.6% and 29.6% when compared to OLI3 and OLI4–MAPE of 18.4% and 28%, respectively

4.4 DISCUSSION

Computing suitable R_{rs} spectra is not an easy task. The glint removal methods are widely used in a broader range of oceanic and freshwater systems; however, there is no consensus of which method is the optimum way to provide accurate datasets (Lee et al., 2010). The TRCS presented a wide range of water quality parameters, from turbid to clearer waters (turbidity ranged from 1.01–80.9 NTU), with algae blooms, and scums. In some cases there is a CDOM dominance in some reservoirs with brown color, which was observed during in situ measurements (BAR2 and IBI2).

Water quality parameter variations from up-to-downstream inside a unique continuum system (Tietê River) are dependent on the time residence of the water, inputs from tributaries along the cascading reservoirs, auto-depuration, the availability of solar irradiation, and the activities developed within the sub-basin areas that contribute to wastewater discharges. Barra Bonita, for instance, is near to São Paulo (capital of São Paulo State) and it is the most populous city in Brazil (Watanabe et al., 2016). The Bariri reservoir receives discharge from the river that flows throughout Bauru city, an urban area that recently adopted wastewater treatments, and Ibitinga is near Environmental Protection Areas, which contribute to the organic matter as a result of the vegetation coverage (Cairo et al., 2017). Besides, the continuum river cascade concept (CRCC) in TRCS contributes to meaningful changes throughout a sequence of impoundments within the same river–retention of particles as turbidity decreases and a higher amount of energy along the water column in downstream accumulates (Barbosa et al., 1999).

Several water types can be found in TRCS identified by ternary diagrams (Figure 4.2). With absorptions displaced towards the CDOM axes in BAR and IBI, BB showed absorption coefficients displaced towards the phytoplankton axes, and NAV presented absorption coefficients well distributed inside the ternary diagram with slightly higher contributions of NAP (Barrela et al., 2003). The iron absorption features (450–550 nm) and high CDOM absorption coefficients (<500 nm) resulted in flat *Rrs* spectra at shorter wavelengths (<550 nm), mainly in curves obtained in BAR, IBI, and NAV fieldworks (Brezonik et al., 2015; Xiao et al., 2015; Kutser et al., 2016). In case of black waters, CDOM absorption can be higher than water absorption even at 700 nm (Kutser et al., 2016). The increase in magnitudes at 550 nm is related to several SPM concentrations and compositions, with inorganic particles causing light scattering in the green spectral region (Han et al, 1997; Doxaran et al., 2002). A minor reflectance feature near 760 nm, in almost all spectral curves, can be associated to oxygen absorption (Kutser et al., 2013) and normally related to the glint effect. Computing the dip of oxygen absorption, the results from all approaches were close to zero ($D \leq 0.001$), which means the glint effect was removed (Kutser et al., 2009).

After applying the glint correction methods, the features in the R_{rs} spectra only changed in magnitude. The main differences between glint removal methods are presented in Table 4.1. The adoption of specific geometry views aimed to rule out problems with sun glint, shadows, reflections, foam, and whitecaps (Mobley 1999). During in situ measurements, we adopted the sensor's viewing of 40° from nadir and from zenith to measure L_t and L_{sky} as recommended by Mobley (1999), nevertheless, the wind speed overcame 5 m.s^{-1} in BAR, IBI and NAV fieldworks, which makes the adoption of ρ = 0.028 unfeasible. Besides, the effects on several viewing geometry sets under radiometric measurements are described in

(Garaba et al., 2013). The wind speed variations caused roughened surfaces, where each wave facet caused the solar light to be reflected into the sensor's viewing and resulted in different L_{sky} contributions (Zhang et al., 2017). Facing such a challenge, the surface radiance needs to be modeled and removed from R_{rs} by using the sea-surface reflectance factor—ρ. Then, ρ models the glint effects caused by the waves reflection of radiance. When better ρ is estimated, more accurate is R_{rs} computations are achieved (Lee et al., 2010).

Accurate estimates of ρ values depend on the sky conditions, sea state, viewing geometry, and environmental conditions. In order to control the variable geometry viewings, our sensors were coupled on steel frames positioned in boat platforms, so the instability of the boat caused by waves was taken into account by the measurements that were not commonly taken in a perfect viewing geometry. Apart from geometry, some measurements were taken under unstable conditions beyond human control, such as the variability of environmental conditions (wind speed, cloud coverage variations, and atmospheric composition with particles due to sugarcane burned areas near reservoirs - Gomes et al., 2017).

The glint removal results demonstrated similar patterns between the M1 and M2 approaches for almost all reservoirs (NAV2 was the exception), with a very similar coefficient of variation of R_{rs} (Figure 4.3). A previous study developed by Garaba et al. (2015) indicates that some glint removal methods are overlapped, resulting in similar corrections due to the same optical assumptions. 68% of ρ values from M2 were comprised between 0.025 and 0.028, which demonstrated a relative overlap of ρ values with M1, and consequently, very similar results (Garaba et al., 2015). The remainder values of M2 were equally divided into two main categories: 0.020–0.025; and 0.028–0.037. The highest value of ρ was also accomplished with wind speed near 5 $m \cdot s^{-1}$.

M4 did not show similar results from M1, M2, and M3 approaches in environments where inorganic loads are an expressive component of SPM (around 40% on average). This conclusion can be obtained by observing IBI1 and NAV2 (Figure 4.3 - e,h) fieldworks, which can indicate that M4 showed different behavior when applied to environments with marked inorganic composition, although they were developed for specific turbid areas.

CDOM-rich environments (BAR2, IBI1 and IBI2) did not present wide variations in the R_{rs} visible range (400–700 nm), on the contrary, the NIR range showed a higher variation as depicted in Figure 4.3 (CV of M4 in BAR2 ranged from 40% to 80%). Considering BAR1 as a CDOM environment with remarkable phytoplankton concentrations, the results did not follow the same pattern as BAR2, IBI1, or IBI2. BAR1 presented variability very similar to the BB1 and BB2, which were fieldworks with high SPM concentrations and high levels of Chl-*a*, with samples reaching more than 250 $mg \cdot L^{-1}$. The M3 approach depicted the most distinguishable CVs among all of the tested approaches. The variations in M3 results can be a consequence from the Δ corrections that took into account, as an initial guest, the average of R_{rs} between 750–800 nm (in some cases, considering even longer wavelengths for such computation). This spectral region was influenced by a marked peak at 760 nm in some R_{rs} spectra, then, the initial guess of Δ can be highly variable, resulting in widely spectral optimizations.

Facing the challenges of glint removal, we simulated 24 spectra from all fieldworks using HydroLight to obtain a reference dataset. Then, we spectrally resampled the in situ and HydroLight R_{rs} to compute the errors. Error assessments of each fieldwork retrieved MAPE ranging from 7.6% to 54.1%, with M4 retrieving the highest errors. The errors from M4 can be caused by the wind speed equation based on optical simulations (Equation 4.8) that probably did not correctly estimate the spectral-reflectance proportional factor and did not retrieve the most accurate R_{rs} datasets.

We relied on the errors assessment demonstrated in Table 4.4. Almost all glint-removed methods did not work for CDOM-rich environments, such as IBI1 and IBI2, where the errors achieved were higher than 20%. The most suitable glint removal method was M2 (with errors around 8% and 17%) for IBI1 and IBI2. Regarding the M3 results for IBI2, we improved from 20.8% in M3 to 11% when we did not take into account the sampling with lowest Chl-*a* and SPM concentrations. This result indicates that the M3 approach is highly sensible for measurements carried out in environments with remarkable CDOM amounts and less expressive Chl-*a*/SPM concentrations.

Modeling glint effects from higher Chl-*a* concentrations, and consequently high SPM concentrations, was also a challenge. Removing the samples with the highest concentrations for BB1 and IBI1, the MAPE changes from 18.4% to 11.5%, and 16.5% to 9.0%, respectively, suggesting that M3 is a good approach overall the methods, however, it was very sensible when the dataset contained a few concentrations of outliers. Overall, the M3 approach showed the best results in BB2, BAR (both fields), and NAV (both fields). Considering that M3 approach corrects the sun and sky glint effects, and also takes into account the spectral variation of ρ (in our case, the values varied in a factor of 8 such as the results showed in Lee et al. (2010)), the best results were expected from the glint removal method. Overall, the M3 approach was the most suitable method for glint correction in high turbid waters, as found in BAR and BB, and clearest waters, as found in NAV.

Considering several studies about bio-optical modeling for inland waters (Li et al., 2013; Watanabe et al., 2016) and the potential of OLI for its aquatic monitoring (Pahlevan et al., 2014; Bernardo et al., 2016) we evaluated the matching between our glint corrected R_{rs} and LaSRC from OLI. The OLI dataset has been widely applied to inland water systems due to its spatial resolution and the detailed richness of such environments (Vanhellemont and Ruddick. 2014; Alcântara et al., 2017; Bernardo et al., 2017; Lee et al., 2017).

In the relied error analysis (Table 4.5), it was observed that the coastal band retrieved errors near 43% of nRMSD (and 54% of MAPE), which can be related to atmospheric issues, such as high influence of Rayleigh scattering and aerosol concentrations (Vanhellemont and Ruddick, 2014). Besides, the green and red band retrieved lower errors (nRMSD < 26%) even with some sampling spots displaced towards higher values ($R_{rs\_M3} > 0.020$ sr^{-1}) for the green region (Figure 4.4). These points related to high levels of Chl-*a* concentrations (> 250 mg·L^{-1}). No wind and haze days meant the sky was partly clouded and this increased L_{sky}, making the glint correction more challenging, which probably caused the mismatching.

OLI errors from Table 4.5 indicate the suitability of OLI bands in the green and red bands, however, the short wavelengths represented by the Coastal (443 nm) and Blue (482 nm) bands showed significant errors. In 443 nm, the MAPE was higher than the other wavelengths, which can be caused by two main problems: atmospheric issues in the blue range or high Chl-*a* concentrations that are additional to the higher CDOM absorptions. A deep decrease in the R_{rs} in this range complicates atmospheric correction. It is worth mentioning that the spectral mixture and spatial resolution impacts the acquisition of images, and in situ measurements were not evaluated in this paper, yet they have implications for matching. Based on our results, and considering the OLI applications for inland environments, it will be possible to use OLI green and red bands for monitoring SPM. For instance, for CDOM estimates (Kutser et al., 2005), if 443 nm is used for CDOM absorptions

(Matthews 2011, Zhu et al., 2014), it might be necessary to achieve better evaluations of the atmospheric correction methods, as well as, the impacts of glint-removal.

4.5 CONCLUSIONS

Computing reliable R_{rs} datasets is crucial to obtaining accurate estimates, describing optical features, developing bio-optical modeling, and establishing environmental monitoring by satellite products. The main challenges for in situ measurements are to reduce the glint effects from the sky and sun light into the water-leaving radiance, or R_{rs}. Besides, other aspects such as viewing and illumination geometry, environmental conditions (wind speed, clouds, solar incident radiation), and vertical mixing of water components produced uncertainties in R_{rs}.

The present study evaluates four methods of glint removal and identified that the spectral method (aforementioned as M3) (Lee et al., 2010) provided the most accurate data when compared to synthetic datasets obtained from HydroLight simulations. The main advantage of computing the spectral glint correction is considered to be the spectral influence of the surface reflectance into the remote sensing signal. In addition, using a delta to remove glint residuals fits very well for almost all optical compositions evaluated in this paper. One exception needs to be highlighted: the spectral approach is too sensible when the dataset contains some outliers of Chl-*a* concentration. Our results also support that CDOM-rich environments are a challenging task, since the best glint removal for this case was variable ρ, which was different from all other fieldworks

Our results pointed out that there is no general value of ρ factor to be adopted in different inland water conditions. On the contrary, the findings demonstrated that the most suitable methodology is the spectral ρ. That in turn means, for very unstable platforms (boats) and inland water environments (optical complex systems), non-flat surfaces considerably affect the sensor's measurements, and at some moment, the sensor is registering the sun glint effect, which needs to be spectrally corrected. All other tested methods provided less accurate R_{rs} datasets.

Comparisons to the LaSRC product demonstrated the same trend: M3 is the best approach to provide R_{rs} for spectral matching and the quality control of the optical information. Coastal and blue bands (centered at 442 nm and 481 nm) showed the highest errors. The error sources can be attributed to the high levels of CDOM and Chl-*a* concentrations that increase the absorptions in this spectral region and make the atmospheric correction a challenge. Other reasons for mismatching in lower wavelengths are related to Rayleigh scattering from atmospheric components, or adjacency effects (spectral mixture contamination), which are beyond the scope of our study. Special attention has been given to CDOM-rich environments, since the glint removal methods were sensitive to this optical composition. Regarding the other optical compositions (NAP or Chl-*a* dominance), the spectral glint correction when compared to the other glint-removal methods, retrieved suitable R_{rs} and reduced the errors by almost 30%.

CHAPTER 5: EMPIRICALLY TUNED MODEL TO ESTIMATE THE SUSPENDED PARTICULATE MATTER IN A RESERVOIR CASCADING SYSTEM

5.1 SCOPE

Remote sensing techniques are capable to establish the water quality conditions using bio-optical modeling. The term bio-optical was used by Gordon et al. (1975) and denotes the state of water in terms of optical properties, meaning, the mechanisms of absorption and scattering of light along the water column with optical active components (OACs), that are summarized by phytoplankton (represented by Chl-a pigment), suspended particulate matter (SPM) and colored dissolved organic matter (CDOM), besides the water itself. The SPM is the most important component because it affects the water clarity, implying in high levels of light attenuation, affecting the primary production of inland water systems (Doxaran et al., 2002; Song et al., 2012, Lee et al., 2016).

Empirical approaches are an easy way to estimate SPM concentrations using remotely sensed data, which are divided in two sub-categories – empirical or semi-empirical (Morel, 2001; Lee et al., 2002). The basic difference is related to the development steps. Empirical models are based on statistics correlation and cannot assume physical meaning. Semi-empirical models are established based on the physical background and consider the spectral behavior of water targets (Ogashawara, 2015). Regarding the statistical correlations, it is expected that band ratios retrieved better results than single band models because the band ratios minimize the external effects, such as the undesirable light variability, atmospheric effects or even the effect of heterogeneity of shape and physical properties of sediments (Kong et al., 2018). Besides the aforementioned advantages, the best of empirical models is the quick application and simplicity; however, it is still a challenge to identify which are the most suitable single band or band ratio to estimate the SPM concentrations over a widely ranging of SPM concentrations.

Several studies have been conducted in order to map SPM concentrations, collecting SPM samples to calibrate and validate models (Matthews 2011, Odermatt et al., 2012, Kutser et al., 2016). The use of derivative analysis (Chen et al., 1992; Han et al., 1994) contributes to minimize the influences of Chl-a over the SPM. Other approaches are based on single or band ratio index (Doxaran et al., 2002b, Rodrigues et al., 2017b) to empirically estimate SPM ranges. In the literature, other relevant premises to provide a well-performed model are the robustness of dataset, the choose of the most suitable spectral interval, the fit type (linear or polynomial), the saturation of remote sensed signal at certain SPM levels (Luo et al., 2018), and the effects of OACs into the accuracy of SPM estimates (Nechad et al., 2010).

Over a widely range of SPM concentrations, it is a challenge to provide a single remote sensing algorithm that shown a statistically significant performance. Facing the site-specific dependence of empirical modeling (Ogashawara et al., 2016) and considering the complexity of inland waters (Odermatt et al., 2012), it is required a tuning approach to provide the most reliable estimates by the empirical modeling approach. The objective of the present work was to investigate the relationships between the heterogeneous SPM configuration in Tietê River Cascade System (TRCS) and the remote sensing reflectance (R_{rs}), by identifying the existence the most suitable empirical model to quantify a widely interval of SPM concentrations.

5.2 MATERIALS AND METHODS

5.2.1 TRCS Dataset

The dataset used in this work contains 174 samplings of in situ measurements of SPM concentrations and R_{rs}. R_{rs} dataset were computed as described in Chapter 4, using the methodology described in Lee et al. (2010). The radiometric measurements were gathered out in four reservoirs along the TRCS (See chapter 2 for Study area), and two fields were conducted in each reservoir. The measurements of radiance and irradiance were gathered out using TriOS radiometers, registering the signal from 350 to 900 nm, at 3.3 nm of spectral resolution, using the geometry set proposed in Mobley (1999).

A linear interpolation was conducted for the entire dataset in order to achieve the 1-nm resolution. The Hyperspectral R_{rs} were resampled to match with the Operational Land Imager (OLI) bands using the spectral response function of each band (Barsi et al., 2014). The sensor OLI/Landsat-8 have been provide interesting results in the inland water monitoring field (Bernardo et al., 2016). The SPM concentrations were established in laboratory using APHA (1998) protocol and water samples collected in situ during the field campaigns. Water quality parameters were also measured and are described in Table 2.1.

5.2.2 SPM Modeling

Empirical models were established using the hyperspectral and spectral resampling dataset for Operational Land Imager, Landsat-8, with linear and polynomial fitting. We divided our investigations into three groups (Figure 2): (i) the dataset from one field was used to calibrate the model, and the validation was made using the remainder TRCS' dataset (resulting in 8 models). (ii) Two campaigns from a unique reservoir was used to the models, and the validation was made using the remainder TRCS' dataset (resulting in 4 models). The fitting models were evaluated using Pearson correlation's coefficient (Equation 1) or R^2 (= r^2).

$$r = \sum_{i=1}^{N}\left[\frac{x_{m,i}-\left(\frac{1}{N}\sum_{j=1}^{N}x_{e,j}\right)}{\left(\frac{1}{N-1}\sum_{k=1}^{N}\left[x_{m,k}-\left(\frac{1}{N}\sum_{l=1}^{N}x_{m,l}\right)\right]^2\right)^{0.5}}\right]\left[\frac{x_{e,i}-\left(\frac{1}{N}\sum_{j=1}^{N}x_{e,j}\right)}{\left(\frac{1}{N-1}\sum_{k=1}^{N}\left[x_{e,k}-\left(\frac{1}{N}\sum_{l=1}^{N}x_{e,l}\right)\right]^2\right)^{0.5}}\right] \quad (5.1)$$

In the investigation (iii), three sub-groups were tested: (a) the entire dataset was randomly divided into a calibration (70%) and validation (30%) dataset, whereas the fitting was provided by SOLVER tool available at Microsoft Excel®; (b) the dataset was iteratively divided in order to select an optimal dataset division to calibrate and validate the model. The stop criteria was the lowest retrieved error. Besides the in-situ validation, we also applied the retrieved models to OLI images. It is important to highlight the differences between approaches (a) and (b) - the approach (a) optimized the fit whereas the approach (b) optimized the TRCS division dataset for calibration and validation.

Approach (c) established a single model using the entire TRCS dataset, and we validated the model only using the OLI image, it means, the SPM estimates retrieved from this model that was applied into the satellite image. The only validation was only provided using the OLI images. The SPM retrievals models from approach (a) and (b) were also validate with the OLI images (besides the use of in situ dataset for validation) (Figure 5.1).

Figure 5.1 Schemes to calibrate and validate the models. Note that approach c was only validated using the OLI image results.

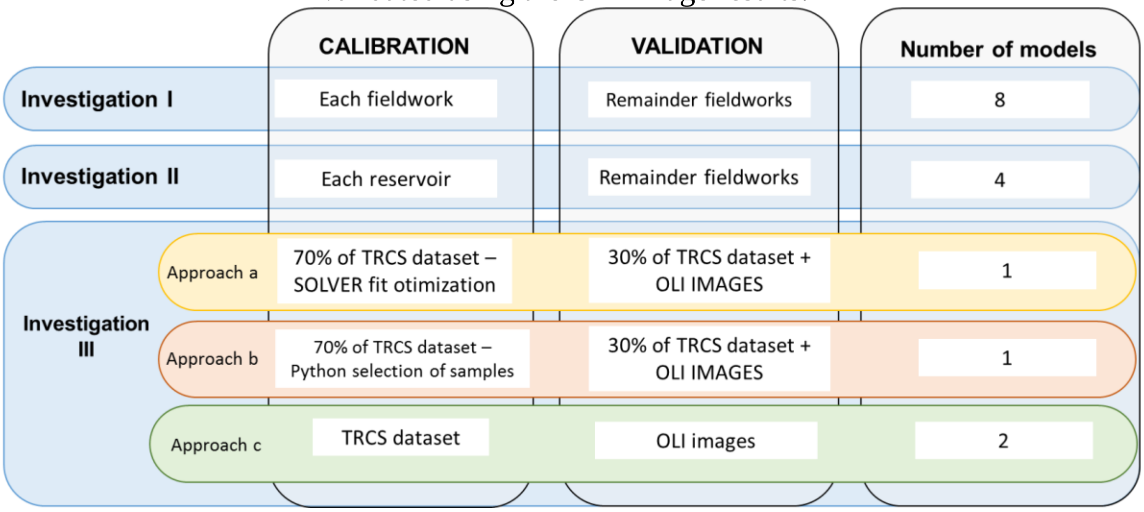

The accuracy assessment was made by computing the errors (Equation 5.2 to 5.4).

$$RMSE = \sqrt{\frac{1}{n}\sum_{i=1}^{n}(x_{e,i} - x_{m,i})^2} \tag{5.2}$$

$$nRMSE = \frac{RMSE}{(\max(x_{m,i}) - \min(x_{m,i}))} \times 100 \tag{5.3}$$

$$MAPE = \frac{1}{n}\sum_{i=1}^{n}\frac{|x_{e,i} - x_{m,i}|}{x_{m,i}} \times 100 \tag{5.4}$$

5.2.3 SPM Retrieval from OLI/LANDSAT-8

SPM retrieval models that presented best performances were applied to the Landsat Surface Reflectance Code (LASRc, Zanter 2018). OLI images were converted into R_{rs} by multiplying the bands by a scale factor (10^{-4}) and dividing them by π. Then, the models were applied to the image to map SPM via OLI images (see Table 5.1 for OLI images used in this study).

Table 5.1 OLI images used to SPM mapping.

Acquisition Date	Fieldwork	Path/Row
13 Oct 2014	BB2	220/076
15 Aug 2016	BAR1	220/076
21 June 2016	IBI1	221/075
05 May 2014	NAV1	222/075

5.3 RESULTS

5.3.1 Water Characterization

Statistical of water quality parameters are described in Table 5.2. The results are described for each field, each reservoir, and the entire dataset. Upstream reservoirs, such as BB and BAR, presented high levels of SPM and Chl-*a*, consequently, high turbidity and lower values of Z_{SD}. Meanwhile the downstream reservoirs, such as IBI and NAV presented high Z_{SD} and lower Chl-*a* and SPM concentrations. The entire cascade of reservoirs, presented by TRCS, shown a widely range of SPM (0.2 – 44 $mg.L^{-1}$) and Chl-a concentrations (1.37 – 797.8 $mg.m^{-3}$), imposing a challenge to estimate SPM over the widely optical conditions encountered along the cascade.

Table 5.2 Statistics for water quality parameters. The symbols are BB – Barra Bonita, BAR – Bariri, IBI – Ibitinga, NAV – Nova Avanhandava, TRCS – Tietê Reservoir Cascade System. The Z_{SD} is the Secchi Disk Depth.

		Z_{SD} (m)	Turbidity (NTU)	Chl-*a* ($mg.m^{-3}$)	SPM ($mg.L^{-1}$)
BB1	Min-Max	0.80 - 2.30	1.66 - 12.9	17.8 - 279.9	3.6 - 16.3
	Mean±SD	1.49 ± 0.43	5.17 ± 2.43	120.44 ± 70.3	7.21 ± 3.3
BB2	Min-Max	0.37 - 0.78	11.6 - 33.2	263.2 - 797.8	10.8 - 44.0
	Mean±SD	0.57 ± 0.10	18.6 ± 5.27	428.7 ± 154.5	21.9 ± 7.04
BAR1	Min-Max	0.50 - 1.60	7.80 - 80.9	25.7 - 709.9	3.6 - 40.3
	Mean±SD	1.16±0.29	16.6±13.9	119.8±159.9	8.30±8.44
BAR2	Min-Max	1.60 - 2.50	3.48 - 8.80	3. 82 - 19.1	0.2 - 2.6
	Mean±SD	2.06 ± 0.24	5.72 ± 1.60	7.99 ± 4.10	1.59 ± 0.6
IBI1	Min-Max	1.60 - 3.20	2.82 - 8.87	1.37 - 119.04	1.00 - 8.10
	Mean±SD	2.23 ± 0.35	4.29 ± 1.20	21.75 ± 28.4	2.61 ± 1.6
IBI2	Min-Max	1.90 - 3.80	1.85 - 3.60	2.46 - 13.65	0.2 - 2.20
	Mean±SD	2.93 ± 0.57	2.47 ± 0.52	7.08 ± 4.24	1.06 ± 0.60
NAV1	Min-Max	2.29 - 4.80	1.01 - 2.47	15.30 - 20.0	2.46 - 12.56
	Mean±SD	3.15 ±0.65	1.66 ± 0.43	6.2 ± 2.55	1.01 ± 0.60
NAV2	Min-Max	2.45 - 4.65	1.01 - 2.56	6.40 - 10.30	0.50 - 2.80
	Mean±SD	3.41 ± 0.62	1.73 ± 0.41	7.87 ± 0.98	1.00 ± 0.58
TRCS	Min-Max	0.37 - 4.80	1.01 - 80.9	1.37 - 797.8	0.20 - 44.00
	Mean±SD	1.15 ± 1.02	13.31 ± 8.90	197.5 ± 157.9	11.3 ± 7.91

Additionally, scatterplots were depicted in Figure 5.2 to provide the relationships between water quality parameters. Z_{SD} parameter is well distributed along its entire range.

The higher frequency of Chl-*a* concentration is lower than 200 mg.m^{-3}, whereas the SPM concentration presented higher frequencies of SPM < 25 mg.L^{-1}. Turbidity values are more represented between 0 – 20 NTU interval, with few samples that presented values higher than 40 NTU.

Figure 5.2 Scatterplots of water quality parameters with marginal plots of histograms of frequency from each variable considering the entire dataset.

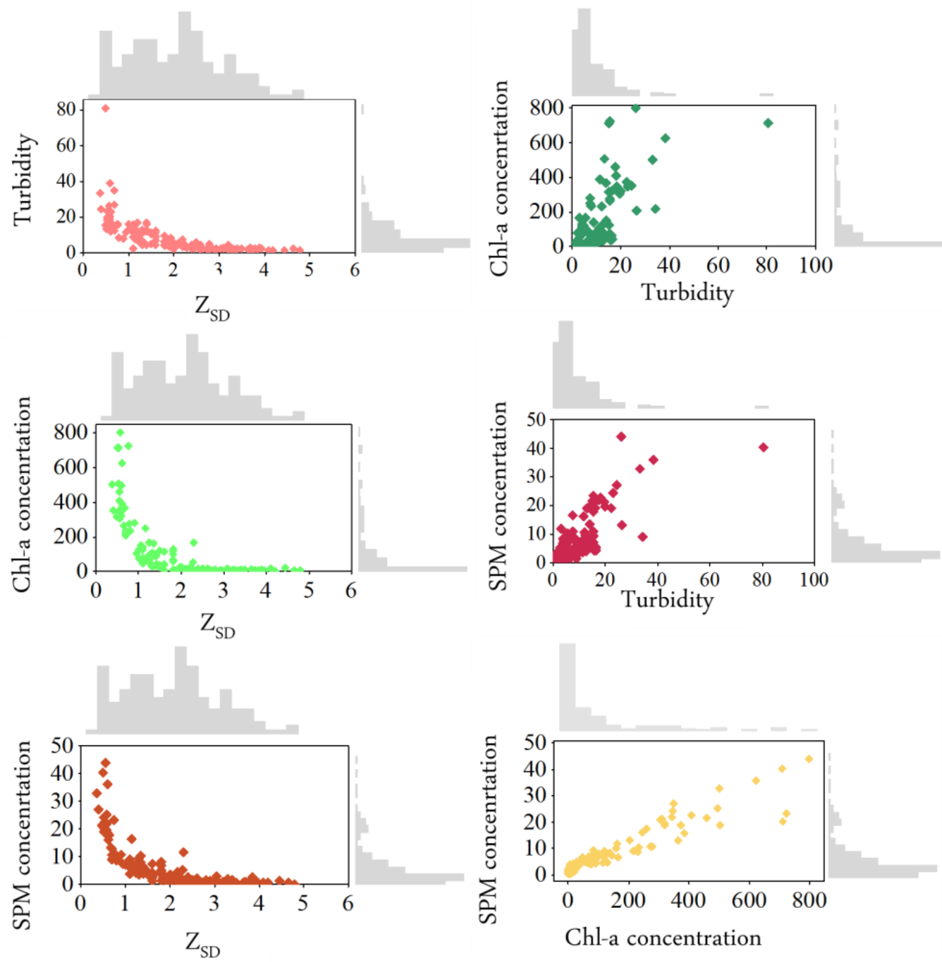

The R_{rs} datasets (hyperspectral and resampled) are depicted at Figure 5.3. Different magnitudes and shapes in R_{rs} spectra are found in TRCS. Overall, a variable magnitude of 550 nm-peak in hyperspectral measurements indicate the variability in SPM concentrations and respectively backscattering differences. Some curves shown this peak displaced towards to longer wavelengths, which reveals CDOM absorption contributions. A peak in the near infrared (around 700 nm) also is a response of SPM backscattering in highly turbid waters (Doxaran et al., 2002). Other relevant features in hyperspectral dataset is the presence of deeply phytoplankton absorption near 680 nm, which can be justified by the high levels of Chl-*a*.

Figure 5.3 (a) in situ Hyperspectral and (b) Resampled R_{rs} dataset for OLI/Landsat-8.

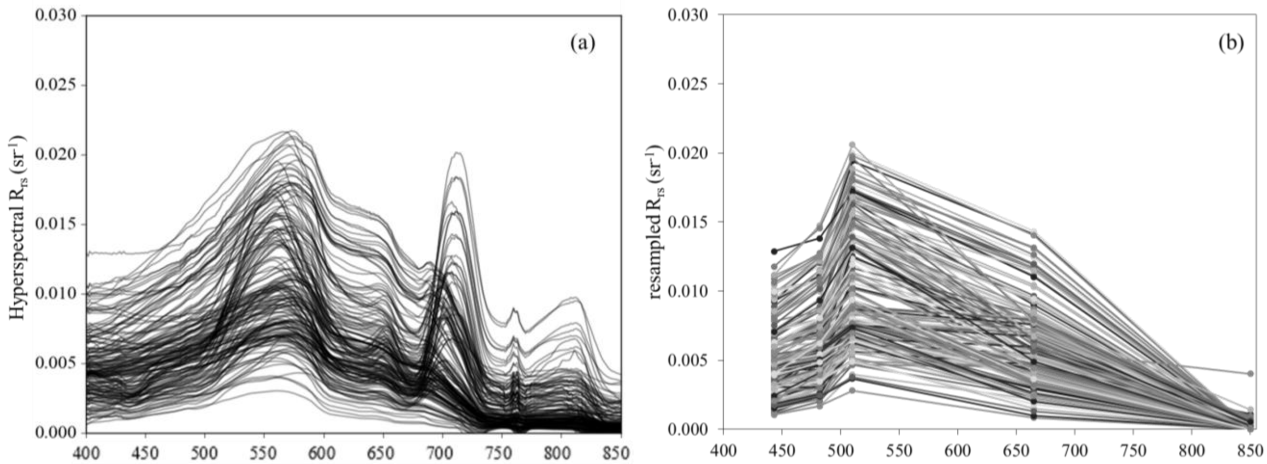

5.3.2 Correlation Analysis

Due to the high contribution of organic matter into the SPM composition, the correlation analysis for hyperspectral measurements were conducted for SPM and Chl-*a* concentrations. The plots are shown in Figure S.5.1, and significant correlations (even when negative) are shown in Table 5.3.

Table 5.3 Correlation coefficients(r) for hyperspectral (λ) and resampled R_{rs} (OLI bands). For acronyms see Table 2.1.

Field	λ (*r*) SPM	λ (*r*) Chl-*a*	OLI band (*r*) SPM	OLI band(*r*) Chl-*a*
BB1	707 (0.65)	707 (0.62)	561 (0.64)	561/482 (-0.30)
BB2	760 (0.57)	678 (-0.60)	655 (0.44)	561 (-0.37)
BAR1	436 (-0.44)	436 (-0.57)	561/482 (0.37)	561/482 (0.47)
BAR2	680 (0.31)	580 (-0.49)	561/655 (0.26)	561 (-0.47)
IBI1	583 (0.58)	719 (0.68)	561 (0.55)	561/482 (0.64)
IBI2	576 (0.28)	697 (0.40)	561/482 (0.18)	561/482 (0.31)
NAV1	780 (0.62)	710 (0.41)	561/482 (0.45)	561/482 (0.27)
NAV2	500 (0.25)	775 (0.25)	561 (0.24)	561/482 (0.23)
TRCS	720(0.80)	720(0.74)	561/482 (0.65)	561/482 (0.66)

Considering the SPM correlation, hyperspectral R_{rs} retrieved better correlation coefficients than the OLI resampled R_{rs}. The NIR interval (700 to 800 nm) retrieved r > 0.60, whereas the green interval (500 to 600) did not presented the correlation coefficients higher than 0.60. Overall, SPM retrieved higher correlation than Chl-*a* considering the entire dataset (0.80 against 0.74 in 720 nm). Some of correlation is lost when we looked at OLI spectral bands, that returned r = 0.65 using a band ratio of green and blue band, and the results of SPM and Chl-*a* are comparable (0.65 of SPM against 0.66 of Chl-*a*).

It is important to note that blue to green ratio showed the highest correlation in BAR1, IBI2 and NAV1, which were campaigns with relatively contribution of CDOM absorptions, and the 482 nm band can be used to minimize such effects (Ogashawara et al., 2016). In general, the higher correlation coefficient between SPM and OLI R_{rs} occurred in the green (located at 561 nm).

5.3.3 Empirical Algorithms for SPM Retrieval

The SPM equations established from each fieldwork (investigation I) are shown in Figure S.5.2. All results from investigation (i) (linear regressions between OLI R_{rs} and SPM concentrations) retrieved worst R^2 values than the band ratios used to provide the models in investigation (iii), excepting in BAR1 where R^2 = 0.56 at 655 nm. Investigation (ii), that considered two datasets to calibrate the SPM models, did not present significant improvements when compared to the method (i). Therefore, the models resulting from investigation (ii) were not included in this paper.

Considering the investigation (iii), the errors of SPM estimates derived from approach "a" (with Solver optimization fitting) and approach "b" (with Python optimization chose of samples) are shown in Table 5.4. It is important to highlight that investigation iii retrieved models from approaches "a" and "b" that are statistically equal (Figure 5.4).

Table 5.4 Errors analysis from investigation (iii) - approaches "a" from Solver and "b" from Python.

	Approach "a"								
	562 nm			**665 nm**			**865 nm**		
	ax+b	ax²+bx+c	$ae^{b\times x}$	ax+b	ax²+bx+c	$ae^{b\times x}$	ax+b	ax²+bx+c	$ae^{b\times x}$
Bias	0.35	0.75	-3.09	0.61	44.29	-3.28	0.87	0.51	-3.39
RMSE	8.58	8.18	9.19	8.57	79.47	9.39	8.22	7.86	9.02
nRMSE	23.97	**22.85**	25.66	23.94	221.99	26.22	22.97	21.95	25.21
	Approach "b"								
Bias	0.23	-	-	0.98	-	-	0.94	-	-
RMSE	2.68	-	-	3.57	-	-	3.47	-	-
nRMSE	**17.32**	-	-	18.37	-	-	18.51	-	-

The fitting from approach a (R^2) were very low for all adjustments (Figure 5). The best result was achieved at green OLI band (562 nm) where we obtained $R^2 = 0.22$ (p-value = 0.05) using the quadratic fitting.

Figure 5.4 Fitting models from Approach "a" at (a) 562 nm; (b) 655 nm; and (c) 865 nm. Approach "b" were not shown (optimization process retrieved only numerical results)

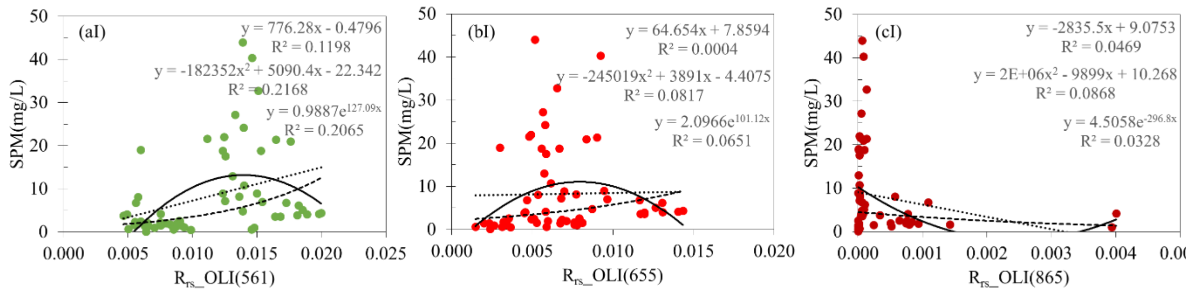

The SPM retrieval models retrieved from approach "c" are shown in Figure 5.5. Among all possible band rations, two band ratios retrieved the best results and were tested: the simple band ratio (model I) and the other model which includes the band of coastal range (443 nm – model II) in order to reduce the atmospheric effects into the index (Figure 5.5 – b). Considering that R^2 was higher than the value retrieved from investigations (i), (ii), and (iii – Approaches "a" and "b"), the models from investigation iii – Approach "c" was also applied to the OLI images considering the model shown in Figure 5.5.

Figure 5.5 SPM algorithm tuning in each field campaign with (a)simple band ratio (R^2 =0.42); and (b) difference in band ratio (R^2 =0.38); CI is the confidence interval, and PI is the prediction interval (α = 95%).

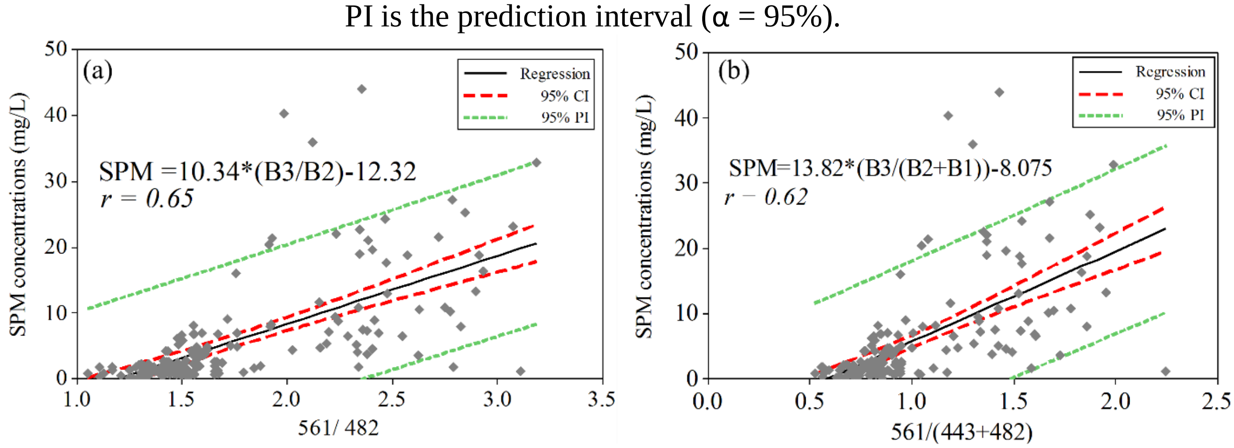

5.3.4 SPM Mapping

For SPM mapping (Figure 5.6), we used the best models from approach iii, however, the most reliable results were obtained using the approach “c”. Therefore, the SPM maps from approach “c” are shown in Figure 7 for BB2, BAR1, IBI1, and NAV1 reservoirs. The SPM maps shown in this Figure are derived from model I application (SPM = 10.34*[561/482]-12.32). The SPM retrieval model I resulted in the lowest error on average (nRMSE = 32.97%, MAPE = 47.05%). The model II was also applied to the images and returned poorest results (Table 5.5).

Figure 5.6 SPM mapping of (a)BB2; (b)BAR1; (c)IBI1; (d)NAV1 reservoirs. Note SPM scaling is different of each image. BAR1 shown a blank space with no data.

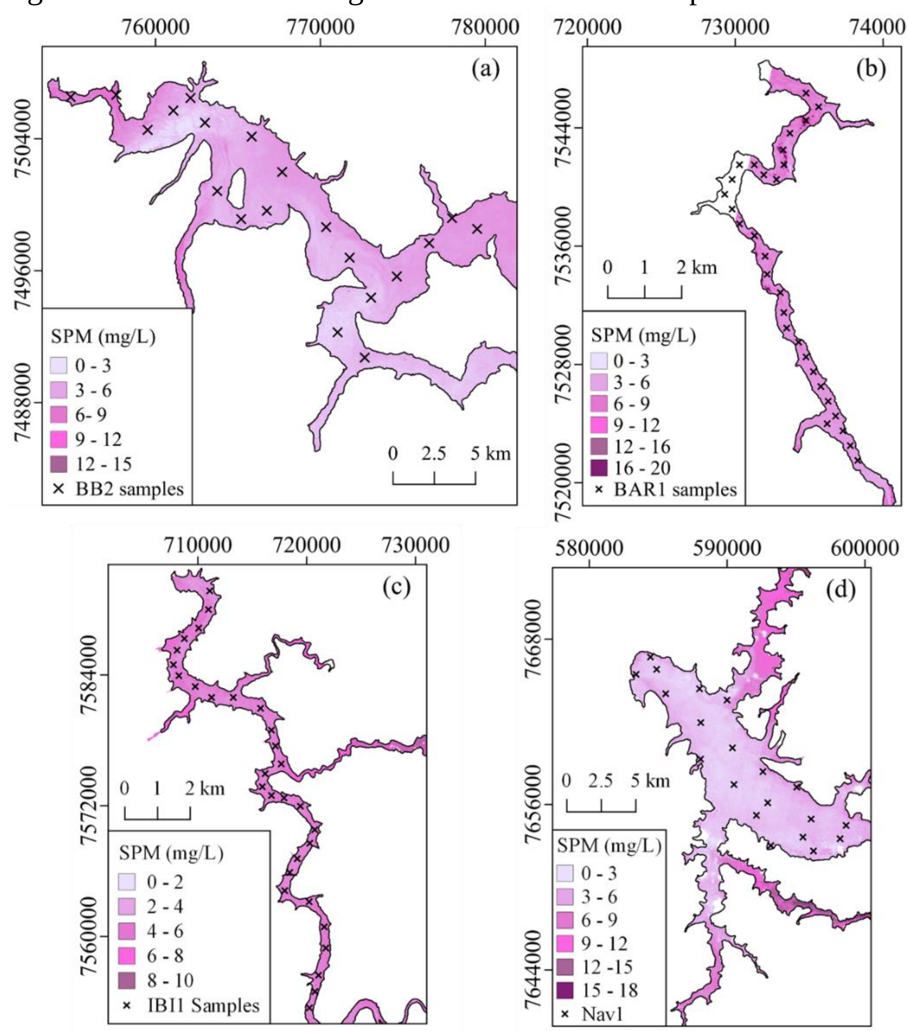

The band ratio model (Model I) retrieved a MAPE that ranged from 25.32% (BAR1) to 66.62% (BB2), whereas Model II retrieved a widely interval with a MAPE that ranged 26.81% (BAR1) and 85.35% (BB2). Regardless to the model, BB2 retrieved the highest errors and BAR1 the lowest errors. On average, Model I presented a RMSE = 6.5 mg.L-1, a nRMSE = 32.97%, and a MAPE = 47.05%; Model II presented a RMSE = 8.36 mg.L-1; a nRMSE = 39.78%, and a MAPE = 63.86%. Although the nRMSE from model I and II varied only 7%, MAPE differences reached 15% approximately. The estimated and measured SPM concentrations were compared using histogram (Figure 5.7)

Table 5.5 Error assessment of SPM model from approach “c” applied to OLI images.

	Model I			Model II		
Field	**RMSE**	**nRMSE(%)**	**MAPE(%)**	**RMSE**	**NRMSE(%)**	**MAPE(%)**
BB2	13.56	40.84	66.62	20.5	61.82	85.35
BAR1	9.62	26.21	25.32	10.30	28.07	26.81
IBI1	2.11	30.65	55.53	1.73	25.13	64.79
NAV1	0.72	34.20	40.88	0.93	44.12	78.50
Average	6.5	32.97	47.05	8.36	39.78	63.86

Figure 5.7 Comparisons between estimated (from OLI images) and measured SPM concentrations in (a)BB2; (b)BAR1; (c)IBI1 and (d)NAV1.

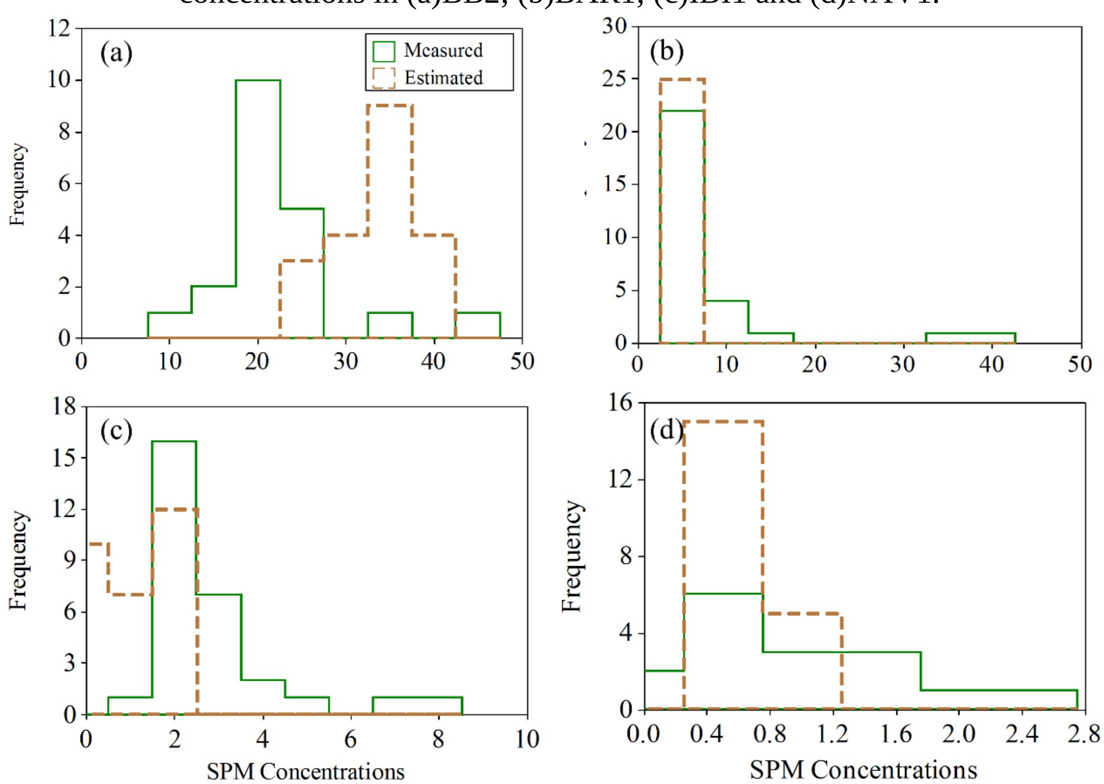

5.4 DISCUSSION

The use of in situ R_{rs} to estimate SPM concentrations is physically relied on the proportional relation between backscattering and SPM, which causes the enhancement of R_{rs}. Three experiments were conducted in order to better understand the effects of our samples into the SPM model, by considering the nature of reservoir and the existence of a gradient from the entire cascade.

Investigation (i) provided an R^2 higher than other investigations, where in 655 nm for BAR1 provided a $R^2 = 0.56$ ($r = 0.75$), however, when it was validated the MAPE value resulted in 80% of error, approximately. The nRMSE was not evaluated in this case due to its dependence to the maximum and minimum SPM concentrations encountered in the field, which could contribute to smooth the error. Investigation (ii) did not improve the models, on the contrary, when two datasets from a specific reservoir was used to calibrate the model, the worst performance was obtained. It can be caused by differences in atmospheric conditions or even due to the SPM composition, such as the variation in organic:inorganic fraction, or the inorganic variation in terms of sandy or clay components. In addition, the size and shape of particles of SPM also affects the backscattering properties (Lobo et al., 2014), which affect the performances of a single model when applied to another optical conditions. These effects were not investigated throughout this work.

Considering the investigation(iii), that used the entire dataset to calibrate the model and divided the entire dataset into calibration and validation groups, the best SPM retrieval models were established using the green band - errors of 25% in Approach "a", and error of 17% in Approach "b"(Table 5.4). However, the models derived from Solver optimization (approach "a") were not suitable to represent the widely variation of SPM concentrations ($R^2 = 0.22$, Figure 5.4). When we randomly divided the dataset by Python optimization (from approach "b"), the retrieved models were not sensitive to the SPM variations, mainly because when we check the calibration dataset, the maximum SPM concentrations were not included. It is known that empirical models are strongly dependent to the dataset used in calibration (Han et al., 2016), being more sensitive where higher values are included to provide the model. The same occurred when some minimum values of SPM were leaved out in calibration, resulting to an overestimation of SPM concentrations.

Overall, approach “c” that included the entire dataset of TRCS in calibration step retrieved better results, where Model I that used a simple band ratio (561/482 nm), provided more suitable SPM estimates than Model II that included a coastal band to minimize the atmospheric effects (Bernardo et al., 2017). The calibration results (Figure 5.5) did not presented significant differences in correlation coefficient (0.65 against 0.66), however, when it was applied to the OLI images, the average MAPE varied almost 20% among them. These differences can be resulted from the effect of coastal OLI band into the model, since the atmosphere effects are markedly expressive in lower wavelengths due to the attenuation caused by the atmospheric components absorption (Vanhellemont, 2019). Then, applying an atmospheric correction into original OLI images can improve the signal of OLI bands in the blue range and also can contribute to a better accuracy of Model II.

In general, when we compared all results, the most suitable SPM retrieval model was the green:blue ratio, that was capable to be sensitive of 65% of SPM variation (Figure 5.5) and also was capable to reduce the effects related to composition and grain-sizes of suspended particles. It is important to highlight that high SPM concentrations in Figure 6 are located out of the confidence interval, which indicated that green:blue ratio is suitable to moderate SPM concentrations (it means, lower than 25 $mg.L^{-1}$). These samples also presented Chl-a concentrations lower than 250 $mg.m^{-3}$. Another relevant issue in respect to band ration is the light variability that is cancelled, due to the division of spectral bands (Doxaran te al., 2002), producing reliable SPM estimates mainly in BAR1 (MAPE = 25.32% and nRMSE = 26.21%).

Using the model I to map SPM in TRCS, it is possible to see that tributaries normally presented higher SPM concentrations than the main channel of the reservoir. Higher concentrations were retrieved in BB2 and BAR1 (Figure 5.6 – a, b), where lower concentrations were found at IBI1 (Figure 5.6 – c) and NAV1 (Figure 5.6– d). As expected, there is a SPM gradient from up to downstream reservoirs (Bernardo et al., 2018) that was demonstrated in SPM mapping. Besides, BAR1 and IBI1 presented the most homogeneous spatial SPM distribution, as observed the frequency of classes in histogram at Figure 5.7 (b and c). It is important to highlight that in situ SPM concentrations found in BAR1 presented the major frequency between 0-10 $mg.L^{-1}$ - the same predicted by Model I (Figure 5.7 – b), however, for SPM > 10 $mg.L^{-1}$, Model I was not considered suitable to retrieve these values.

In BB2, model I was capable to estimate SPM concentrations between 20-40 mg.L^{-1}(Figure 5.7 – a), overestimating the retrieval concentrations of SPM, however, the frequency of histogram follow the same standard. The classes with high frequencies of SPM were well estimated in IBI1 (0 – 2.0 mg.L^{-1}) and NAV1 (0.3 - 1.2 mg.L^{-1}), but some values that are located away from this range, were not estimated.

Our investigations demonstrated that empirical modelling trends to estimate the mean values, it means, the major frequencies of SPM, but failed to estimate the highest values, indicating that the potential of analytical models to better retrieve SPM over a widely range. Analytical models, due to its physical background, are not dependent of some environmental effects such as the solar illumination, widely SPM composition and concentrations, and the variability of R_{rs} derived from image (adjacent effects, atmospheric condition variations, pixel mixture), that can degrade the SPM estimates.

5.5 CONCLUSION

Our investigations were conducted in order to identify the best single empirical model to retrieve SPM concentrations over a widely range of SPM in inland water systems. Other relevant contributions were evaluating the effect of a single or band ratio, and the assessment of including different datasets to provide the most reliable model. Our results indicated that when we mixed two datasets sampled in the same reservoir, the calibrated model degrades its performance to estimate SPM, retrieving errors near 80%. When we grouped the entire dataset collected over a widely range of SPM concentrations, the model became more robust, and it is more sensitive to derive SPM concentrations in this widely interval. The response of a robust model, when applied to the satellite images, reduced almost 50% of errors in some cases.

Overall, the errors of validation obtained using the OLI/Landsat-8 images (approach “c”) were almost three times lower than the validation using the field dataset (approaches “a” and “b”). Another important conclusion was regarded to the inclusion of coastal band into the model aiming to minimize the effect of atmosphere. Instead of reducing the error, the model that contained the coastal band retrieved higher errors when compared to the model that used a simple green:blue ratio. This result indicates that atmospheric correction effects are capable to reduce the performance of SPM retrieval models due to the overestimation of

SPM concentrations in OLI/Landsat-8 images, once both models presented a comparable calibration metrics.

In conclusion, the SPM empirical model adjusted in this paper was capable to retrieve the most frequently SPM values in TRCS, however, need to be improved in order to be able in retrieving the higher SPM concentrations. Scholars (Watanabe et al., 2016; Rodrigues et al., 2017) has shown that the use of semi-analytical models can reduce the errors if compared with empirical approaches, pointed out an alternative to investigate the analytical modelling in TRCS.

5.6 SUPPLEMENTARY FILES

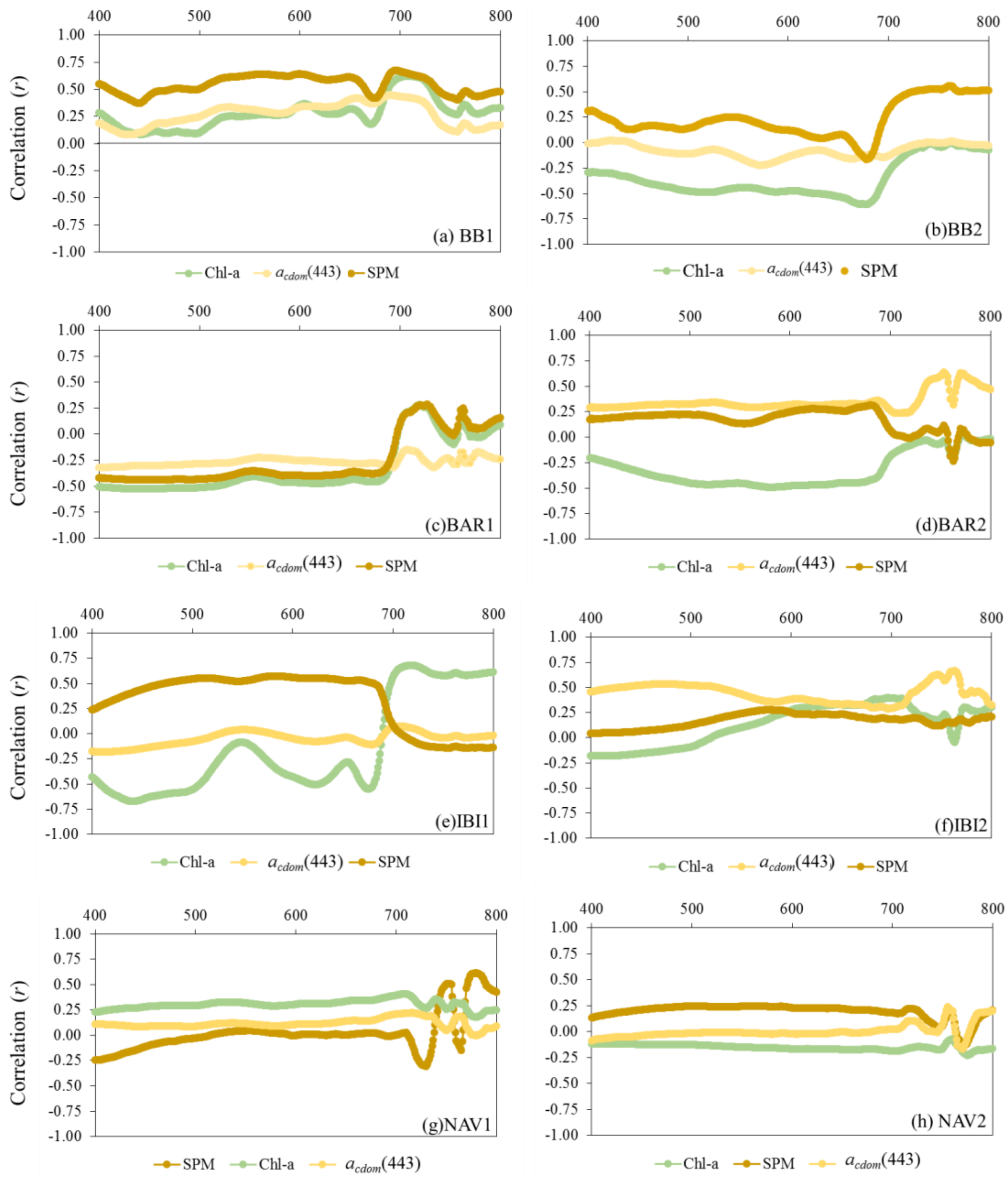

Figure S.5.1. Hyperspectral correlations between R_{rs} and Chl-*a*, SPM and a_{cdom}(443).

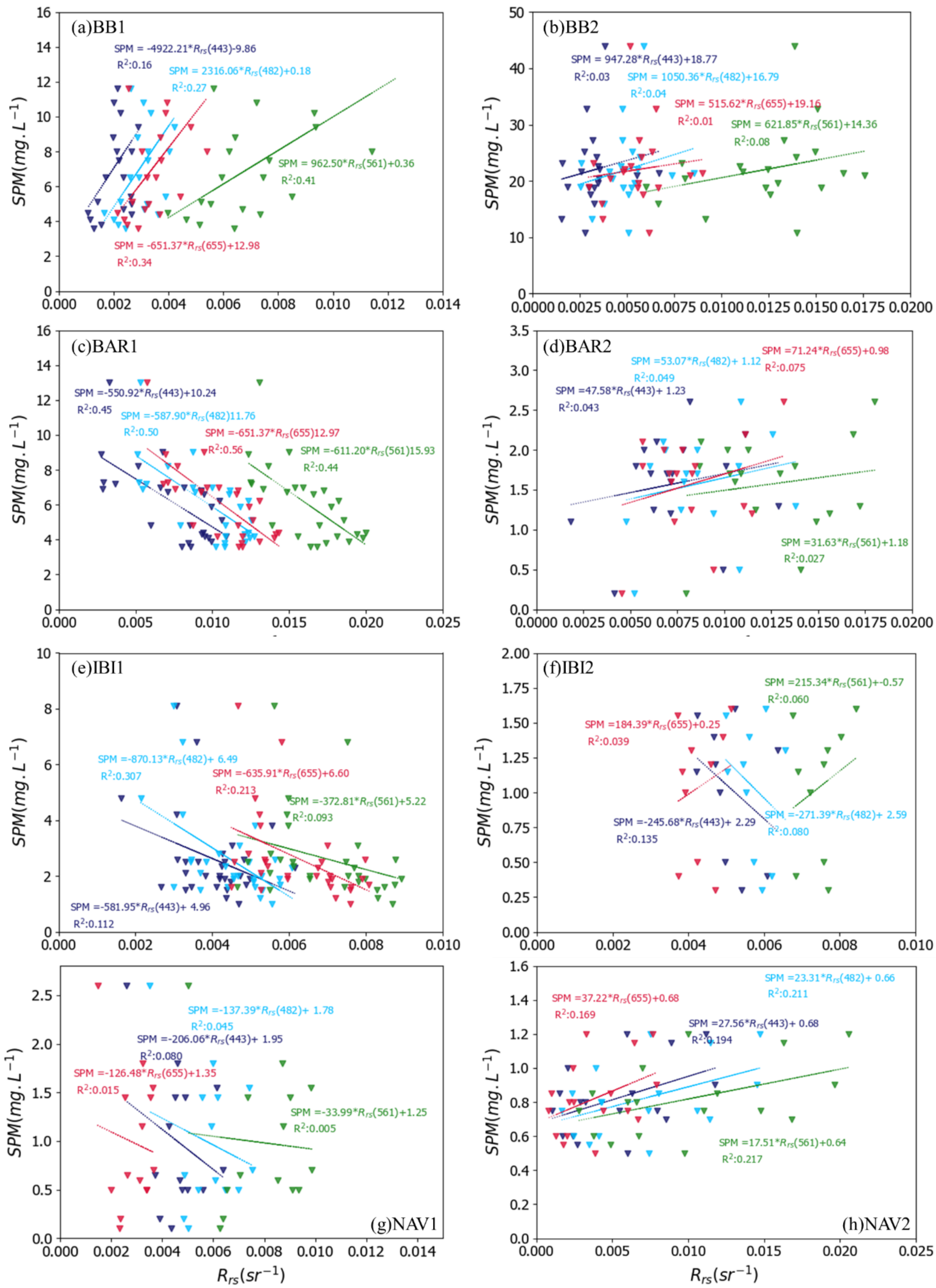

Figure S.5.2 Plots of SPM against R_{rs} considering OLI spectral bands and fieldworks.

CHAPTER 6: RETRIEVAL OF SUSPENDED PARTICULATE MATTER IN INLAND WATERS WITH WIDELY DIFFERING OPTICAL PROPERTIES USING A SEMI-ANALYTICAL SCHEME

This chapter was published in the **Remote Sensing** Journal. doi:
doi.org/10.3390/rs11192283

6.1 SCOPE

Suspended Particulate Matter (SPM – see Table 1.1 for symbols and acronyms) is a major component of the aquatic environment and plays an important role in hydrophysical functioning and biogeochemical cycles of inland waters (Lymburner et al., 2016). It essentially controls, through the absorption and backscattering of light, the turbidity and photosynthetic activities in the water column, and thus mapping the distribuition of SPM concentration is considered critical in water resource management. High levels of SPM may alter the nutrient composition available on water and decreases the water clarity, affecting the light penetration through the water column (Billota and Brazier, 2008). The gradient of available energy underwater determines the biogeochemical cycles and biodiversity of aquatic organisms (Gordon et al., 1977, Kahn et al., 2018).

Although the SPM in inland water systems has been monitored through several different approaches (Edward et al., 2019), remote sensing can be considered the most promising and efficient way to map the large-scale spatiotemporal dynamics of SPM (Pahlevan et al., 2014; Pham et al., 2019). SPM could be estimated from IOPs or AOPs optical properties using empirical or analytical models (Odermatt et al., 2012). Using the IOPs, SPM concentrations can be obtained by employing spectral absorption index (SAI, Liu et al., 2018) or by applying empirical regressions with backscattering coefficient (b_b) (Lobo et al., 2015). Using the AOPs, SPM can be derived from the remote sensing reflectance (R_{rs}) from unique or band ratios (Matthews 2012, Gernez et al. 2014). Establishing a reliable model to estimate SPM concentration using R_{rs} in inland waters, however, is still considered a challenge, because R_{rs} saturates at certain levels of SPM (Luo et al., 2018). Further, the chlorophyll-*a* (Chl-*a*), colored dissolved organic matter (CDOM), and organic and inorganic fractions of SPM imply in different interactions with incident energy, resulting in a widely range of a and b_b coefficients (Ritchie et al., 1976; Rodrigues et al. 2017). An example of widely range of IOPs is the Tietê River, in which the phytoplankton absorption coefficient at 443 nm, $a_{\emptyset}$, ranges from 0.02 to 10.9 m^{-1} (Bernardo et al., 2019).

The Tiete River is an important water resource for the communities at the local scale providing valuable drinking water, food sources, irrigation, water for industrial use, transportation and recreation (Watanabe et al., 2016), thus the water quality of the river is considered a critical issue in this region. Despite a series of six hydroelectrical reservoirs along the Tietê River Cascade System (TRCS) constantly filtering the water, several intensive anthropogenic activities occurring within the catchments (e.g. agriculture, dredging, industrial production, fishing activities). Therefore, different types of water draining the surrounding catchments are impacting directly the dynamics of SPM in the Tiete River (Watanabe et al., 2015; Gomes et al., 2018). The several types of water along the reservoirs as well as the filtration process occasioned by the sequential dams in TRCS, result in a wide range of magnitude concentration and varying composition of SPM.

Several attempts were made to assess the spatiotemporal patterns of SPM in TRCS, however they were not successful in retrieving a robust result. For instance, empirical algorithms were used for a specific (Bernardo et al., 2015) or combined reservoirs (Rodrigues et al., 2017b), nevertheless they could not develop a universal model that accounts for a large variability in SPM concentrations. Up to now, no methods to estimate SPM concentration in the cascade system exist that account for both the varying composition and a wide-ranging (and spatially heterogeneous) concentration of SPM.

In this paper we used diffuse attenuation coefficient (K_d) values as the key parameter for SPM retrieval. K_d is dependent on several factors, including depth (z), incident light (E_d), IOPs (a and b_b) and OACs (Chl-*a*, CDOM and SPM). In the inland water systems such as the TRCS, the SPM concentrations are the main OAC that controls the K_d values (Ma et al., 2016). As an AOP, K_d is largely determined by the IOPs (a and b_b) and secondarily on the light field geometry (Kirk, 2011). Therefore, K_d can be more stable than the R_{rs} in estimating SPM because K_d is directly derived by the sum of IOPs (Kirk, 2011) while R_{rs} is related to the ratio of IOP. Due to the analytical configuration of both, R_{rs} can saturate at certain point of SPM concentration (Hardley et al., 2019). In addition, K_d is also easier to validate if compared with a SPM model based on b_b (Martinez et al., 2015; Devlin et al., 2008). Then, mapping SPM using K_d can covers the gap in widely SPM concentrations modeling which was explored in coastal waters (Devlin et al., 2008) but not totally investigated in inland waters.

We aim to develop a semi-analytical scheme based on K_d to estimate SPM in the TRCS, with enough sensitive to capture the widely varying OACs effects. To do this the IOPs (a and b_b) are estimated using the Quasi-Analytical Algorithm (QAA, Lee et al. 2002) and the K_d is estimated based on Lee et al. (2013). The QAA has been tested for some of reservoirs of TRCS (e.g. Watanabe et al. 2016 and Rodrigues et al. 2018) and the results suggested that some re-parameterizations of QAA are required to provide more accurate results. The K_d model from Lee et al. (2013) was also evaluated for inland waters (Gomes et al. 2018; Rodrigues et al., 2018) and provided the lowest error when compared with other published algorithms. However, Lee's model was never tested for the entire TRCS. The specific objectives are to (i) re-parameterize the QAA considering the optical composition and the available spectral bands onboard Landsat-8; (ii) compare our results with other versions of QAA tuned for inland waters; (iii) evaluate the suitability OLI bands to estimate K_d; and (iv) evaluate K_d retrieved by a semi-analytical scheme;(v)evaluate the influence of different water compositions into SPM estimates.

6.2 DATA AND METHODS

Study sites in this chapter and respective water quality parameters sampled in situ are described in Table 6.1. The map of our study area is illustrated in Chapter 2, Figure 2.1.

Table 6.1 Study sites and sampled parameters in Barra Bonita, Bariri, Ibitinga and Nova Avanhandava reservoirs (see table 1 for acronyms and symbols).

<table>
<tr><th>Reservoirs</th><th>Field Campaign ID</th><th>n</th><th>Time acquisition</th><th>Radiometric variables</th><th>Water quality and physical parameters</th></tr>
<tr><td>Barra Bonita</td><td>BB1/BB2</td><td>20/20</td><td>May / October, 2014</td><td rowspan="6">L_t, L_{sky} E_s, and E_d
a_t (a_{cdom}, a_{phy}, a_{nap}) and b_b</td><td rowspan="6">Turbidity, Z_{SD}, SPM, PIM, POM, Chl-a, Wind Speed and Depth.</td></tr>
<tr><td rowspan="2">Bariri</td><td>BAR1</td><td>30</td><td>August, 2016</td></tr>
<tr><td>BAR2</td><td>18</td><td>June, 2017</td></tr>
<tr><td rowspan="2">Ibitinga</td><td>IBI1</td><td>30</td><td>July, 2016</td></tr>
<tr><td>IBI2</td><td>16</td><td>June, 2017</td></tr>
<tr><td>Nova Avanhandava</td><td>NAV1/NAV2</td><td>20/20</td><td>May / September, 2014</td></tr>
</table>

Turbidity (NTU), wind speed ($m.s^{-1}$), Secchi Disk Depth (Z_{SD}; m) and bottom depth (m) were measured a triplicate with portable turbidimeter, anemometer, a Secchi Disk (diameter of 30 cm), and a depth gauge. As Z_{SD} is much lower than the average depth of the reservoir, the samples are located in deep waters (without bottom reflectance effects), which mean that the bottom effects are negligible. SPM concentrations, and organic and inorganic fractions were retrieved using a Whatman GF/F filters (47 mm of diameter and 0.7 pore size) following the protocol in APHA (1998). Chl-*a* concentrations were determined using the method described in Golterman et al. (1998).

Radiometric measurements (E_d, E_s, L_{sky} and L_t) were obtained using TriOS Hyperspectral radiometers (RAMSES TriOS ®), for 400 to 900 nm wavelength. Measured radiance and irradiance (at 3.3 nm resolution) were interpolated to 1 nm resolution and the same geometry was adapted in all field surveys (Mueller et al., 2000; Mobley, 1999). The R_{rs} variable was calculated using a spectral glint removal method (Lee et al., 2010), which is considered the most reliable (Bernardo et al., 2018).

We measured the particulate absorbance using dual-beam UV-2600 UV–VIS spectrophotometer (SHIMADZU, Japan) at 1 nm resolution, from 280 to 800 nm. Trasmittance-Reflectance (T-R) method was used to calculate the particulate absorption ($a_p = a_{nap} + a_{\varphi}$) described in Tassan and Ferrari (1995, 1998). To bleach the organic fraction of particulate, samples were washed using hypoclorite solution (NaClO at 10%). We used an absorption coefficient of cdom (a_{cdom}) was established by Bricaud et al (1996), that uses a reference correction - a mean absorption value over 700 and 750 nm was subtracted from the entire spectrum curves.

The integration of volume scattering function (VSF) retrieved the backscattering coefficients from HydroScat-6P (HobiLabs, Bellevue-USA) and ECOBB-9 (WetLabs, Philomath-USA) measurements (more details are disposed in Watanabe et al., 2018). The absorption correction was made using laboratory measurements, and exponential fitting was applied in order to standardize the wavelengths to be in accordance with the outputs from QAA. A flowchart showing the methodology described in this section is given in Figure 6.1.

Figure 6.1 Workflow used in this study.

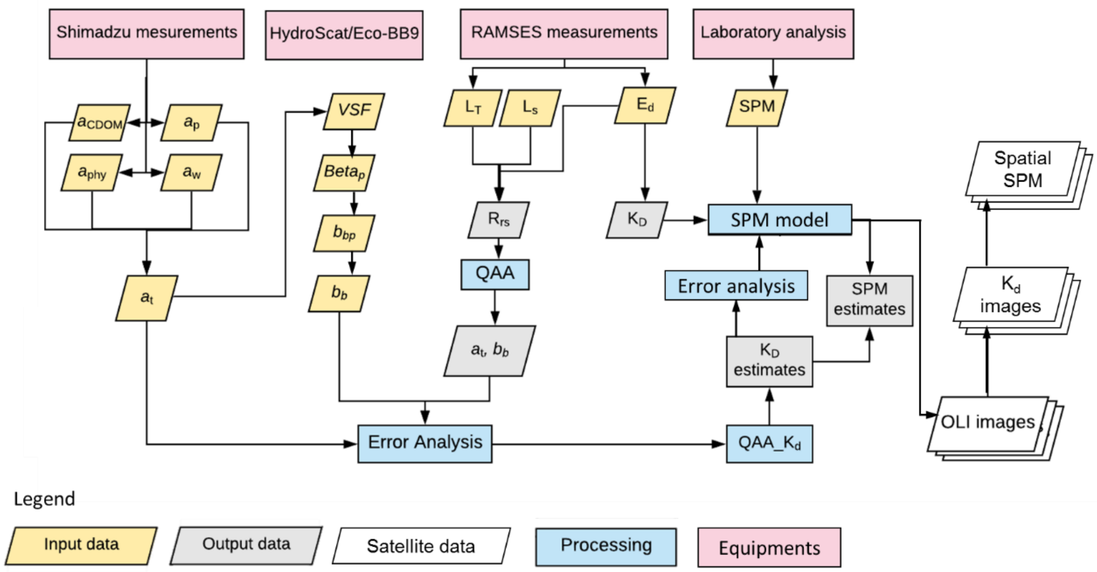

6.2.1 K_D from IOPS

K_d estimates were derived using IOPs obtained from QAA modeling through the seven steps (Figure 6.2). The empirical steps from version 5 of QAA (v5, Lee et al., 2002) were calibrated based on coastal waters, where $a_t(55x)$ might be less than 0.5 m^{-1}. Broader applications for inland water require several site-specific adaptations, mainly in the empirical steps (Mishra et al., 2014; Li et al., 2013). The main error sources are related to (i) the reference wavelength (λ_0) and the estimations of absorption coefficient; and (ii) the spectral power slope (Υ) used to compute b_b (Yang et al., 2013; Yang et al., 2014). Furthermore, the empirical steps in QAA also depends on the local of sample dataset (Zhu and Yu, 2013). The former limitation implies that re-parameterization of the coefficients are necessary because the optical conditions of water are distinct from the original study sites.

The QAA derives a and b_b from R_{rs}, which is referred to as Part I (Xue et al., 2019). The second part of QAA, which determines specific coefficients of each OAC, was not assessed in this paper. The main changes in the parameters used the QAA steps to improve its performance for inland waters were adapted from published results, which are summarized in Table 6.2.

Figure 6.2 QAA steps to provide *a* and b_b from in situ R_{rs} at λ_0 from version 5 (Lee et al., 2002). The $a_w(\lambda_0)$ and $b_{bw}(\lambda_0)$ was assumed from Pope and Fry (1997) and Smith and Baker (1981). Highlights for (i) and (ii) steps.

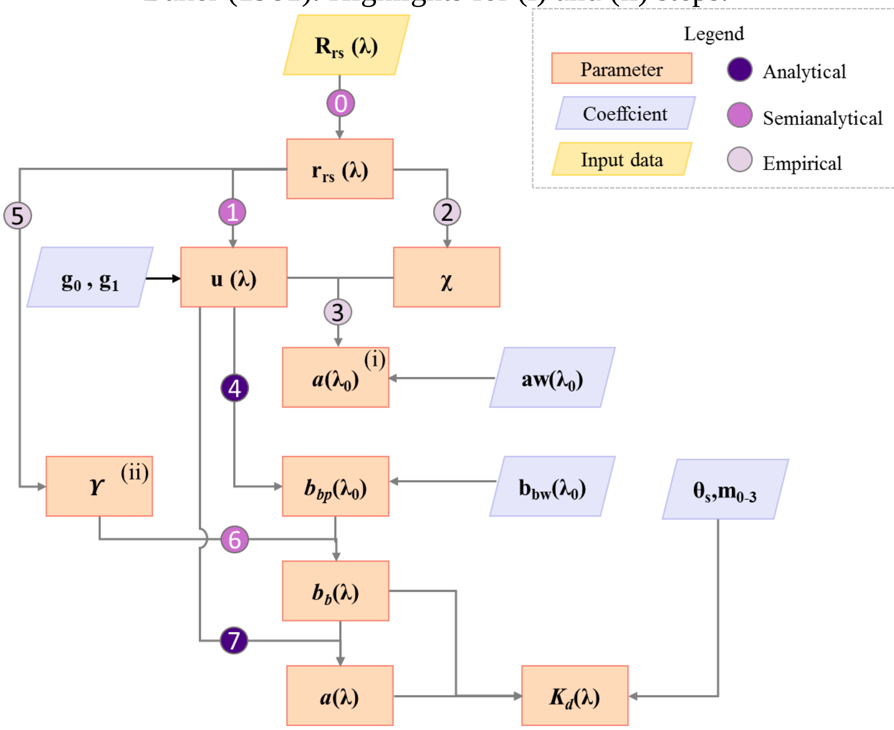

Regarding to the Part I, we modified four steps of the original frame of QAA to establish a QAA for TRCS (QAA_{TRCS}). In the 'zero' step we computed r_{rs} using spectral coefficients as described in Wang et al. (2017), which provides better results for inland waters. The parameters in the empirical steps 2 and 3 were not recalibrated; however, the λ_0 were displaced towards 655 nm where the water absorption is the major contributor to a_t (Figure S.6.1).

To compute χ, we modified the bands by replacing 490 nm and 667 bands to the band at 561 nm and 482 nm, to compensate the CDOM effects (Ogashawara et al., 2016). It is important to consider the multiplication factor in the denominator of χ, where we adapted the value of 5 for turbid environments (BB2 and BAR1) and 2 for non-turbid environments (>10 NTUs). The entire scheme can be found in Table S.6.1.

The coefficients to retrieve a_t in (λ_0) can be recalibrated using *in situ* datasets in step 2 (Rodrigues et al., 2018; Wang et al., 2017; Watanabe et al., 2016; Zhu and Yu, 2013). The optimization processing was used to define the best band combination for computing χ factor (Rodrigues et al., 2018; Watanabe et al., 2016). On the other hand, the Υ factor can be established for different purpose with other spectral bands (Rodrigues et al., 2018; Wang et al., 2017) or by testing new coefficients (Watanabe et al., 2016).

Table 6.2 QAA steps and adaptations from [1] Lee et al., (2005); [2] Zhu and Yu (2013); [3] Wang et al. (2017); [4] Ogashawara et al. (2016); [5] Watanabe et al., 2016; [6] Rodrigues et al., 2018. Steps 3, 5 and 6 were omitted because changes in QAA were not made.

Step	Par.	[1]	[2]	[3]	[4]	[5]	[6]
0	r_{rs}	T = 0.52 γQ = 1.7	T = 0.52 γQ = 1.7	$= \frac{R_{rs}(\lambda)}{\alpha(\lambda)+\beta(\lambda)R_{rs}(}$	-	-	-
1	$u(\lambda)$	g_0 = 0.089 g_1 = 0.125	- -	- -	-	-	-
2.1	$a_t(\lambda_0)$	$\lambda_0 \geq 55x$ h_0 = -1.146 h_1 = -1.366 h_2 = -0.469	555 -1.226 -1.214 -0.35	680 -0.0852 0.8650 0.9398	-	709 -0.7702 0.0999 0.0566	709 -1.148 2.814 -5.813
2.2	χ	$\alpha = 5$ $\lambda_1 = 443$ $\lambda_2 = 490$ $\lambda_3 = 667$ $\lambda_4 = 490$	- 440 490 640 490	- 680* 490 - -	- 412 560 665 443	- 443 665 620 443	0.05 443 665 681 443
4	Y	$y_0 = 2.0$ $y_1 = 1.2$ y_2 = -0.9 $\lambda_5 = 443$	-	m = 1.75* n= -0.05 - -	-	1.0 - 1.9 1.3 - 1.5 0.1 - 0.8 $\lambda_5 =$ 443	– – – 665/754 **
6	$a(\lambda)$	C_1= 1	-	-	$r_{rs}(\lambda_4)/r_{rs}(\lambda_0)$	-	-

*Band ratio = (680/490) and quadratic fit were used; Y = m x $b_{bp}(680)^n$; **Band ratio to establish Y instead of 443/λ_0

The outputs of QAA, *a* and b_b, allow computing K_d values as (Equation 6.1):

$$K_{d\_QAA}(z,\lambda) = (1 + m_0 \times \theta_s)a(\lambda) + (1 - \gamma \frac{b_{bw}(\lambda)}{b_b(\lambda)}) \times m_1 \times (1 - m_2 \times e^{-m_3 \times a(\lambda)})b_b(\lambda) \quad (6.1)$$

Where $K_{d\_QAA}(z,\lambda)$ is the K_d calculated from QAA using OLI/Landsat-8 bands; m_{0-3} and γ are set to 0.005, 4.26, 0.52, 10.8, and 0.265, respectively, which are the coefficients obtained via Hydrolight simulations (Lee et al., 2013). θ_s is the solar zenith angle (considered as 30°); $b_{bw}(\lambda)$ is the backscattering coefficient for water molecules (adopted from Smith and Baker, 1981); and *a* and b_b are the spectral coefficients derived trough QAA model (Lee et al. 2002).

6.2.2 K$_D$ of Reference Dataset

To establish the SPM model for TRCS, we used *in situ* K$_d$ as a predictor variable, to be applied to the satellite images later. K$_d$ values were retrieved from the field measurements of normalized irradiances, E$_d$ and E$_s$. To distinguish *in situ* K$_d$ from that the other derived from QAA, we referred the reference K$_d$ as K$_{d_r}$ and the other as K$_{d_QAA..}$ K$_d$ is mathematically described as an exponential function that represents the decrease of light, i.e., the reduction of available E_d^- within the water column at a certain depth (z) (Mobley, 1994) (Equation 6.2).

$$K_d(z,\lambda) = -\frac{1}{E_d^-(\lambda)}\frac{dE_d^-}{dz} \tag{6.2}$$

The *in situ* measurements of E_d^-, or also called $E_d(z_i)$ is affected by changes of sun geometry that result in variability of incident light field, and consequently cause uncertainties into K$_{d_r}$. In order to minimize the illumination variability, we normalized to E$_d$(z) based on Mueller (2000) and Mishra et al. (2005) (Equation 6.3):

$$E'_d(z_i,\lambda) = -\frac{E_d(z_i,\lambda)E_S(t(z_1),\lambda)}{E_S(t(z_i),\lambda)} \tag{6.3}$$

The normalization factor is defined as the ratio between E_s at first sensor scan at t(z$_1$), $E_s(t(z_1),\lambda)$, and the following sensor scans along the depth at t(z$_i$) , $E_s(t(z_i),\lambda)$. E_s is the downwelling irradiance measured from the roof of the boat, and $E'_d(z_i,\lambda)$ is the normalized E_d within water column in all downward directions (Mobley, 1994). Finally, the reference values of K$_{d_r}$ were computed as Equation (6.4):

$$K_{d\_r}(z,\lambda) = -\frac{1}{E'_d(\lambda)}\frac{dE'_d}{dz} \tag{6.4}$$

6.2.3 SPM Analytical Modeling

SPM concentrations were defined as criterion variable estimated based on scores of K$_{d_r}$. The linear, quadratic, power and exponential fits were tested using K$_{d_r}$ at 443 nm, 482 nm, 561 nm and 655 nm. The best fit, based on higher correlation coefficients (Table 6.3) was chosen, which is the model using K$_{d_r}$(482) that yielded r = 0.79, followed by K$_{d_r}$(655)

with r = 0.74. The 655 nm band is also considered suitable for turbid inland waters (Shi et al., 2014; Zhang et al., 2012).

Table 6.3 Best fits between K_{d_r} resampled for OLI bands and SPM concentrations considering the entire TRCS's dataset. *a,b* and *c* are the coefficients for linear ($ax+b$); quadratic (ax^2+bx+c); power (ax^b) and exponential ($a\ln(x)+b$) equations.

Model ID	OLI band	*a*	*b*	*c*	*r*	Fit
M1	443 nm	3.17	-2.57	-	0.73	Linear
M2	482 nm	0.22	2.27	-0.53	0.79	quadratic
M3	561 nm	3.50	1.39	-	0.61	power
M4	655 nm	2.51	1.64	-	0.74	power

QAA_{TRCS} equations was applied to the OLI images (Table 6.4) level 2 also named as LASR (Zanter, 2018), it means, they were atmospherically corrected. LaSRC provides suitable spatiotemporal resolutions for monitoring inland waters (Bernardo et al., 2016). Previous works also demonstrated that water quality parameters are well estimated via OLI images (Kuhn et al., 2019). Therefore, to retrieve R_{rs} images they were divided by π (Bernardo et al., 2017) and we applied the scale factor (0.0001 – Zanter, 2018). After all QAA processing, images of a and b_b were achieved. Images covering the remaining reservoirs (BB1, BAR2, NAV2) were not used for analysis due to the presence of intense cloud cover.

The IOPs images were used as input of Equation 1 and retrieved an image of K_{d_QAA}. Sequentially, M2 and M4 (Table 6.4) were applied to the K_{d_QAA} image and map SPM concentration in each reservoir. The results were assessed by comparing in situ SPM concentrations and SPM derived from images via K_d.

Table 6.4 OLI/Landsat-8 images for mapping SPM concentrations.

Coverage Area	Path/Row	Overpass date	Overpass time (UTC)	Gap*
BB2	220/076	10/13/2014	13:10:45	3h10m
BAR1	220/076	08/15/2016	13:10:36	2h05m
IBI1	221/075	07/21/2016	13:16:18	3h00m
NAV1	222/075	05/02/2014	13:22:42	2 days

*Considering the samples taken nearest the images acquisition.

6.2.4 Accuracy Assessment

The a_t and b_b derived by QAAs (Table 6.4 and Table S.6.1) were compared with the a_t and b_b obtained in laboratory and in situ, respectively. We used the Root Mean Squared Error (RMSE in sr $^{-1}$) to assess the errors; normalized Root Mean Squared Error (nRMSE in %); bias (δ in sr $^{-1}$); Mean Absolute Percentage Error (MAPE in %), and Pierson correlation coefficient (Equation 6.4 to 6.8, respectively).

$$RMSE = \sqrt{\frac{1}{n}\sum_{i=1}^{n}(x_{e,i} - x_{m,i})^2} \tag{6.4}$$

$$nRMSE = \frac{RMSE}{(\max(x_{m,i}) - \min(x_{m,i}))} \times 100 \tag{6.5}$$

$$\delta = \frac{1}{n}\sum_{i=1}^{n}(x_{e,i} - x_{m,i}) \tag{6.6}$$

$$MAPE = \frac{1}{n}\sum_{i=1}^{n}\frac{|x_{e,i} - x_{m,i}|}{x_{m,i}} \times 100 \tag{6.7}$$

$$r = \sum_{i=1}^{N}\left[\frac{x_{m,i} - \left(\frac{1}{N}\sum_{j=1}^{N} x_{e,j}\right)}{\left(\frac{1}{N-1}\sum_{k=1}^{N}\left[x_{m,k} - \left(\frac{1}{N}\sum_{l=1}^{N} x_{m,l}\right)\right]^2\right)^{0.5}}\right]\left[\frac{x_{e,i} - \left(\frac{1}{N}\sum_{j=1}^{N} x_{e,j}\right)}{\left(\frac{1}{N-1}\sum_{k=1}^{N}\left[x_{e,k} - \left(\frac{1}{N}\sum_{l=1}^{N} x_{e,l}\right)\right]^2\right)^{0.5}}\right] \tag{6.8}$$

Where $x_{e,i}$ is the estimated values, $x_{m,i}$ is the measurements, min and max are corresponding to the minimum and maximum values of dataset, and n is the number of samples. K_d derived from QAA were assessed by comparing with K_{d_r} obtained from in situ measurements as described in section 6.2.2. After the error analysis, K_d is used to estimate SPM concentrations using the models shown in Table 6.3.

6.3 RESULTS

6.3.1 Inputs of SPM Modeling

The in situ dataset of R_{rs}, as well as total absorption curves are shown in Figure 6.3. Different magnitudes through the R_{rs} spectra are widely caused by the varying concentration of OACs. The green (500-600 nm) and NIR bands (>700 nm) are the ranges most sensitive to SPM. High level of CDOM displaces the 550 nm- R_{rs} peak toward near 600 nm, as observed in BAR and IBI field surveys. Furthermore, higher Chl-*a* concentrations contribute to the high absorption in the blue range as observed in BB1, BB2 and BAR1 (Figure 6.3 - b). A marked peak of R_{rs} near 550 nm is correlated with the relatively high SPM concentrations. A smaller peak around 650 nm in some curves also indicates the presence of phycocyanin, caused by the absorption feature near 620 nm (Gitelson, 1992) and 670 nm due to Chl-*a*.

Figure 6.3 (a) Mean±SD R_{rs} spectra and (b) Mean±SD total absorption spectra from all field surveys.

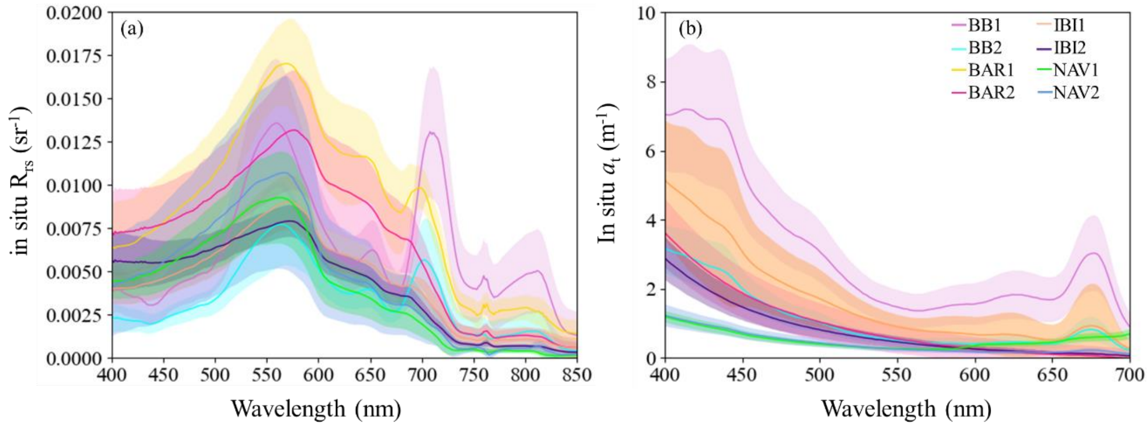

6.3.2 QAA Performances

The entire dataset of *in situ* R_{rs} was used to retrieve a_t and b_b. As mentioned above, the 655 nm band was chosen as a reference wavelength for two reasons: (i) it retrieved the best result when compared to 561 and 865 nm; and (ii) a large portion (65%) of the total absorption coefficients was dominated by water itself. Accurate estimation of QAA is essential for K_d computation (Yang et al., 2014). Errors of a_t and b_b from all tested QAA and the model developed in this study, QAA_{TRCS}, are reported in Table 6.5. Further details of QAA_{TRCS} are given in Table S.6.1.

Table 6.5 Average- δ (m^{-1}), nRMSE (%), and MAPE (%) considered all QAAs tested in this study and a_t and b_b estimates with entire TRCS's dataset.

	Estimated a_t (m^{-1})			***Estimated b_b(m^{-1})***		
QAA	**δ**	**nRMSE**	**MAPE**	**δ**	**nRMSE**	**MAPE**
Lv5	-0.67	18.8	42.3	-0.07	18.3	79.3
BBHR	-0.67	20.8	37.4	-0.08	19.8	47.0
OMW	-0.75	21.8	43.9	-0.08	19.7	39.0
CDOM	-0.32	17.7	37.6	-0.06	18.8	48.1
V	-0.60	20.4	37.7	-0.04	19.4	73.5
TRCS	-0.39	16.8	30.7	-0.06	18.6	39.5

Overall, the average nRMSE ranged between 16.8% to 21.8% for a_t; and 18.3% to 19.8% for b_b. The MAPE values presented a quietly different pattern, ranging from 30.7% to 43.9% for a_t estimates; and 39.5% to 79.3% for b_b estimates. The lowest errors were retrieved from TRCS, with nRMSE of 16.8% for a_t and the lowest MAPE (=39.0%) for b_b, resulting from QAA_{TRCS} and QAA_{OMW}.

Evaluating a_t estimates for each field campaign, overall the QAA_{TRCS} retrieved the lowest errors in reservoirs (Table S.6.2), with the MAPE ranging from 7.2% to 39.5% (except for BB2). We compared the performance of all tested QAAs and found that QAA_{TRCS}'s performance was lower than the QAA_{CDOM} (in BB1) and QAA_V (in BAR1 and NAV1), however the differences were less than 2%. It is important to highlight that the accuracy of a_t in BB2 was not very high, regardless of QAA (MAPE > 60%), and the same happened for BB1 for b_b estimates (Figure 6.4).

Regarding the b_b estimates, we observed that in non-turbid waters (turbidity < 6 NTU on average), QAA_{OMW} achieved the best performance with a MAPE ranging from 14.5% to 67.2% (Table S.6.2). In turbid waters (turbidity > 16 NTU on average), QAA_{TRCS} presented a better performance than QAA_{OMW} with the lowest MAPE values of 39.2% and 26.3%, respectively in BB2 and BAR1.

Figure 6.4 IOPs derived from QAA_{TRCS} - $a(\lambda)$ with index 1; and $b_b(\lambda)$ with index 2. The frames represent the center wavelengths of OLI bands (a) 443, (b) 482, (c) 561, (d) 655 nm. (continue)

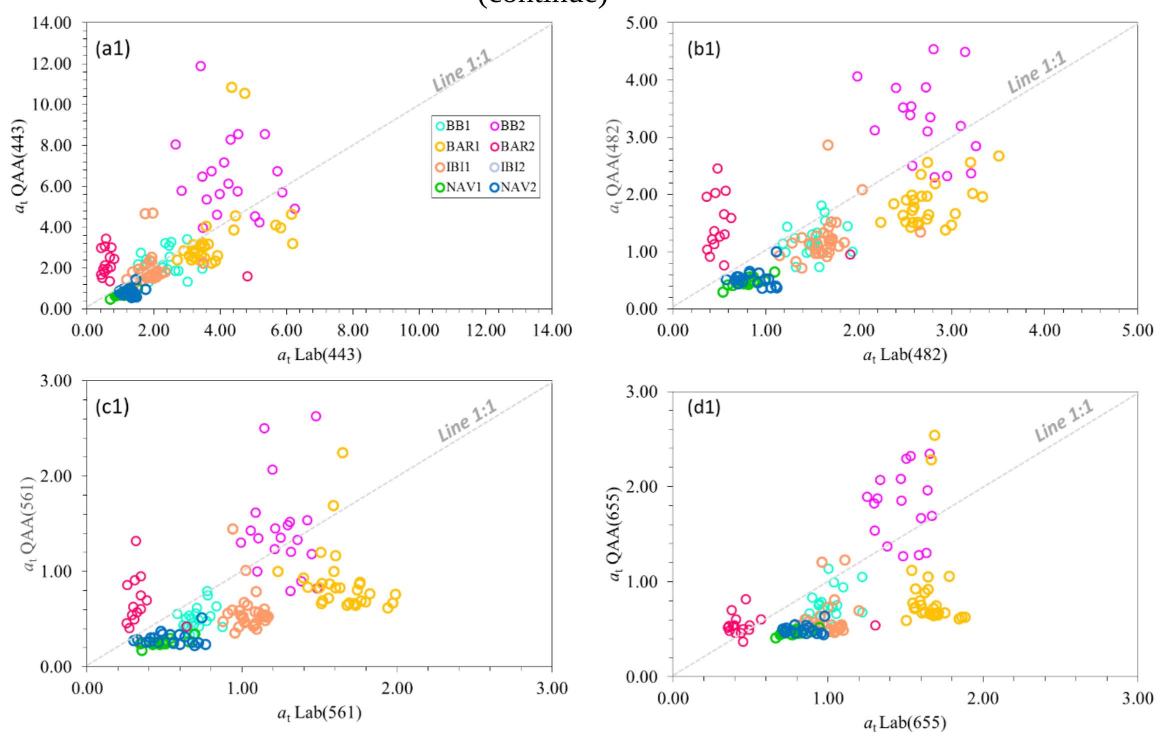

Figure 6.4 IOPs derived from QAA$_{TRCS}$ - $a(\lambda)$ with index 1; and $b_b(\lambda)$ with index 2. The frames represent the center wavelengths of OLI bands (a) 443, (b) 482, (c) 561, (d) 655 nm (end).

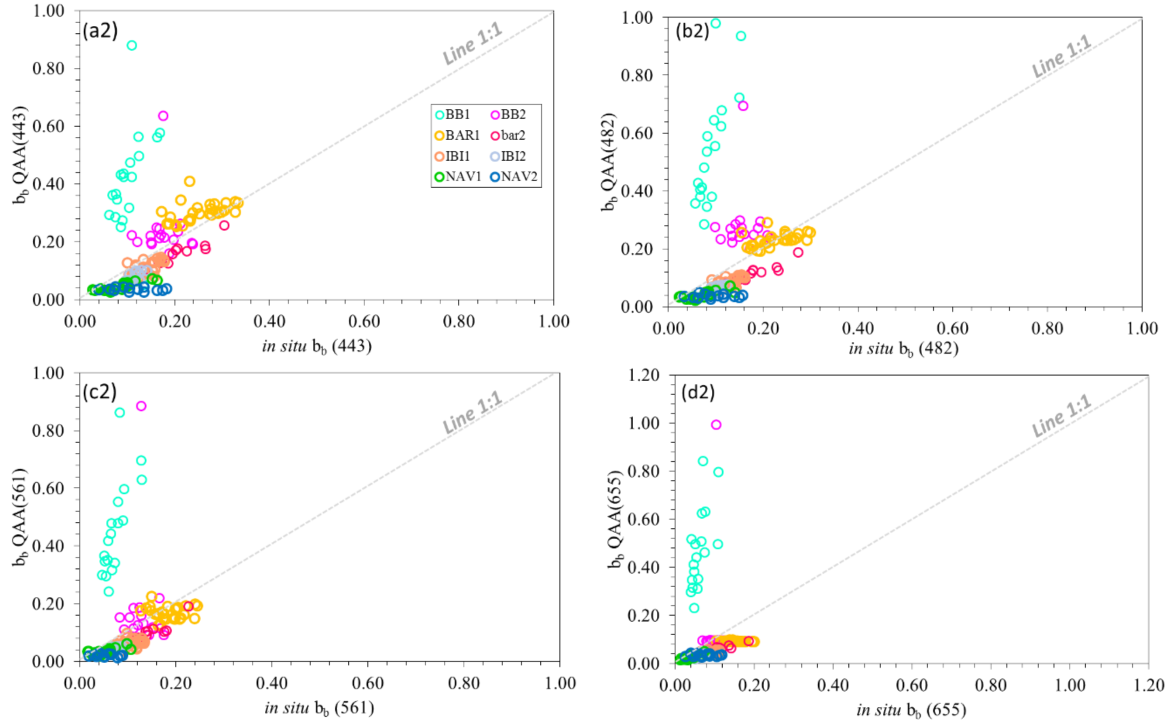

6.3.3 K$_D$ Estimates

Considering that QAA$_{TRCS}$ derived a_t and b_b with the lowest errors (Table 6.5), these outputs were used in Equation 6.1 to retrieve K$_d$. The estimated K$_d$ in central wavelengths of OLI sensor are depicted in Figure 6.5, presenting a wide range of variability and a generally decreasing trend downstream. The K$_d$(443) ranged in between 0.69 and 4.78 m^{-1} with a coefficient of variation (CV) near 43%; while in K$_d$(655) ranged between 0.64 and 1.2 m^{-1}, with CV = 16%.

Figure 6.5 K$_d$ estimates via QAA$_{TRCS}$ for entire cascade.

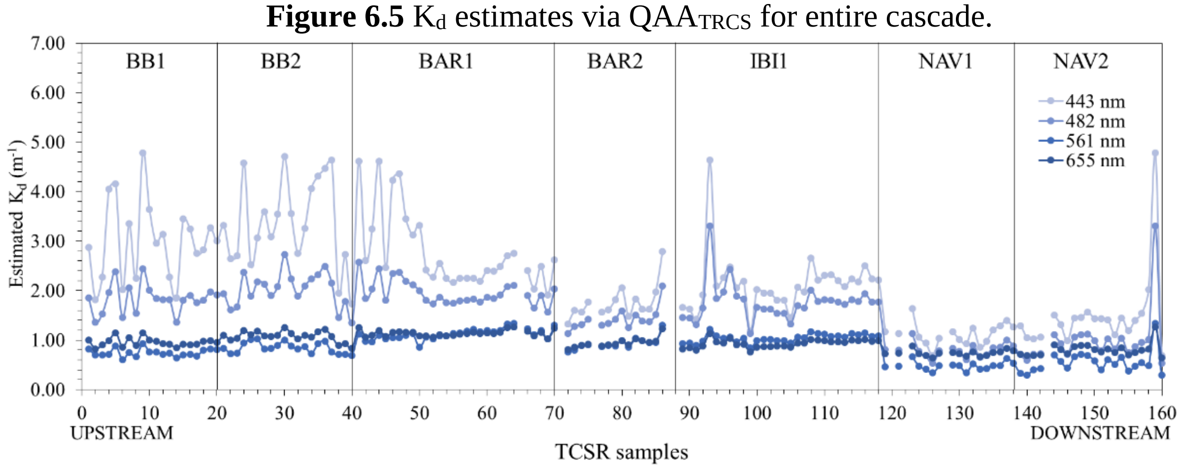

$K_d(443)$ is higher than other wavelengths, whereas the $K_d(561)$ presented the lowest values in almost all of the field surveys, except for IBI1 where $K_d(561)$ and $K_d(655)$ are similar. Overall, the highest values of K_d were observed in BB, while the lowest values were observed in NAV. The K_d estimates via QAA_{TRCS} were assessed using nRMSE for each OLI/Landsat-8 band (Table 6.6). Considering the entire dataset of TRCS (*n* = 174), comparable level of errors are shown in 561 and 655 nm. For each fieldwork, highest errors were observed in hypertrophic environments, such as in BB2 and BAR1, and and higher CDOM contributions such as BAR2, mainly at short wavelengths. Overall, the lowest average errors were retrieved from BB1 (26%) and for longer wavelengths, such as in 655 nm (39.44%). Graphical comparisons are showed in Figure 6.6.

Table 6.6 nRMSE (%) of K_{d_QAA} for the entire dataset (TRCS) and each field campaign.

DATASET	443	482	561	655	Average
TRCS	22.93	22.26	19.16	19.74	**21.02**
BB1	35.93	24.80	21.06	22.41	**26.05**
BB2	101.99	71.58	53.33	62.49	72.35
BAR1	55.59	41.15	33.43	25.83	39.00
BAR2	80.54	43.12	35.99	46.03	51.42
IBI2	52.64	62.15	24.97	22.17	40.48
NAV1	95.61	61.35	33.57	35.51	56.51
NAV2	147.39	120.03	77.23	61.62	101.57
Average	81.38	60.60	39.94	**39.44**	-

Figure 6.6 Plots of K_{d_QAA} against K_{d_r} (*in situ* K_d) considering each fieldwork.

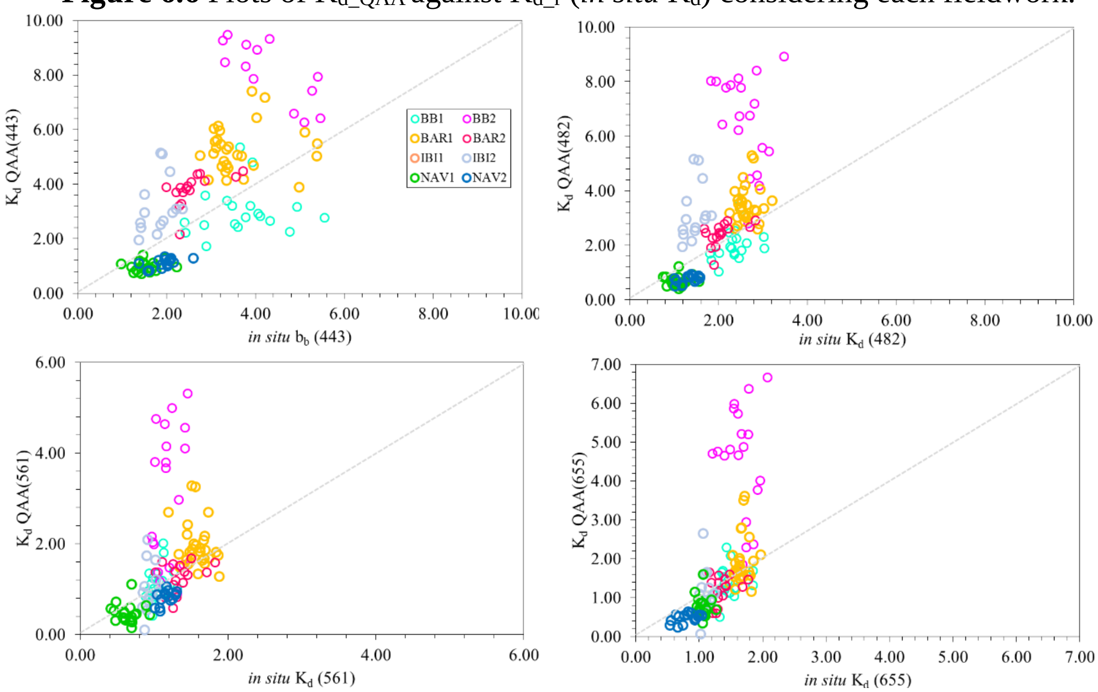

6.3.4 SPM Retrieval From OLI/LANDSAT-8 Images

The OLI images were processed to retrieve a_t and b_{bp} (removing water backscattering from b_b), and sequentially, K_d. The M4 SPM retrieval model in Table 6.3 was applied to the K_d images, given that it provided the most reliable SPM estimations at K_d(655)nm band. The SPM maps over different reservoirs are shown in Figure 6.7. Values of R_{rs}(655) varied between 0.011 - 0.018 sr^{-1} in BB2, 0.006 - 0.016 sr^{-1} in BAR1, 0.005 - 0.024 sr^{-1} in IBI1, and 0.002 - 0.010 sr^{-1} in NAV1. The a_t(655) values were ranging between 0.63-0.76 m^{-1} in BB2, 0.42 - 0.60 m^{-1} in BAR1, 0.50 - 0.70 m^{-1} in IBI1, and 0.63 - 1.12 m^{-1} in NAV1. The b_{bp} were ranging between 0.11 - 0.22 m^{-1} in BB2, 0.07 - 0.21 in BAR1, 0.05 - 0.15 in IBI1 and 0.02 - 0.22 m^{-1} in NAV1, clearly showing a downstream decreasing trend overall, i.e., sequential trapping of SPM materials through the cascades. The SPM concentrations were higher in BB2, ranging from 5.0 to 25 $mg.L^{-1}$; in BAR1 ranged from 6.3 - 15.0 $mg.L^{-1}$; and in NAV1, the range was 0.40 to 0.70 $mg.L^{-1}$. SPM estimates retrieved 28.4% of nRMSE, on average.

6.4 DISCUSSION

Regarding the QAA performances, QAA_{TRCS} provides the most accurate results, mainly for the a_t estimates. The improvement of its performance is related to the four main modifications we made to derive the QAA_{TRCS}. The first modification was adapting the method from Wang et al. (2017) to compute $\alpha(\lambda)$ and $\beta(\lambda)$ coefficients instead of using 0.52 and 1.7 values to retrieve r_{rs}. The second change was shifting λ_0 towards longer wavelengths. Integrating the Landsat 8/OLI bands and our absorption measurements (400-800 nm), we selected two wavelengths for this – 561 nm and 665 nm. Nevertheless, when we assessed the total absorption against water absorption contribution, we found that a_{t-w}(655) comply with Lee et al.(2002) requirements for choosing the reference wavelength.

Another relevant change was to identify α coefficient (see Table S.6.1) that relevantly estimate a and b_b. For this, we tested α=2 and α=5 (Lee et al., 2002; Lee et al., 2007), where they presented huge discrepancies in their errors, reaching almost 20% in some wavelengths (results of our tests not shown in this paper). In regard to the performances, we used α=2 for reservoirs with higher CDOM contributions and lowest turbidity (BAR2 and IBI2) and; α=5 for the reservoirs with high influence of Chl-a and highest turbidity levels. The final change was to modify the bands for compunting the η parameter, since two reservoirs (BAR and IBI) presented a high contribution of CDOM into the absorption conditions (Figure 3.4). We used 561/655 band ratio to account for the CDOM effects (Ogashawara et al., 2017). Among all tested bands, the 561/655 band ratio also provided the best correlation with SPM concentrations for TRCS's dataset (r= 0.65).

Figure 6.7 OLI images to retrieve R_{rs}, a_t, b_{bp} and SPM concentration in BB (10/13/14), BAR (08/15/2016) and NAV (05/02/2014) reservoirs in first, second and third line, respectively.

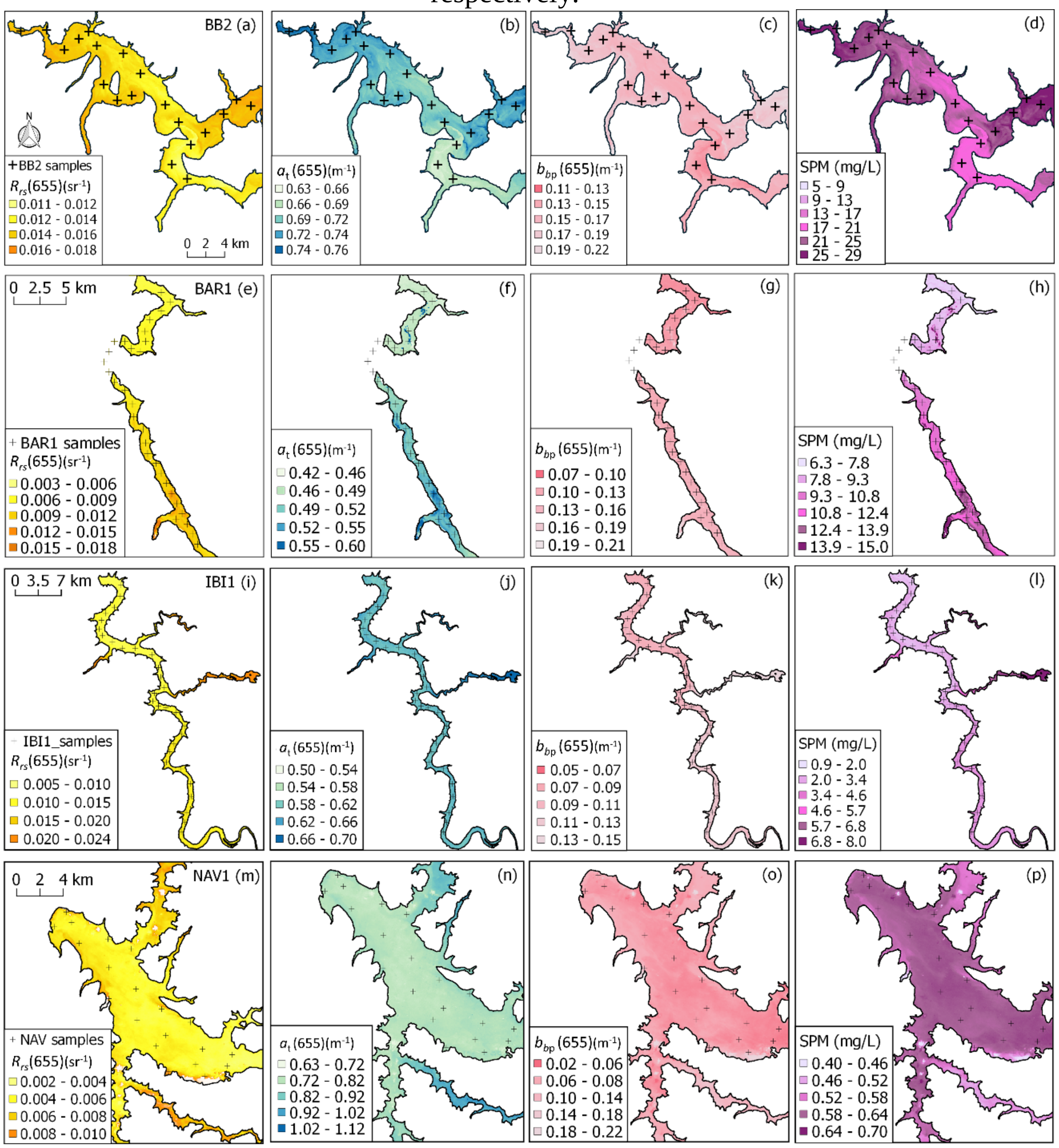

As a result of these changes, the QAA_{TRCS} improved almost 14% in a_t estimates compared to QAA_{OMW} and 30% in b_b estimates when compared with QAA_{V5} that retrieved the worst results. The main reason for the poor performance of a_t estimates in BB2 (Table S.6.2) is related to the high levels of Chl-*a* in BB2. Comparing the results with eutrophic aquatic systems by Watanabe et al (2016) and Mishra et al (2014), the poorest performance is likely to be caused by the λ_0, since OLI did not have the 709 nm (or near) band to be used as reference wavelength.

Regarding to the backscattering, the estimated values agreed with in situ b_b, except in BB1. The backscattering measurements in BB1 and NAV1 were conducted with HydroScat-6P (HOBI-labs Inc.2008), which was developed for ocean waters (Wu et al., 2011). Therefore, when the sensor is used in turbid water with high scattering and absorption properties, the measurements are subject to errors related to the signal losses of path length and saturation (Carvalho et al., 2015). BB1 is more complex than NAV1, which can produce non-stable measurements due to limitations of the equipment that did not occur in NAV1 that is considered as a less complex water environment (Leymarie et al., 2010; Carvalho et al., 2015). Furthermore, eventual errors in BB1 can be related to the post-processing, which consist in corrections of power losses due to the sensor's path length, also called as the Sigma correction. Even when processed accordingly to the manufacturer's instructions, it can imply in undesired variations within the blue-green spectral range in the case where environmental conditions did not meet the HydroScat specifications (Wu et al., 2013).

It is important to highlight that QAA_{OMW} also presented good performances for b_b estimates within considered individual field campaigns, mainly for non-turbid waters (Turbidity < 6 NTU). Differences in MAPE of the b_b estimates between QAA_{OMW} and QAA_{TRCS} in non-turbid waters ranged between 5.9% (IBI2) to 16.6% (NAV2). A possible source of this difference could be the band ratio used to compute η. Rodrigues et al. (2018) used 655/754 nm, which are the bands not available bands in OLI. We tested all band combinations to provide η values close to the ones retrieved from QAA_{OMW}, and the best result was achieved with 561/655 nm. Despite these differences, the magnitude of estimated b_b via QAA_{TRCS} did not affect the final K_d estimates (unlike the case for the a_t estimates) since η values are mostly influential over shorter wavelengths (Yang et al., 2013).

Overall, QAA_{CDOM} and QAA_{TRCS} also presented similar performances for a_t and b_b estimates. Such results confirmed that the inclusion of 561 nm was important in improving the QAA performance. Additionally, computing r_{rs} using spectral coefficients instead of fixed values, and using an interchangeable value of α also contributed on improving the IOPs estimates.

Outputs of QAA_{TRCS} were used in the K_d equation (Equation 6.1). The model published by Lee et al. (2013) derives K_d from IOPs and is considered a semi-analytical model which provides reliable estimates for inland waters according to Gomes et al.(2018). Comparing between K_{d_QAA} and K_{d_ref} resulting in errors lower than 25% for entire TRCS's dataset, with the minimum at 561 nm (19.2%). Poorest performances were found in BB2, BAR1 and BAR2, that can be a result of complexity of water types – the presence of meaningful concentrations of OACs differently impacts the light attenuation and, consequently produced higher values of K_d that were not considered by Lee et al. (2013). This was clearer when we observed the higher errors in shorter wavelengths for BB2, BAR1 and BAR2 that indicates an additional effect of CDOM absorption into K_d.

The highest modeled K_d value reached 8.5 m^{-1}, whilst the highest measured value was 11.9 m^{-1}, which is almost 30% less than the maximum reference value. The same error, about 30%, was found for the minimum value of K_d. Overall, the average error about 21% is a satisfactory result (Table 6.6). Observing the K_d plot in Figure 6.5 the values of K_d are directly related to SPM concentration that decreases from upstream to downstream, with isolated peaks of SPM that implies in K_d peaks. Higher values of $K_d(443)$ and $K_d(482)$ also confirmed that absorption from CDOM and phytoplankton in shorter wavelengths highly contributes to the K_d values. Other observable trend in Figure 6.5 is that K_d estimates are spectral dependent since K_d in longer wavelengths are more precise than in shorter wavelengths, confirming the errors shown in Table 6.6.

Once 655 nm was determined as wavelength, we used this band in Landsat 8/OLI to estimate a_t, b_b, K_d and then finally to derive SPM concentrations (Figure 6.7). $R_{rs}(655)$ values were higher in the BB2 image, whilst the values were the lowest in NAV. Considering that all images used in this study were atmospherically corrected provide the LASRC (Zanter, 2018), we conclude that the variance observed in each image is resulted from the widely varying of OACs.

In the BB, although is an accumulation reservoir, distribution of SPM is rather homogeneous and a typical decreasing pattern of SPM concentration downstream (Conde et al. 2019) is not observed. We consider that at this time the dam was in operation releasing water because October is in the middle of wet season. The SPM map of NAV collected in May, which is close to the peak of the hydrograph also did not show any longitudinal trend. In contrast, a clear longitudinal pattern of decreasing SPM toward the dam is detected in the BAR. Although this is a run-or-river dam, since the image was acquired during the dry season (August), the reservoir seems to be storing water and thus temporally trapping sediment. The same logic is applied in IBI that demonstrate a decreasing gradient towards the dam. It is important to highlight that BAR and IBI have lowest residence time when compared to BAR and NAV reservoirs, which also can caused differences in SPM gradients.

The tributaries of each reservoir presented higher SPM concentrations than the main channel of reservoirs located at the Tietê River, which indicates the SPM contribution from tributaries of Tietê. It is noteworthy that OLI images we used to estimate SPM were acquired on the same day (or near) with our field campaigns and thus it enabled direct validation of SPM estimates. Now that we have field validated semi-analytical model, it should be important to reconstruct a time series SPM map for continuous monitoring of SPM dynamics and to build standards of SPM concentrations in the entire cascade using K_d as the predict parameter.

6.5 CONCLUSIONS

SPM directs impact the biological aquatic process due to several effects, such as adsorbing contaminants, increasing the temperature by absorbing heat, and affecting the penetrability of light within the water column. Regarding to the light attenuation caused by SPM within the water, we observed throughout our experiments that K_d, that represented the light attenuation, was a suitable single explanatory variable to estimate SPM concentrations for inland waters. In respect to the complexity of such systems, take into account the OACs variation is an important issue to accurately develop the optical modeling, mainly when we use analytical models to derive IOPs, which are described as a function of OAC’s concentration. In respect to the most applicable analytical model, QAA, we tried to perform adjustments in order to make it suitable for OLI sensor for being applicable in a widely range of OACs concentrations.

Our changes in QAA consists in use an interchangeable parameter for CDOM environment, as well as, adapt the spectral methodology to compute r_{rs} instead of using fixed values as the original propose in Lee et al. (2002). The main reason to use spectral coefficients for computing r_{rs} is its spectral dependence. Another relevant modification was included a specific band to incorporate and mitigate the CDOM absorption effect, mainly for brownish waters as BAR and IBI reservoirs located at TRCS. The adoption of 561 nm band retrieved the lowest errors in all tested versions of QAA.

The re-parameterization and changes provided our model, named as $QAA_{TRCS,}$ which was capable to improve the IOPs estimates, yielding better accuracies for a_t, b_b and consequently K_d estimates. K_d was responsible to describe more than 74% of SPM variation within the widely range of SPM concentrations in TRCS. Then, the predictive SPM values were retrieved by using $K_d(655)$ and a power fitting, capable to provide estimates with errors lower than 30%.

Changes that were made in bands of some parameters made by and spectral optimization also implied in some constraints. One of them was that OLI bands did not show enough sensitive to estimate a_t in more eutrophic environments, however, the relative error did not affects the SPM concentration estimates by K_d. The 655 nm band was the most suitable band of OLI sensor, but the requirement of non-water total absorption dominates at was valid only for 70% of TRCS's dataset. The possibility of use other sensors can improve the SPM estimates when SPM > 30 $mg.L^{-1}$ - the highest SPM estimation using QAA_{TRCS}.

Throughout the cascade, K_d demonstrated a decrease gradient from upstream to downstream, which followed the same standard of SPM variation. In addition, the highest values of $K_d(443)$ confirmed that CDOM and phytoplankton absorption are markedly representative in K_d values. Relied on our estimates, SPM is homogeneous in the downstream reservoir, while in the intermediary reservoirs in TRCS presented a significant gradient towards to the dams.

In conclusion, QAA_{TRCS} was capable to derive K_d in inorganic, organic and CDOM dominated aquatic systems and provides reliable SPM estimates for the entire TRCS. Further investigations are needed to assess the suitability of using a sensor that has available a 700-

nm band and adequate spatial resolution to capture moderate to high SPM concentrations. Once the model was validated using synchronous in situ measurements, temporal series should be investigated to identify the existence of SPM standards and respectively driving factors.

6.6 SUPPLEMENTARY FILES

Figure S.6.1. Values of absorptions from water (a_w –black dotted line) and total non-water (a_{tnw}) at 561 nm (a) and 655 nm(b).

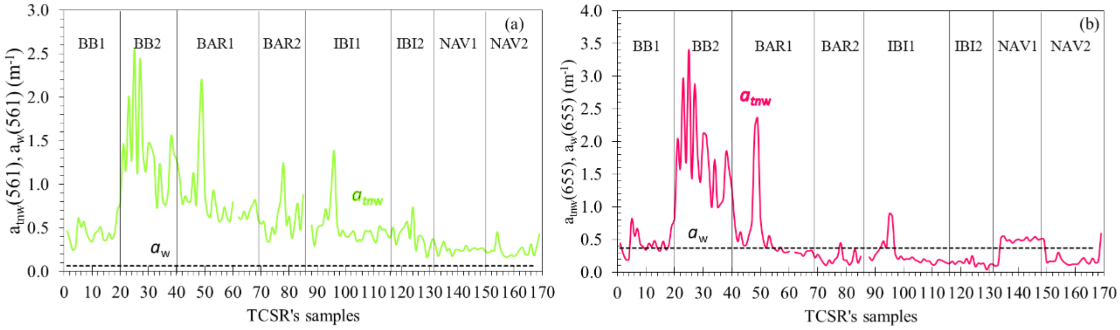

Table S.6.1. QAA enhancements in empirical steps for TRCS dataset (QAA$_{TRCS}$) based on original frame (v5, Lee et al.2002). Coefficients $\alpha(\lambda)$ and $\beta(\lambda)$ were computed using Equations from Wang et al. (2017)

Step	Parameter	Equation	V5	TRCS
0	r_{rs}	$= \dfrac{R_{rs}(\lambda)}{T + \gamma Q R_{rs}(\lambda)}$	T = 0.52 γQ = 1.7	$= \dfrac{R_{rs}(\lambda)}{\alpha(\lambda) + \beta(\lambda) R_{rs}(\lambda)}$
1	$u(\lambda)$	$= \dfrac{b_b(\lambda)}{b_b(\lambda) + a(\lambda)}$ $= \dfrac{g_0 + \sqrt{{g_0}^2 + 4 \times g_0 \times g_1 \times r_{rs(\lambda)}}}{2 \times g_1}$	g_0 = 0.089 g_1 = 0.125	-
2	χ	$= \log_{10}\left(\dfrac{r_{rs}(\lambda_1 = 443) + r_{rs}(\lambda_2 = 490)}{r_{rs}(\lambda_0) + \alpha \times \dfrac{r_{rs}(\lambda_3 = 667)^2}{r_{rs}(\lambda_4 = 490)}}\right)$	$\alpha = 5$ $\lambda_1 = 443$ $\lambda_2 = 490$ $\lambda_3 = 667$ $\lambda_4 = 490$	α = 2 or 5 $\lambda_1 = 443$ $\lambda_2 = 561$ $\lambda_3 = 561$ $\lambda_4 = 482$
3	$a(\lambda_0)$ where λ_0 = 55x, 560 or higher	$= a_w(\lambda_0) + 10^{h_0 + h_1 \times \chi + h_2 \times \chi^2}$	λ_0=55x/560 h_0 = -1.146 h_1 = -1.366 h_2 = -0.469	λ_0 = 655
4	$b_{bp}(\lambda_0)$	$= \dfrac{u(\lambda_0) \times a(\lambda_0)}{1 - \times u(\lambda_0)} - b_{bw}(\lambda_0)$	-	-
5	Υ	$= y_0 \times \left(1 - y_1 \times \exp\left(y_2 \dfrac{r_{rs}(\lambda_5 = 443)}{r_{rs}(\lambda_0)}\right)\right)$	$y_0 = 2.0$ $y_1 = 1.2$ y_2 = -0.9 $443/\lambda_0$	$y_0 = 2.0$ $y_1 = 1.2$ y_2 = -0.9 $561/\lambda_0$
6	$b_{bp}(\lambda)$	$= b_{bp}(\lambda_0) \times \left(\dfrac{\lambda_0}{\lambda}\right)^{\Upsilon}$	-	-
7	$a(\lambda)$	$= \dfrac{(C_1 - u(\lambda)) \times (b_{bp}(\lambda))}{u(\lambda)}$	C_1= 1	C_1= 1

Table S.6.2. Average **δ** (Bias, m^{-1}), RMSE (m^{-1}), nRMSE (%), and MAPE (%) among all assessed QAAs for a_t and b_{bp} retrieved from each **field campaign.**

Parameter	**δ**	**nRMSE**				**MAPE**				
a	**TRCS (n =174)**		**BB1**	**BB2**	**BAR1**	**BAR2**	**IBI1**	**IBI2**	**NAV1**	**NAV2**
	δ	**nRSME**	***n*=20**	***n*=20**	***n*=30**	***n*=18**	***n*=30**	***n*=16**	***n*=20**	***n*=20**
Lv5	-0.67	18.8	29.6	63.4	45.2	47.3	31.8	69.0	34.6	32.8
BBHR	-0.67	20.8	37.6	77.9	53.6	38.2	23.9	39.7	11.1	17.1
OMW	-0.75	21.8	41.6	79.1	58.1	50.0	26.7	42.4	25.1	28.2
CDOM	-0.32	17.7	**22.5**	68.4	44.4	36.9	21.3	38.3	8.0	17.6
V	-0.60	20.4	22.8	71.8	**39.0**	36.8	67.4	36.2	10.3	**16.9**
TRCS	-0.39	**16.8**	23.7	**62.8**	39.5	**36.1**	**20.5**	**36.2**	**7.2**	19.3
b_{bp}	**δ**	**nRMSE**				**MAPE**				
Lv5	-0.06	18.94	82.3	37.3	40.7	74.0	86.1	93.3	106.7	237.0
BBHR	-0.08	19.82	88.9	55.5	36.8	25.6	26.9	37.4	31.7	85.2
OMW	-0.08	19.70	87.9	59.1	34.7	**14.8**	**14.5**	**14.7**	**21.5**	**67.6**
CDOM	-0.06	18.83	84.8	40.2	30.3	33.4	33.8	36.4	39.0	98.2
V	-0.04	19.50	**84.4**	47.2	40.0	66.8	122.7	73.8	40.8	94.5
TRCS	-0.06	**18.70**	84.7	**39.2**	**26.3**	22.9	23.5	20.6	29.0	84.2

CHAPTER 7: FINAL CONCLUSIONS AND RECOMMENDATIONS

7.1 CONCLUSION

Understanding light interactions with OACs are essential to provide suitable bio-optical models. In the chapter 3, we evaluated the absorption properties in TRCS and identified that the gradients of OACs from up-to-downstream directly affected the absorption properties along the cascade. Water quality parameters revealed the existence of a Chl-a gradient from up-to-downstream. The opposite gradient was found for Z_{SD}, which was lower in upstream reservoirs (BB2 reaches 0.37 m) and higher in the downstream reservoirs (NAV reaches Z_{SD} = 4.80 m).

Furthermore, it was observed that organic fraction of SPM dominated the upstream reservoirs, while inorganic fractions dominated the downstream reservoir, represented by NAV. Other relevant conclusion was that reservoirs with expressive Chl-a concentration also presented high levels of phytoplankton absorption. We also evaluated an intense irradiance into the water during the fieldwork with higher Chl-a concentration, which can corroborate to phytoplankton development in BB. It was observed a widely variation between the fields conducted in BAR1 and BAR2; and IBI1 and IBI2 mainly in terms of Chl-a concentration.

Other important conclusion was some outstanding concentrations encountered in samples taken near tributaries, which also indicates some local discharges of nutrients, such as the samples located at the Ribeirão Grande River and The Jacaré-Guaçu/Claro Rivers. Regarding to phytoplankton assemblage, the variability of features observed in samples from different reservoirs indicate species richness the of phytoplankton community along the cascade.

The total absorption along the cascade is dominated by phytoplankton contributions in BB; by CDOM in BAR and IBI, and by NAP in NAV (considering the average). Considering our results, it is possible to highlight a challenge to derive a unique bio-optical model capable to retrieve OACs for the entire cascade. Nevertheless, our work also presented some dominance of phytoplankton absorption over the total absorption. Longer time series can provide more information about absorption coefficients and can also identify some predominant factors of absorption coefficients.

Once absorption properties were investigated, the quality of R_{rs} calculations was also investigated. In situ, the measurements allowed to compute R_{rs} using four different methods and the validation was conducted using transfer radiative simulation through Hydrolight and matching our results with satellite images from OLI. All methodologies considered the ρ factor as a key parameter to retrieve more accurate values of R_{rs}. Although the simplest methodology considered a fixed value, this is not totally applicable to our dataset, mainly due to wind speed conditions in some samples (ws > 5 $m.s^{-1}$). Considering all tested methods, the best R_{rs} methodology was the one provided by Lee et al., 2010, that considered a spectral value to remove glint.

Furthermore, the method removes the residual glint and fitted very well in almost all optical composition. However, this method did not retrieve satisfactory results in some high Chl-a concentrations and demonstrated that is no general values of ρ in different OACs compositions. Overall, the Lee.(2010) method reduced almost 30% the errors when compared to the other tested methods. Using the R_{rs} glint removal, it was possible to establish two bio-optical modeling empirical and analytical. The empirical models were tested as a function of simple or ratio band, and it was possible to conclude that band ratio represented better the SPM variations.

Also, tests demonstrated that using the entire dataset it is better to fit a function than use just a partial dataset, it means, data from one fieldwork or from each reservoir (two from fieldwork). The use of entire dataset provided the most reliable empirical model that retrieved errors almost 50% lower than when the model is derived from a singular dataset. Moreover, the inclusion of coastal band into the green to blue ratio, increase the errors when the model was applied into OLI images, that is an indicative that atmospheric correction can be a gap when we are leading to map the SPM concentrations over the reservoirs. The empirical model was capable to estimate the most frequent data but was not capable to estimate some extreme values, which inspire the last and main chapter of our thesis - the analytical model.

Once the IOPs are stable optical properties that are directly affected by OACs composition and concentration, we investigated the use of K_d derived by IOPs from QAA as the best single explanatory variable to define a bio-optical modeling for SPM estimates. To derive IOPs from QAA, the relevant modifications were defined in order to deal with a widely range of SPM concentration and OACs composition, mainly with CDOM dominance.

Other change was made to compute a hyperspectral coefficient to derive r_{rs}, instead of use constant values. These changes imply in reducing almost 20% of errors in IOPs when compared to the in-situ dataset. The use of K_d model was responsible to describe more than 74% of SPM variations (against of 65% of band ratio empirical model) and demonstrated that Kd at 655nm was suitable to estimate SPM concentrations with errors lower than 30%.

Considering the widely variation of inorganic, organic and CDOM domination identified in Chapter 3, and based on our results when compared to other QAA's performances, we can conclude that QAA_{TRCS} was able to derive K_d, and consequently, estimate reliable SPM concentrations.

7.2 FUTURE RECOMMENDATIONS

Our findings demonstrated improvements related to the expansion of optical knowledge in linked systems as cascade of reservoirs, quality of R_{rs} calculations, the empirical model and its strengths and limitations, besides to provide a new SA model capable to estimate SPM over a widely range of OACs concentrations. However, some recommendations are also highlighted for future works.

The first recommendation is to test new sensors with similar spatial resolution and high spectral resolution, such as Sentinel-2 that has spectral bands centered at 705 nm, 740 nm and 783 nm with 20 meters at spatial resolution. It might be possible that the red-edge band used as the reference wavelength can improve the SPM estimations in more eutrophic reservoirs, as shown in Watanabe et al. (2016) that developed QAA_{BBHR} using a dataset obtained in Barra Bonita reservoir. Moreover, additional dataset considering the other two reservoirs, Promissão and Três Irmãos, will offer a more robust dataset and can be used to revalidate our model, QAA_{TRCS}.

Another relevant issue is related to the atmospheric correction methods. Besides OLI/Landsat-8 reflectance product presents a good accuracy (Pahlevan et al., 2019), it was noticed that coastal band introduced errors in SPM estimations when we applied the model II (561/(482-443)) to the image. Maybe tests related to new atmospheric correction methods, such as the presented in ACOLITE (Vanhellemont, 2019) can derive more accurately K_d values, and retrieved lowest errors of SPM.

Further studies about profile measurements of absorption and backscattering can be conducted to better understand the dynamic inside the aquatic systems. Additional challenge might be faced regarding to backscattering coefficient, that was not measured just-below the surface. The first measurement was conducted at least in 0.50 depth and some of measurements were affected by the boat instability. Hydrolight simulations can be an alternative to provide reliable optical information in the case of in situ measurement limitations.

Once the QAA_{TRCS} was validated using OLI/Landsa-8 images, it is possible to apply the model to a pre-processed time-series and identify the occurrence of SPM standards along the TRCS. In this case, it will be also possible to identify possible causes or drivers related to high levels of SPM (rainfall, temperature, flow rates, retention time, and so on).

REFERENCES

Alcântara, E.H., Curtarelli, M., Stech, J. 2016a. Estimating total suspended mater using the particle backscattering coefficient: results from Itumbiara hydroelectric reservoir (Goiás State, Brazil). **Remote Sens. Let.,** v.7, n.4, p. 397-406. https://doi.org/10.1080/2150704X.2015.1137646

Alcântara, E., Watanabe, F., Bernardo, N., Rodrigues, T.; 2016b. The variability of particle backscattering coefficient in an oligo-to-hypertrophic cascading reservoir system: implications to TSM bio-optical model development. **Model. Earth Syst. Environ** 2(84), p.1-7. https://doi.org/10.1007/s40808-016-0146-2

Alcântara, E.;Watanabe, F.; Rodrigues, T.; Bernardo, N.; Rotta, L.; Carmo, A.; Curtarelli, M.; Imai, N. 2016. Field measurements of the backscattering coefficient in a cascading reservoir system: First results from Nova Avanhandava and Barra Bonita Reservoirs (São Paulo, Brazil). **Remote Sens. Lett.** 7, 417–426. http://dx.doi.org/10.1080/2150704X.2016.1145361

Alcântara, E.; Bernardo, N.;Watanabe, F.; Rodrigues, T.; Rotta, L.; Carmo, A.; Shimabukuro, M.; Gonçalves, S.; Imai, N. 2016c. Estimating the CDOM absorption coefficient in tropical inland waters using OLI/Landsat-8 images. **Remote Sens. Lett.** 7, 661–670. https://doi.org/10.1080/2150704X.2016.1177242

Alcântara, E.; Bernardo, N.; Rodrigues, T.; Watanabe, F. 2017. Modeling the spatio-temporal dissolved organic carbon concentration in Barra Bonita reservoir using OLI/Landsat-8 images. **Model. Earth Syst. Environ.** 2017, 3(11), 1–11. https://doi.org/10.1007/s40808-017-0275-2

APHA (American Public Health Association), AWWA (American Water Works Association), WEF (Water Environmental Federation). Standard methods for the examination of water and wastewater. 20th Edition. Washington, DC, USA: APHA, AWWA, WEF, 1998.

Babin, M.; Stramski, D.; Ferrari, G.M.; Claustre, H.; Bricaud, A.; Obolensky, G.; Hoepffner, N. 2003. Variations in the light absorption coefficients of phytoplankton, nonalgal particles, and dissolved organic matter in coastal waters around Europe. **JGR: Oceans** 108.(C7), 3211. https://doi.org/10.1029/2001JC000882

Barbosa, F.A.R.; Padisak, J.; Espindola, E.L.G.; Borics, G.; Rocha, O. 1999. The cascading reservoir continuum concept (CRCC) and its application to the river Tietê-basin, São Paulo State, Brazil. **Theor. Reserv. Ecol. Appl.** 1, 425–437.

Barrella, W.; Petrere, M., Jr. 2003. Fish community alterations due to pollution and damming in Tietê and Paranapanema rivers (Brazil). **River Res. Appl.** 19, 59–76. https://doi.org/10.1002/rra.697

Barsi, J.; Lee, K.; Kvaran, G.; Markham, B.; Pedelty, J. 2014. The spectral response of the Landsat-8 operational land imager. **Remote Sens.** 6, 10232–10251. https://doi.org/10.3390/rs61010232

Bernardo, N., Alcântara, E., Rodrigues, T.,Watanabe, F., Carmo, A., Gomes, A.C.C., Andrade, C.2018. Light Absorption Budget in a Reservoir Cascade System with Widely Differing Optical Properties. **Water** 11(2), 229-252. http://dx.doi.org/10.3390/w11020229.

Bernardo, N.; Watanabe, F.; Pequeno, T.; Alcântara, E. 2017. Atmospheric correction issues for retrieving total suspended matter concentrations in inland waters using OLI/Landsat-8 image. **Adv. Space Res.** 59,2335–2348. http://dx.doi.org/10.1016/j.asr.2017.02.017.

Bernardo, N.; Alcântara, E. 2017. Comparing proximal remote sensing and orbital images to estimate the total suspended matter in inland water. **Model. Earth Syst. Environ.** 3, 1–8. https://doi.org/10.1007/s40808-017-0285-0

Bernardo, N.;Watanabe, F.; Rodrigues, T.; Alcântara, E. Evaluation of the suitability of MODIS, OLCI and OLI for mapping the distribution of total suspended matter in the Barra Bonita Reservoir (Tietê River, Brazil). **Remote Sens. Appl. Soc. Environ.** 2016, 4, 68–82. https://doi.org/10.1016/j.rsase.2016.06.002

Bernardo, N., Alcântara E., Watanabe, F., Rodrigues, T., Carmo, A., Gomes, A., Andrade, C. 2018. Glint Removal Assessment to Estimate the Remote Sensing Reflectance in Inland Waters with Widely Differing Optical Properties. **Remote Sen**. 10, 1655 - 1677. https://doi.org/10.3390/rs10101655.

Bilotta G. S; Brazier R.E. 2008. Understanding the influence of suspended solids on water quality and aquatic biota. **Water Resource**, v. 42, p. 2849–2861. https://doi.org/10.1016/j.watres.2008.03.018

Brezonik, P.L.; Olmanson, L.G.; Finlay, J.C.; Bauer, M.E. 2015. Factor affecting the measurement of CDOM by remote sensing of optically complex inland waters. **Remote Sens. Environ.** 157, 199–215. https://doi.org/10.1016/j.rse.2014.04.033

Bricaud, A.; Morel, A.; Louis, P. 1981. Absorption by dissolved organic matter of the sea (yellow substance) in the UV and visible domains. **Limnol. Oceanogr.** 26, 43–53. https://doi.org/10.4319/lo.1981.26.1.0043

Bricaud, A.; Babin, M.; Morel, A.; Claustre, H. 1995. Variability in the chlorophyll-specific absorption coefficients of natural phytoplankton: Analysis and parameterization. **JGR: Oceans** 100, 13321–13332. https://doi.org/10.1029/95JC00463

Bricaud, A.; Morel, A.; Babin, M.; Allali, K.; Claustre, H. 1998. Variations of light absorption by suspended particles with chlorophyll a concentration in oceanic (case 1) waters: Analysis and implications for bio-optical models. **JGR: Oceans** 103, 31033–31044. https://doi.org/10.1029/95JC00463

Bukata, R.P.; Jerome, J.H.; Kondratyev, A.S.; Pozdnyakov, D.V. Optical Properties and Remote Sensing of Inland and Coastal Waters; CRC Press: Boca Raton, FL, USA, 1995.

Bukata, R. P. 2013. “Retrospection and Introspection on Remote Sensing of Inland Water Quality: Like Déjà Vu All over Again.” **Journal of Great Lakes Research** 39 (Suppl.): 2–5. https://doi.org/10.1016/j.jglr.2013.04.001.

Cairo, C.T.; Barbosa, C.C.F.; Novo, E.M.L.M.; Calijuri, M.C. 2017. Spatial and seasonal variation in diffuse attenuation coefficients of downward irradiance at Ibitinga Reservoir, São Paulo, Brazil. **Hydrobiologia** 784, 265–282. https://doi.org/10.1007/s10750-016-2883-7

Campbell, G.; Phinn, S.R.; Daniel, P. 2011. The specific inherent optical properties of three subtropical and tropical water reservoirs in Queensland, Australia. **Hydrobiologia** 658, 233–252. https://doi.org/10.1007/s10750-010-0476-4

Carder, K.L.; Steward, R.G.; Harvey, G.R.; Ortner, P.B. 1989. Marine humic and fulvic acids: Their effects on remote sensing of ocean chlorophyll. **Limnol. Oceanogr**. 34, 68–81. https://doi.org/10.4319/lo.1989.34.1.0068

Carlson, R.E. Estimating Trophic State, Lake Line 2007, 25-28 (Spring).

Carvalho, L.A.S., Barbosa, C.C.F., Novo, E.M.L.M., Rudorff, C.M. 2015, Implications of scatter corrections for absorption measurements on optical closure of Amazon floodplain lakes using the Spectral Absorption and Attenuation Meter (AC-S Wetlab). **Remote Sens. Environ.** 157, 123-137. https://doi.org/10.1016/j.rse.2014.06.018.

Cetinic, I. 2018. Phytoplankton: Optical Constituents of the Ocean. Available online: http://www.oceanopticsbook.info/view/optical_constituents_of_the_ocean/_phytoplankton #searchResult1 (accessed on 5 September 2018).

Chen, Z.M., Curran, P.J., and Hanson, J.D. 1992. Derivative reflectance spectroscopy to estimate suspended sediment concentration. **Remote Sens. Environ**. 40, 67-77. http://dx.doi.org/10.1016/0034- 4257(92)90127-6

Cole, J.J.; Prairie, Y.T.; Caraco, N.F.; McDowell,W.H.; Tranvik, L.J.; Striegl, R.G.; Duarte, C.M.; Kortelainen, P.; Downing, J.A.; Middelburg, J.J.; Melack, J. 2007. Plumbing the Global Carbon Cycle: Integrating inland waters into the terrestrial carbon budget. **Ecosystems**, 10, 175–185. https://doi.org/10.1007/s10021-006-9013-8

Das, S.; Hazra, S.; Giri, S.; Das, I.; Chanda, A.; Akhand, A.; Maity, S. 2017. Light absorption characteristics of chromophoric dissolved organic matter (CDOM) in the coastal waters of northern Bay of Bengal during winter season. **Indian J. Geo Mar. Sci.**46, 884–992.

Dellamano-oliveira, M.J.; Vieira, A.A.H.; Rocha, O.; Colombo, V.; Sant’Anna, C.L. 2008. Phytoplankton taxonomic composition and temporal changes in a tropical reservoir. **Fund Appl. Limnol.** 171, 27–38. https://doi.org/10.1127/1863-9135/2008/0171-0027

Dev, P.J.; Shanmugam, P. 2014. A new theory and its application to remove the effect of surface-reflected light in above-surface radiance data from clear and turbid waters. **J. Quant. Spectrosc. Radiat. Transf.** 142, 75–92. https://doi.org/10.1016/j.jqsrt.2014.03.021

Devlin, M.J., Barry, J., Mills, D.K., Gowen, R.J., Foden, J., Sivyer, D., Tett, P. 2008. Relationships between suspended particulate material, light attenuation and Secchi depth ini UK marine waters. **Est. Coast. Shelf Sci.** 79(3), 429-239. https://doi.org/10.1016/j.ecss.2008.04.024.

Devlin, M.J., Barry, J., Mills, D.K., Gowen, R.J., Foden, J., Sivyer, D., Greenwood, N., Pearce, D., Tett, P. 2009. Estimating the diffuse attenuation coefficient from optically active components in UK marine waters. **Est. Coast Shelf. Sic.** 82(1), 73-83. https:// doi:10.1016/j.ecss.2008.12.015

Doxaran, D.; Froidefone, J.; Castaing, P. 2002. A reflectance band ratio used to estimate suspended matter concentrations in sediment-dominated coastal waters. **Int. J. Remote Sens.** 23, 5079–5085. https://doi.org/10.1080/0143116021000009912

Doxaran, D., Froidefond, J.M., Lavender, S., and Castaing, P. 2002b. Spectral signature of highly turbid waters Application with SPOT data to quantify suspended particulate matter concentrations. **Remote Sens. Environ.** 81, 149-161. http://dx.doi.org/10.1016/S0034 - 4257(01)00341-8

Doxaran D, Froidefond J.M., Castaing P. 2003. Remote-sensing refectance of turbid sediment dominated waters. Reduction of sediment type variations and changing illumination conditions efects by use of refectance ratios. **Appl Opt** 42:2623–2634. https://doi.org/10.1364/AO.42.002623

Edward, T. K., Glysson, G.D., Guy, H.P., Norman, V.W. 2019. Field Methods for Measurement of Fluvial Sediment. Available online: https://pubs.er.usgs.gov/publication/ofr86531 (accessed on 29 September 2018).

Estapa, M.L.; Boss, E.; Mayer, L.M.; Roesler, C.S. 2012. Role of iron and organic carbon in mass-specific light absorption by particulate matter from Louisiana coastal waters. **Limnol. Oceanogr**, 57, 97–112. https://doi.org/10.4319/lo.2012.57.1.0097

Ferreira, A.; Ciotti, A.M.; Giannini, M.F.C. Variability in the light absorption coefficients of phytoplankton, non-algae particles, and colored dissolved organic matter in a subtropical bay (Brazil). **Estuar. Coast. Shelf Sci.** 2014, 139, 127–136. https://doi.org/10.1016/j.ecss.2014.01.002

Frascareli, D.; Cardoso-Silva, S.; Mizael, J.D.; Rosa, A.H.; Pompeo, M.L.M.; Doval, J.C.L.; Moschini, C.V. 2018. Spatial distribution, bioavailability, and toxicity of metals in surface sediments of tropical reservoirs, Brazil**. Environ. Monit. Assess** 190, 199. https://doi.org/ 10.1007/s10661-018-6515-8.

Fougnie, B.; Frouin, R.; Lecomte, P.; Deschamps, P.-Y. 1999. Reduction of skylight reflection effects in the above water measurement of diffuse marine reflectance. **Appl. Opt.** 38, 3844–3856. https://doi.org/10.1364/AO.38.003844

Garaba, S.P.; VoB, D.; Wollschlager, J.; Zielinski, O. 2015. Modern approaches to shipborne ocean color remote sensing. **Appl. Opt.** 54, 3602–3613. https://doi.org/10.1364/AO.54.003602

Garaba, S.P.; Zielinski, O. 2013. Comparison of remote sensing reflectance from above-water and in-water measurements west of Greenland, Labrador Sea, Denmark Strait and west of Iceland. **Appl. Opt.** 21, 15938–15950. . https://doi.org/10.1364/OE.21.015938.

Garaba, S.P.; Zielinski, O. Methods in reducing surface reflected glint for shipborne above-water remote sensing. **J. Eur. Opt. Soc. Rapid Publ.** 2013, 8. https://doi.org/10.2971/jeos.2013.13058.

Gernez, P., Barillé, L., Lerouxel, A., Mazeran, C., Lucas, A., Doxaran, D. 2014. Remote sensing of suspended particulate matter in turbid oyster-farming ecosystem. **JGR Oceans** 119, 7277-7294. https://doi.org/10.1002/2014JC010055.

Gilerson, A.; Carrizo, C.; Foster, R.; Harmel, T. Variability of the reflectance coefficient of skylight from the ocean surface and its implications to ocean color. **Opt. Exp.** 2018, 26, 9615–9633.

Golterman, H.L. Developments in water science 2. Physiological limnology: an approach to the physiology of lake ecosystems. Amsterdam, Netherlands: Elsevier, 1975.

Gomes, A. C. C.; Bernardo, N. M. R.; Alcântara, E. 2017. Accessing vegetation health in a drought and land use and land cover changing scenario. **Natural Hazards.** 89,1401-1420.

Giardino, C., Brando, V.E., Gege, P., Pinnel, N., Hochberg, E., Knaeps, E., Reusen, I., Doerffer, R., Bresciani, M., Braga, F., Foerster, S., Champollion, N., Dekker, A. 2018. Imaging spectrometry of inland and coastal waters: state of the art, achievements and perspectives. Surveys in Geophysics 1-29. doi: 10.1007/s10712-018-9476-0.

Giardino C, Bresciani M, Braga F, Cazzaniga I, De Keukelaere L, Knaeps E, Brando VE 2017. Biooptical modeling of total suspended solids. In: Mishra DR, Ogashawara I (eds) Bio-optical modeling and remote sensing of inland waters. Elsevier, Amsterdam,129–156.

Gokul, E.A.; Palanisamy, S.; Sundarabalan, B.; Sahay, A.; Chauhan, P. 2014.ç Modelling the inherent optical properties and estimating the constituents' concentrations in turbid and eutrophic waters. **Cont. Shelf Res.** 84, 120–138. https://doi.org/10.1016/j.csr.2014.05.013

Golterman, H.L. Developments in Water Science 2. Physiological Limnology: An Approach to the Physiology of Lake Ecosystems; Elsevier: Amsterdam, The Netherlands, 1975.

Gordon, H.R.; Brown, O.B.; Jacobs, M.M. 1975. Computed relationships between the inherent and apparent optical properties of a flat, homogenous ocean. **Appl. Opt.** 14, 417–427. https://doi.org/10.1364/AO.14.000417

Gordon, H. R., Brown, O. B., Evans, R. H., Brown, J. W., Smith, R. C., Baker, K. S., Clark, D. K. 1988. A semianalytic radiance model of ocean color. J. Geophys. Res. 93, 10909–10924. https://doi.org/10.1364/0148-0227/88/008 D-0129505.00

Han, L.H., Rundquist, D.C., Liu, L.L., Fraser, R.N., and Schalles, J.F. 1994. The spectral responses of algal chlorophyll in water with varying levels of suspended sediment. Int. J. Remote Sens., 15, 3707-3718. http://dx.doi.org/10.1080/01431169408954353.

Han, B., Loisel, H., Vantrepotte, V., Mériaxu, X., Bryère, P., Ouillon, S., Dessaily, D., Xing, Q., Zhu, J. 2016. Development of a Semi-Analytical Algorithm for the Retrieval of Suspended Particulate Matter from Remote Sensing over Clear to Very Turbid Waters. **Remote Sens.** 8, 211. http://dx.doi.org/10.3390/rs8030211.

Hansen, C.H. Google Earth Engine as a Platform for Making Remote Sensing of Water Resources a Reality for Monitoring Inland Waters. Available online: https://www.researchgate.net/profile/Carly_Hansen/ publication/277021226_Google_Earth_Engine_as_a_Platform_for_Making_Remote_Sensing_of_Water_ Resources_a_Reality_for_Monitoring_Inland_Waters/links/555f8c2a08ae9963a118b3e2.pdf (accessed on 18 March 2019).

Harvey, E T., Walve, J., Andersson, A., Karlson, B., Kratzer, S. 2018. The Effect of Optical Properties on Secchi Depth and Implications for Eutrophication Management. **Front. Mar. Sci.** 5, 1-19. https://doi.org/10.3389/fmars.2018.00496.

Helms, J.R.; Stubbins, A.; Ritchie, J.D.; Minor, E.C.; Kieber, D.J.; Mopper, K. 2008. Absorption spectral slopes and slope ratios as indicators of molecular weight, source, and photobleaching of chromophoric dissolved organic matter. **Limnol. Oceanogr**, 53, 955–969. https://doi.org/10.4319/lo.2008.53.3.0955.

HOBILabs - HYDRO-OPTICS, BIOLOGY e INSTRUMENTATION LABORATORIES. HydroScat-6P - Spectral backscattering sensor and fluorometer: user’s manual (revision j). 67 p., 2010. Available at: <http://www.hobilabs.com/cmsitems/attachments/3/HS6ManualRevJ-2010-8a.pdf>. Access in: Janeiro 2018.

Hooker, S.B.; Lazin, G.; Zibordi, G.; McLean, S. 2002. An evaluation of above- and in-water methods for determining water leaving radiances. **J. Atmos. Ocean. Technol**. 19, 486–515. https://doi.org/10.4319/lo.2008.53.3.0955. https://doi.org/10.1175/1520-0426(2002)019<0486:AEOAAI>2.0.CO;2

Højerslev, N.K. 2001. Analytic remote-sensing optical algorithms requiring simple and practical field parameter inputs. **Appl. Opt.** 40, 4870–4874. https://doi.org/10.1364/AO.40.004870.

Imai, N.N., Shimabukuro, M.H., Carmo, A.F.C., Alcântara, E.H., Rodrigues, T.W.P., Watanabe, F. 2015 .Bio-optical data integration based on a 4D database system approach. In: The International Archives of Photogrammetry, Remote Sensing and Spatial Information Sciences, Volume XL-7/W3, 2015. 36th International Symposium on Remote Sensing of Environment, 11–15 May 2015, Berlin, Germany.

IOCCG. Remote sensing of inherent optical properties: Fundamentals, tests of algortihms and applications. Reports of the international ocean-colour coordinating group. Dartmouth, Canada:IOCCG, 2006.

IOCCG. Atmospheric Correction for Remotely-Sensed Ocean-Colour Products, Reports of the International Ocean-Colour Coordinating Group; Report Number 10; IOCCG: Busan, Korea, 2010.

Joshi,D. I. and D'sa, E. 2018. An estuarine-tuned quasi-analytical algorithm (QAA-V): assessment and application to satellite estimates of SPM in Galveston Bay following Hurricane Harvey. **Biogeosciences** 15, 4065-4086. https://doi.org/10.5194/bg-15-4065-2018.

Kay, S.; Hedley, J.D.; Lavender, S. 2009Sun glint correction of high and low spatial resolution images of aquatic scenes: A review of methods for visible and near-infrared wavelengths. **Remote Sens.** 1, 697–730. https://doi.org/10.3390/rs1040697

Khan, M.F., Maulud, K.N.A., Latif, M.T., Chung, J.X., Amil, N., Alias, A., Nadzir, M.S.M., Sahani, M., Mohammad, M., Jahaya, M.F., Hassan, H. 2018. Physicochemical factors and their potential sources inferred from longterm rainfall measurements at an urban and a remote rural site in tropical areas. **Sci Total Environ** 613:1401–1416. https://doi.org/10.1016/j.scitotenv.2017.08.025

Kirk, J. Light and Photosysnthesis in Aquactic Ecosystems, 2nd ed.; Cambridge University Press: Cambridge, UK, 1994.

Kirk, J.T.O. 2011. Light and photosynthesis in aquatic ecosystems, 3rd ed. Cambridge University Press, New York.

Kong, J., Shan, Z., Chen, Y., Yang, J., Hu, Y., & Wang, L. 2018. Assessment of remote-sensing retrieval models for suspended sediment concentration in the Gulf of Bohai. Inte. J. Remote Sensing, 1–19.doi:10.1080/01431161.2018.148202

Kruse, F.A.; Lefkoff, A.B.; Dietz, J.B. 1993. Expert System-Based Mineral Mapping in Northern Death Valley,California/Nevada, Using the Airbone Visible/Infrared Imaging Spectrometer (AVIRIS). **Remote Sens. Environ.** 44, 309–336. https://doi.org/10.1016/0034-4257(93)90024-R

Kuhn, C., de Matos Valerio, A., Ward, N., Loken, L., Sawakuchi, H. O., Kampel, M., Butman, D. 2019. Performance of Landsat-8 and Sentinel-2 surface reflectance products for river remote sensing retrievals of chlorophyll-a and turbidity. **Remote Sens.Environ**., 224, 104–118. doi:10.1016/j.rse.2019.01.023.

Kutser, T.; Pierson, D.C.; Kallio, K.Y.; Reinart, A.; Sobek, S. 2005. Mapping lake CDOM by satellite remote sensing. **Remote Sens. Environ.** 94, 535–540. https://doi.org/10.1016/j.rse.2004.11.009

Kutser, T.; Vahtmae, E.; Paavel, B.; Kauer, T. 2013. Removing glint effects from field radiometry data measured in optically complex coastal and inland waters. **Remote Sens. Environ.** 133, 85–89. https://doi.org/10.1016/j.rse.2013.02.011

Kutser, T.; Paavel, B.; Verpoorter, C.; Ligi, M.; Soomets, T.; Toming, K.; Casal, G. 2016. Remote sensing of Black Lakes and using 810 nm reflectances peak for retrieving water quality parameters of optically complex waters. **Remote Sens.**, 8, 497. https://doi.org/10.3390/rs8060497

Kutser, T.; Vahtmäe, E.; Praks, J. 2009. A sun glint correction method for hyperspectral imagery containing areas with non-negligible water leaving NIR signal. **Remote Sens. Environ.** 113, 2267–2274. https://doi.org/10.1016/j.rse.2009.06.016

Lambert, T.; Teodoru, C.R.; Nyoni, F.C.; Bouillon, S.; Darchambeau, F.; Massicotte, P.; Borges, A.V. 2016. Along-stream transport and transformation of dissolved organic matter in a large tropical river. **Biogeosciences** 13(9) 2727–2741. https://doi.org/10.5194/bg-13-2727-2016

Le, C.F., Li, Y.M., Zha, Y., Sun, D., Yin, B. 2009. Validation of quasi-analytical algorithm for highly turbid eutrophic water of Meiliang Bay in Taihu Lake, China. **IEE Trans. Geosc.** Remote Sens. 47(8), 2492-2500. https://doi.org/10.1109/TGRS.2009.2015658

Lee Z-P., Carder K.L., Arnone R.A., 2002 Deriving inherent optical properties from water color: a multiband quasi-analytical algorithm for optically deep waters. **Appl Opt** 41:5755–5772. https://doi.org/10.1364/AO.41.005755

Lee, Z.;Weidemann, A.; Kindle, J.; Arnone, R.; Carder, K.L.; Davis, C. 2007. Euphotic zone depth: Its derivation and implication to ocean-color remote sensing. **JGR: Oceanas** 112, C03009. https://doi.org/10.1029/2006JC003802.

Lee, Z.; Lubac, B.; Werdell, J.; Arnone, R. An Update of the Quasi-Analytical Algorithm (QAA_v5) [WWW

Document]. 2009. Available online:
http://www.ioccg.org/groups/Software_OCA/QAA_v5.pdf (accessed
on 12 August 2018).

Lee, Z.; Ahn, Y.; Mobley, C.; Arnone, R. 2010. Removal of surface-reflected light for the measurements of remote-sensing reflectance from an above-surface platform. **Opt. Exp.** 18, 26313–26324. https://doi.org/10.1364/OE.18.026313

Lee, Z.; Pahvelan, N.; Ahn, Y.; Greb, S.; O'Donnell, D. 2013. Robust approach to directly measuring water-leaving radiance in the field. **Appl. Opt.** 52, 1693–1701. https://doi.org/10.1364/AO.52.001693

Lee, Z., Hu, C., Shang, S., Du, K., Lewis, M., Arnone, R., Brewin, R.. 2013b. Penetration of UVvisible solar radiation in the global oceans: insights from ocean color remote sensing. **JGR: Oceans** 118:4241–4255. http://dx.doi.org/10.1002/jgrc.20308.

Lee, Z., Shang, S., Qi, L., Lin, G. 2016. A semi-analytical scheme to estimate Secchi-disk depth from Landsat-8 measurements. **Remote Sens. Environ.** 177, 101-106. https://doi.org/10.1016/j.rse.2016.02.033.

Lee Z., Shang, S., Stavn, R. 2018. AOPs are not additive: on the biogeo-optical modeling of the difuse attenuation coefficient. **Frontiers in Marine Science**, 5(8), https://doi.org/10.3389/fmars.2018.00008.

Lehmann, M.K.; Nguyen, U.; Allan, M.; van der Woerd, H. 2018. Colour classification of 1486 lakes across a wide range of optical water types. **Remote Sen.** 10, 1273. https://doi.org/10.3390/rs10081273

Leymarie, E., Doxaran,D., Babin, M. 2010. Uncertainties associated to measurements of inherent optical properties in natural waters. **Appl, Opt**., 49(28), 5415-5436. https://doi.org/10.1364/AO.49.005415

Li, L., Li, L., Song, K. 2014. Remote sensing of freshwater cyanobacteria: an extended IOP inversion model of inland waters (IIMIW) for partitioning absorption coefficient and estimating phycocyanin. **Remote Sens. Environ.**, v. 157, p. 9 – 23. https://doi.org/10.1016/j.rse.2014.06.009

Li, L.; Li, L.; Song, K.; Li., Y.; Tedesco, L.P.; Shi, K.; Li, Z. 2013. An inversion model for deriving optical properties validation and application. **Remote Sens. Environ** 135, 150–166. https://doi.org/10.1016/j.rse.2013.03.031

Liu, J., Liu, J., He, X., Pan, D., Zhu, F., Chen, T., Wang, Y. 2018. Diurnal dynamics and seasonal variations of total suspended particulate matter in highly turbid Hangzhou Bay waters based on Geostationaty Ocean Color Imager. **IEEE J. Sel. Top. Appl. Earth Observ. Remote Sens.**, 11(7), 2170-2180. https://doi.org/10.1109/JSTARS.2018.2830335

Lobo F.L., Costa M.P., Novo E.M. 2015. Time-series analysis of Landsat-MSS/TM/OLI images over Amazonian waters impacted by gold mining activities. **Remote Sens. Environ.** 157:170–184. https://doi.org/10.1016/j.rse.2014.04.030

Lobo, F. L., Costa, M. P. F., Phillips, S., Young, E., & McCregor, C. 2014. Light backscattering in turbid freshwater: A laboratory investigation. **J. App. Rem. Sens.** 8(1), 083611 – 083625. http://dx.doi.org/10.1117/1.JRS.8.083611.

Londe, L.R., Novo, E. M. L. M., Barbosa, C., Araujo, C. A. S. 2016. Water residence time affecting phytoplankton blooms: study case in Ibitinga Reservoir (São Paulo, Brazil) using Landsat/TM images. **Braz. J Biol.** 76(3), 664-672, http://dx.doi.org/10.1590/1519-6984.23814.

Lobo, F. L., Costa, M., Phillis, S., Young, E., McGregor, C. 2014. Light backscattering in turbid freshwater: a laboratory investigation. **J. Appl. Remote Sens.** 8(1), 083611-1 - 083611-14. https://doi.org/10.1117/1.JRS.8.083611.

Luo, Y., Doxaran, D., Ruddick, K., Shen, F., Gentili, B., Yan, L., Huang, H. 2018. Saturation of water reflectance in extremely turbid media based on field measurements, satellite data and bio-optical modelling. **Opt. Exp.** 26(8), 10435-10451. https://doi.org/10.1364/OE.26.010435.

Lymburner, L., Botha, E., Hestir, E., Anstee, J., Sagar, S., Dekker, A., Malthus, T. 2016. Landsat 8: providing continuity and increased precision for measuring multi-decadal time series of total suspended matter. **Remote Sens. Environ.** 185, 108–118. https://doi.org/10.1016/j.rse.2016.04.011.

Maritorena, S.; Siegel, D. A.; Peterson, A. R. Optimization of a semianalytical ocean color model for global-scale applications. **Appl. Opt.** 41(15), 2705–14, 2002. https://doi.org/10.1364/AO.41.002705

Martins, S.; Chokmani, K.; Alcântara, E.; Ogashawara, I.; El-Alem, A. 2018. Mapping the coloured dissolved organic matter absorption coefficient in a eutrophic reservoir using remotely sensed images. **Inland Waters** 8, 488–504. https://doi.org/10.1080/20442041.2018.1482153

Ma, J., Song., K., Wen, Z., Zhao, Y., Shang, Y., Fang, C., Du, J. 2016. Spatial distribution of diffuse attenuation of photosynthetic active radiation and its main regulating factors in inland waters of Northeast China. **Remote Sens.** 8, 964-981. http://dx.doi.org/10.3390/rs8110964.

Martinez, J-M., Espinoza-Villar, R., Armijos, E., Moreira, L.S. 2015. The optical properties of river and floodplain waters in the Amazon River Basin: Implications for satellite-based measurements of suspended particulate matter. **JGR: Earth Surface** 120, 1274-1287. http://dx.doi.org/10.1002/2014JF003404.

Massicote, P.; Asmala, E.; Stedmon, C.; Markager, S. 2017. Global distribution of dissolved organic matter alongthe aquatic continuum: Across rivers, lakes and oceans. **Sci. Total Environ.** 609, 180–191. http://dx.doi.org/10.1016/j.scitotenv.2017.07.076

Matthews, M. W. 2011. A current review of empirical procedures of remote sensing in inland and near-coastal transitional waters. **Int. J. Remote Sens.**, v. 32(21),6855–6899. https://doi.org/10.1080/01431161.2010.512947

Matthews, M.W.; Bernard, S. 2013. Characterizing the absorption properties for remote sensing of three small optically-diverse South African reservoirs. **Remote Sens**. 5, 4370–4404. http://dx.doi.org/10.3390/rs5094370

Matsuoka, A.; Hooker, S.B.; Bricaud, A.; Babin, M. 2013. Estimating absorption coefficients of colored dissolved organic matter (CDOM) using a semi-analytical algorithm for southern Beaufort Sea Waters: Application to deriving concentrations of dissolved organic carbon from space. **Biogeosciences** 10, 917–927. DOI: 10.5194/bg-10-917-2013

Meler, J.; Ostrowska, M.; Ston-Egiert, J.; Zablocka, M. 2017. Seasonal and spatial variability of light absorption by suspended particles in the southern Baltic: A mathematical description. **J. Mar. Syst**. 170, 68–87. https://doi.org/10.1016/j.jmarsys.2016.10.011

Mishra, S., Mishra, D.R., Lee, Z-P. 2014. Bio-optical inversion in highly turbid and cyanobacteria-dominated waters. **IEEE Trans. Geosc. Remote Sens.** 52(1), 375 – 388. 10.1109/TGRS.2013.2240462

Mobley, C.D. Light and Water: Radiative Transfer in Natural Water; Academic Press: San Diego, CA, USA, 1994.

Mobley, C. D. 1999. Estimation of the remote-sensing reflectance from above-surface measurements. **Appl. Opt.**, v. 38, n. 36, p. 7442-7455. https://doi.org/10.1364/AO.38.007442

Mobley, C. 2001. "Radiative Transfer in the Ocean." In Encyclopedia of Ocean Sciences, edited by J. H. Steele, 2321–2330. London: Academic Press Elsevier.

Mobley, C.D.; Sundman, L.K. HydroLight 5.2—EcoLight 5.2 Users' Guide; Sequoia Scientific, Inc.: Bellevue,WA,USA, 2013.

Mobley, C. 2015. Polarized reflectance and transmittance properties of windblown sea surfaces. **Appl. Opt.** 54, 4828–4849. https://doi.org/10.1364/AO.54.004828

Moore, T.; Dowell, M.D.; Bradt, S.; Verdu, A.R. 2014. An optical water type framework for selecting and blending retrievals from bio-optical algorithms in lake and coastal waters. **Remote Sens. Environ**. 143, 97–111. https://doi.org/10.1016/j.rse.2013.11.021

Morel, A.; Prieur, L. 1977. Analysis of variations in ocean color. **Limnol, Oceanog** 22(4), 709-722. https://doi.org/10.4319/lo.1977.22.4.0709

Morel, A. 2001. “Bio-Optical Models.” In Encyclopedia of Ocean Sciences, edited by J. H. Steele,317–326. London: Academic Press Elsevier.

Morel A, Maritorena S. 2001 Bio-optical properties of oceanic waters: a reappraisal. **J Geophys** Res 106:7163–7180. https://doi.org/10.1029/2000JC000319

Muow, C.B.; Greb, S.; Aurin, D.; DiGiacomo, P.M.; Lee, Z.; Twardowski, M.T.; Binding, C.; Hu, C.; Ma, R.; Moore, T.; et al. 2013. Aquatic color radiometry remote sensing of coastal and inland waters: Challenges and recommendations for future satellite missions. **Remote Sens. Environ.** 2013, 160, 15–30. https://doi.org/10.1016/j.rse.2015.02.001

Mueller, J.L.2000. In-water radiometric profile measurements and data analysis protocols. In Ocean Optics Protocols for Satellite Ocean Color Sensor Validation; Fargion, G.S., Mueller, J.L., Eds.; NASA Tech. Memo, Goddard Space Flight Center: Greenbelt, MD, USA, 2000; pp. 87–97.

Nechad, B., Ruddick, K.G., and Park, Y. 2010. Calibration and validation of a generic multisensory algorithm for mapping of total suspended matter in turbid waters. **Remote Sens. Environ.,** 114, 854-866. http://dx.doi.org/10.1016/j.rse.2009.11.022

Novoa, S., Doxaran, D., Ody, A., Vanhellemont, Q., Lafon, V., Lubac, B., Gernez, P. 2017. Atmospheric corrections and multi-conditional algorithm for multi-sensor remote sensing of suspended particulate matter in low-to-high turbidity levels coastal waters. **Remote Sens.** 9, 61 – 92. http://dx.doi.org/10.3390/rs9010061.

Odermatt, D.; Gitelson, A.; Brando, V.E.; Schaepman, M. 2012. Review of constituent retrieval in optically deep and complex waters from satellite imagery. **Remote Sens. Environ.**, 118, 116–126. https://doi.org/10.1016/j.rse.2011.11.013

Ogashawara, I., Mishra, D.R., Nascimento, R.F.F., Alcântara, E., Kampel, M., Stech, J.L. 2016. Re-parametrization of quasi-analytical algorithm for colored dissolved organic matter dominant inland waters. International Journal of Applied Earth and Observation and Geoinformation 53, 128-145. https://doi.org/10.1016/j.jag.2016.09.001

Palmer, S., Kutser, T., Hunter, P.D. 2015. Remote sensing of inland waters: Challenges, progress and future directions. **Remote Sens. Environ.** 175, 1-8. https://doi.org/10.1016/j.rse.2014.09.021

Pahlevan, N., Chittimalli, S.K., Balasubramanian, S.V., Vellucci, V. 2019. Sentinel-2/Landsat-8 product consistency and implications for monitoring aquatic systems. **Remote Sens. Environ.** 220, 19-29. https://doi.org/10.1016/j.rse.2018.10.027.

Pahlevan, N., Balasubramanian, S., Sarkar, S., Franz, B.A. 2018. Toward Long-Term Aquatic Science Products from Heritage Landsat Mission. **Remote Sens.** 10, 1337-1360. https://doi.org/ 10.3390/rs10091337.

Pahlevan, N.; Lee, Z.; Wei, J.; Schaaf, C.B.; Schott, J.R.; Berk, A. 2014. On-orbit radiometric characterizations of OLI (Landast-8) for applications in aquatic remote sensing. **Remote Sens. Environ.** 154, 272–284. https://doi.org/10.1016/j.rse.2014.08.001

Pahlevan, N.; Schott, J.R. Leveraging EO-1 to evaluate capability of new generation of Landsat sensors for coastal/inland water studies. **IEEE J. Sel. Top. Appl. Earth Observ. Remote Sens.** 2013, 6, 360–374. https://doi.org/10.1109/JSTARS.2012.2235174

Pahm, Q.V., Ha, N.T.T., Pahlevan, N., Oanh, L. T., Nguyen, T.B., Nguyen, N.T. 2018. Using Landsat-8 images for quantifying suspended sediment concentration in Red River (Northern Vietnam). **Remote Sen**. 10, 1841 – 1860. https://doi.org/10.3390/rs10111841.

Periotto, N.A.; Tundisi, J.G. 2018. A characterization of ecosystems services, drives and values of two watersheds in São Paulo State, Brazil. **Braz. J. Biol.** 78, 397–407. http://dx.doi.org/10.1590/1519-6984.166333

Perkins, M.G.; Effler, S.W.; Strait, C.M. 2014. Phytoplankton absorption and the chlorophyll a-specific absorption coefficient in dynamic Onondaga Lake. **Inland Waters** 4, 133–146. http://dx.doi.org/10.5268/IW-4.2.607

Pope, R. M.; Fry, E. S. 1997. Absorption spectrum (380–700 nm) of pure water. II. Integrating cavity measurements. **Appl. Opt.**, v. 36, n. 33, p. 8710-8723.

Prado, R.B.; Novo, E.M.L.M. 2015. Modeling pollution potential input from the drainage basin into Barra Bonita reservoir, São Paulo—Brazil. **Braz. J. Biol.** 2015, 75, 314–323. https://doi.org/10.1364/AO.36.008710

Prieur, L.; Sathyendranath, S. 1981. An optical classification of coastal and oceanic waters based on specific spectral absorption curves of phytoplankton pigments, dissolved organic matter, and other particulate materials. **Limnol. Oceanogr.** 1981, 26, 671–689. https://doi.org/10.4319/lo.1981.26.4.0671

Richardson, L.L. 1996. Remote sensing of algal bloom dynamics: A new research fuses remote sensing of aquatic ecosystems with algal accessory pigment analysis. **Bioscience** 46(7), 492–501. https://doi.org/10.2307/1312927

Riddick, C.A.L.; Hunter, P.D.; Tyler, A.N.; Vicente, V.M.; Horváth, H.; Kovács, A.W.; Vörös, L.; Preston, T.; Présing, M. 2015. Spatial Variability of absorption coefficient over a biogeochemical gradient in a large and optically complex shallow lake. **J. Geophys. Res.**, 120, 7040–7066.

Ritchie, J.C.; Schiebe, F.R.; Mchenry, J.R.1976. Remote sensing of suspended sediments in surface waters. **Photogramm. Eng. Remote Sens.** 42, 1539–1545. https://doi.org/10.1002/2015JC011202

Rodrigues, T.W.P.; Guimarães, U.S.; Rotta, L.H.; Watanabe, F.S.; Alcântara, E.; Imai, N.N. 2016. Sampling design in reservoirs based on Landsat-8/OLI images: A case study in

Nova Avanhandava reservoir (São Paulo State, Brazil). **Bol. Ciênc. Geod.** 22, 304–323. http://dx.doi.org/10.1590/S1982-21702016000200017

Rodrigues, T.; Alcântara, E.; Watanabe, F.; Bernardo, N.; Rotta, L.; Imai, N. 2016.Spatial and temporal variations of the inherent optical properties in a tropical cascading reservoir system. **Model. Earth Syst. Environ**. 2016, 2,86. https://doi.org/10.1007/s40808-016-0144-4

Rodrigues, T, Alcântara, E., Watanabe, F., Imai, N. 2017. Retrieval of Secchi disk depth from a reservoir using a semi-analytical scheme. **Remote Sens. Environ.** 198, p. 213-228, https://doi.org/10.1016/j.rse.2017.06.018

Rodrigues, T., Mishra, D. R., Alcântara, E., Watanabe, F., Rotta, L., Imai, N. 2017b. Retrieving Total Suspended Matter in Tropical Reservoirs Within a Cascade System With Widely Differing Optical Properties. IEEE Journal of Selected Topics in Applied Earth Observations and Remote Sensing, 10(12), 5495-5512. https://doi.org/10.1109/JSTARS.2017.2745700

Roesler, C. S.; Perry, M. J. 1995. In situ phytoplankton absorption, fluorescence emission, and particulate backscattering spectra determined from reflectance. **JGR:Oceans** 100, n. C7, p. 13279, 1995. https://doi.org/10.1029/95JC00455

Ruddick, K.G.; de Cauwer, V.; Park, Y.; Moore, G. 2006. Seaborne measurements of near infrared water-leaving reflectance: The similarity spectrum for turbid waters. **Limnol. Oceanogr.** 51, 1167–1179. https://doi.org/10.4319/lo.2006.51.2.1167

Sathyendranath, S.; Lazzara, L.; Prieur, L. 1987. Variations in the spectral values of specific absorption of phytoplankton. Limnol. Oceanogr. 32, 403–415. https://doi.org/10.4319/lo.1987.32.2.0403

Shaju, S.S.; Minu, P.; Srokanth, A.S.; Ashraf, P.M.; Vijayan, A.K.; Meenakumari, B. 2017. Decomposition study of in vivo phytoplankton absorption spectra to identify the pigments and phytoplankton group in complex case 2 waters of coastal Arabian Sea. **Oceanol. Hydrobiol. Stud.** 44(3), 282–293.

Shen, Q.; Li, J.; Zhang, F.; Li, J.; Li, W.; Zhang, B. 2015. Classification of several optically complex waters in China using in situ remote sensing reflectance. **Remote Sens.** 7, 429–440. https://doi.org/10.3390/rs71114731

Shi, L.; Mao, Z.; Wu, J.; Liu, M.; Zhang, Y.; Wang, Z. Variations in spectral absorption properties of phytoplankton, non-algae particles and Chromophoric Dissolved Organic Matter in Lake Qiandaohu.. **Water** 9(5), 352. https://doi.org/10.3390/w9050352

Shi, K., Zhang, Y., Liu, X., Wang, M., Qin, B., 2014. Remote sensing of diffuse attenuation coefficient of photosynthetically active radiation in Lake Taihu using MERIS data. **Remote Sens. Environ**. 140, 365–377. https://doi.org/10.1016/j.rse.2013.09.013

Smith, R.C.; Baker, K.S. 1981. Optical properties of the clearest natural waters (200–800 nm). **Appl. Opt.** 20(2), 177–184. https://doi.org/10.1364/AO.20.000177

Smith,W.S.; Espíndola, E.L.G.; Rocha, O. 2014. Environmental gradients in reservoirs of the medium and low Tietê River: Limnological differences trough the habitat sequence. **Acta Limnol. Bras.**, 16, 73–88. http://dx.doi.org/10.1590/S2179-975X2014000100009

Song, K.S., Li, L., Wang, Z.M., Liu, D.W., Zhang, B., Xu, J.P., Du, J., Li, L.H., and Li, S. 2012. Retrieval of total suspended matter and chlorophyll-a using remote sensing data for drinking water resources. **Environ. Monit. Assess.,** 184(3), 1449-1470. http://dx.doi.org/10.1007/s10661-011-2053-3

Song, K.S., Li, L., Tedesco, L., Duan, H.T., Li, L.H., Du, J. 2014. Remote quantification of total suspended matter trhough empirical approaches for inland waters. **Journal of Environemntal Informatics** 23(1), 23-36. https://doi.org/10.3808/jei.201400254

Souza, A.D.G.; Tundisi, J.G. 2000. Hidrogeochemical comparative study of the Jaú and Jacaré-Guaçu River watersheds, São Paulo, Brazil. (English). **Rev. Bras. Biol.** 60, 563–570. http://dx.doi.org/10.1590/S0034-71082000000400004

Spyrakos, E.; O'Donnell, R.; Hunter, P.D.; Miller, C.; Scott, M.; Simis, S.G.; Neil, C.; Barbosa, C.C.; Binding, C.E.; Bradt, S.; et al. 2018. Optical types of inland and coastal waters. **Limnol. Oceanogr.** 2018, 63, 846–870. https://doi.org/10.1002/lno.10674

Straškraba, M. Retention time as a key variable of reservoir limnology. In Theoretical Reservoir Ecology and Its Applications; Tundisi, J.G., Straškraba, M., Eds.; International Institute of Ecology, Brazilian Academy of Sciences and Backhuys Publishers: São Carlos, Brazil, 1999; pp. 385–410.

Tassan, S.; Ferrari, G. M. 1995. An alternative approach to absorption measurements of aquatic particles retained on filters. **Limnol. Oceanog**. 40(8), 1358-1368. https://doi.org/10.4319/lo.1995.40.8.1358

Tassan, S.; Ferrari, G. M. 1998. Measurement of light absorption by aquatic particles retained on filters: determination of the optical path length amplification by the 'transmittance-reflectance' method. J**. Plank. Res.**, 20(9), 1699-1709. https://doi.org/10.1093/plankt/20.9.1699

Tilstone, G.H.; Lotliker, A.A.; Miller, P.I.; Ashraf, P.M.; Kumar, T.S.; Suresh, T.; Ragavan, B.R.; Menon, H.B. 2013. Assessment of MODIS-Aqua chlorophyll-a algorithms in coastal and shelf waters of the eastern Arabian Sea. **Cont. Shelf Res**. 65, 14-26. https://doi.org/10.1016/j.csr.2013.06.003

Tilstone, G.; Moore, G.F.; Sørensen, K.; Doerffer, R.; Røttgers, R.; Ruddick, K.G.; Pasterkamp, R.; Jørgernsen, P.V. REVAMP, Regional Validation of MERIS Chlorophyll

Products in North Sea Coastal Waters, Protocols; European Union FPV: City of Brussels, Belgium, 2002; 68p.

Toole, D.A.; Siegel, D.A.; Menzies, D.W.; Neumann, M.J.; Smith, R.C. 2000. Remote sensing reflectance determinations in the coastal ocean environment: Impact of instrumental characteristics and environmental variability. **Appl. Opt.** 39, 456–469. https://doi.org/10.1364/AO.39.000456

Tonietto, A.E.; Lombardi, A.T.; Choueri, R.B.; Vieira, A.A. 2015. Chemical behavior of Cu, Zn, Cd, and Pb in a eutrophic reservoir: Speciation and complexation capacity. **Environ. Sci. Pollut. Res.** 22, 15920–15930. https://doi.org/10.1007/s11356-015-4773-3

Tundisi, J.G.; Matsumura-Tundisi, T. 1990. Limnology and eutrophication of Barra Bonita reservoir, S. Paulo State, Southern Brazil. **Arch. Hydrobiol. Beih.** 33, 661–676. https://doi.org/10.1007/s11356-015-4773-3. https://doi.org/10.1007/978-94-017-1096-1_2

Tundisi, J.D.; Matsumura-Tundisi, T.; Pareschi, D.C.; Luzia, A.P.; von Haeling, P.H.; Frollini, E. 2008. The Tietê/Jacaré watershed: A case study in research and management. **Estud. Av.**, 22, 159–172. http://dx.doi.org/10.1590/S0103-40142008000200010

Twardowski, M.S.; Boss, E.; Sullivan, J.M.; Donaghay, P.L. Modeling the spectral shape of absorption by chromophoric dissolved organic matter. Mar. Chem. 2004, 89, 69–88.

Tyler A.N., Hunter P.D., Spyrakos E., Groom S., Constantinescu A.M., Kitchen J. 2016. Developments in Earth observation for the assessment and monitoring of inland, transitional, coastal and shelf-sea waters**. Sci Total Environ** 572,1307–1321. https://doi.org/10.1016/j.scitotenv.2016.01.020

Vähätalo, A.V.; Wetzel, R.G. 2004. Photochemical and microbial decomposition of chromophoric dissolved organic matter during long (months–years) exposures. **Mar. Chem.** 89, 313–326. https://doi.org/10.1016/j.marchem.2004.03.010

Vanhellemont, Q.; Ruddick, K.G. 2015. Advantages of high quality SWIR bands for ocean colour processing: Examples from Landsat-8. **Remote Sens. Environ.** 161, 89–106. https://doi.org/10.1016/j.rse.2015.02.007

Vanhellemont, Q.; Ruddick, K.G. 2014. Turbid wakes associated with offshore wind turbines observed with Landsat 8. **Remote Sens. Environ**. 145, 105–115. https://doi.org/10.1016/j.rse.2014.01.009

Vanhellemont, R. 2019. Adaptation of the dark spectrum fitting atmospheric correction for aquatic applications of the Landsat and Sentinel-2 archives. **Remote Sens. Environ.** 225, 175-192. https://doi.org/10.1016/j.rse.2019.03.010.

Vishnu, P.S.; Shaju, S.S.; Tiwari, S.P.; Menon, N.; Nashad, M.; Joseph, C.A.; Raman, M.; Hatha, M.; Prabhakaran, M.P.; Mohandas, A. 2018. Seasonal variability in bio-optical properties along the coastal waters of Cochin. **Int. J. Appl. Earth Obs. Geoinf.** 66, 184–195. https://doi.org/10.1016/j.jag.2017.12.002

Watanabe, F., Mishra, D. R., Astuti, I., Rodrigues, T., Alcântara, E., Imai, N. and Barbosa, C. 2016. Parametrization and calibration of a quasi-analytical algorithm for tropical eutrophic waters. **ISPRS J Photogramm**, 12, 28–47, . https://doi.org/10.1016/j.isprsjprs.2016.08.009.

Xiao, Y.H.; Räike, A.; Hartikainen, H.; Vähätalo, A.V. 2015. Iron as a source of color in river waters. **Sci. Total Environ.** 536, 914–923. https://doi.org/10. 1016/j.scitotenv.2015.06.092.

Xu, J., Hood, R.R., Chao, S.Y., 2005. A simple empirical optical model for simulating light attenuation variability in a partially mixed estuary. **Estuaries** 28, 572–580. https://doi.org/10.1007/BF02696068

Xue, K., Ma, R., Duan, H., Boss, E., Cao, Z. 2019. Inversion of inherent optical properties in optically complex waters using sentinel 3A/OLCI images: A case study of China's three largest freshwater lakes. **Rem. Sen. Environ.** 225, 328-346. https://doi.org/10.1016/j.rse.2019.03.006

Wang, Y., Shen, F., Sokoletsky, L., Sun, X. 2017. Validation and calibration of QAA algorithm for CDOM absorption retrieval in the Changjiang (Yangtze) Estuarine and Coastal Waters. **Remote Sens.** 9, 1192. http://doi.org/10.3390/rs9111192

Watanabe, F.S.Y.; Alcântara, E.; Imai, N.; Rodrigues, T.; Bernardo, N. 2018. Estimation of Chlorophyll-a Concentration from Optimizing a Semi-Analytical Algorithm in Productive Inland Waters. **Remote Sens.** 10, 227. https://doi.org/10.3390/rs10020227

Watanabe, F.S.Y.; Alcântara, E.H.; Rodrigues, T.W.P.; Bernardo, N.M.R.; Rotta, L.H.S.; Imai, N.N. 2017. Phytoplankton community dynamic detection from the chlorophyll-specific absorption coefficient in productive inland waters**. Acta Limnol. Bras.**, 29, s2179–s2975. http://dx.doi.org/10.1590/s2179-975x0417

Wei, J.; Lee, Z.; Shang, S. 2016. A system to measure the data quality of spectral remote-sensing reflectance of aquatic environments**. JGR: Oceans** 121, 8189–8207. http://dx.doi.org/10.1002/2016JC012126

WET Labs, Inc. Spectral Absorption and Attenuation Sensor AC-S. User's Guide (Revision L). 33p. 2013. Available at: < http://www.wetlabs.com/sites /default /files /documents /acsl_0.pdf>. Access in: 05 March 2018.

WET Labs, Inc. Scattering Meter ECO BB-9. User's Guide (Revision L). 21p. 2013. Available at: < http://www.wetlabs.com/sites/default/files/documents/bb9l.pdf>. Access in: 09 March 2019.

Wòzniak, S.B.; Meler, J.; Lednicka, B.; Zdun, A.; Sto ´ n-Egiert, J. 2011. Inherent optical properties of suspended particulate matter in the southern Baltic Sea. **Oceanologia** 53, 691–729. https://doi.org/10.5697/oc.53-3.691

Wu, G., Cui, L., Duan, H., Fei, T., Liu, Y. 2011. Absorption and backscattering coefficients and their relations to water constituents of Poyang Lake, China. **Appl. Opt.** 50(34), 6358-6369. https://doi.org/10.1364/AO.50.006358.

Yang, W., Matsushita, B., Chen, J., Yoshimura, K., Fukushima, T. 2013. Retrieval of inherent optical properties for turbid inland waters from remote-sensing reflectance. **IEEE Trans. Geosc. Remote Sens**. 51(6), 3761 – 3773. https://doi.org/10.1109/TGRS.2012.2220147.

Yang, W.; Matsushita, B., Chen, J.; Yoshimura, K., Fukushima, T. 2014. Application of a Semianalytical Algorithm to remotely estimate diffuse attenuation coefficient in turbid waters. **IEEE Geos. and Remote Sens. Letters** 11, 1046-1050. https://doi.org/10.1109/LGRS.2013.2284343.

Zanter, K. 2018. Landsat 8 Surface Reflectance Code – Product Guide v.1.0. Available at: https://prd-wret.s3-us-west-2.amazonaws.com/assets/palladium/production/atoms/files/LSDS-1368_L8_Surface_Reflectance_Code_LASRC_Product_Guide-v2.0.pdf. Access: 25 April 2019.

Zhang, Y. L., Liu, M.L., Wang, X., Zhu, G.W., Chen, W.M. 2009. Bio-optical properties and estimation of the optically active substances in Lake Tianmuhu in summer. **Int. J. Remote Sens.** 30(11), 2837-2857. https://doi.org/10.1080/01431160802558592

Zhang, Y.; Zhang, B.; Wang, X.; Li, J.; Feng, S.; Zhao, Q.; Liu, M.; Qin, B. 2007. A study of absorption characteristics of chromophoric dissolved organic matter and particles in Lake Taihu, China. **Hydrobiologia** 2007, 592, 105–120. https://doi.org/10.1007/s10750-007-0724-4

Zhang, M.; Tang, J.; Dong, Q.; Song, Q.; Ding, J. 2010. Retrieval of total suspended matter concentration in the Yellow and East China Seas from MODIS imagery. **Remote Sens. Envron.**, 114, 392–403. https://doi.org/10.1016/j.rse.2009.09.016

Zhang, X.; He, S.; Shabani, A.; Zhai, P.; Du, K. 2017. Spectral sea surface reflectances of skylight**. Opt. Exp.** 25,1–13. https://doi.org/10.1364/OE.25.0000A1

Zhu, W.; Yu, Q.; Tian, Y.Q.; Becker, B.L.; Zheng, T.; Carrick, H.J. 2014. An assessment of remote sensing algorithms for colored dissolved organic matter in complex freshwater environments. **Remote Sens. Environ**. 140,776–778. https://doi.org/10.1016/j.rse.2013.10.015.

Zibordi, G.; Ruddick, K.; Ansko, I.; Moore, G.; Kratzer, S.; Icely, J.; Reinart, A. 2012. In situ determination of the remote sensing reflectances: An inter-comparison. **Ocean Sci.** 567–586. https://doi.org/10.5194/os-8-567-2012